ANUL L 2005

STUDIA
UNIVERSITATIS BABEŞ–BOLYAI
PHYSICA

2

Editorial Office: 400015 – Cluj–Napoca Republicii no. 24, Phone: 0264-405352

SUMAR - SOMMAIRE - CONTENTS - INHALT

STUDIA UNIVERSITATIS BABEŞ-BOLYAI, PHYSICA, L, 2, 2005

MICROWAVE ABSORPTION IN PLASMIDIC PBR322 DNA MOLECULES

CRISTINA M. MUNTEAN[1], ANDREI IOACHIM[2], CĂLINA CORNEA[3]

ABSTRACT. In this work, scalar microwave measurements of insertion loss and return loss have been caried out between 7.3-12.4 GHz, at room temperature, for aqueous solutions of plasmidic pBR322 DNA and for the corresponding buffer. A low intensity microwave driving field was considered. Samples were placed in a particular configuration of weak electric field. The relative electric-field attenuation constants and the percentage of the microwave power attributed to 4362 bp circular DNA-hydration layer, were calculated on the basis of insertion loss and return loss. A broadband influence of low-intensity microwaves, have been found for plasmidic DNA-hydration layer systems. No sharp feature, which might prove the participation of acoustic mode excitation to DNA dynamics, at GHz-frequencies has been observed. Debye type relaxation processes can explain the experimental results.

Keywords: 4362 bp circular DNA; DNA-hydration layer system; microwave absorption

1. Introduction

The polyanionic nature of DNA molecules in neutral aqueous solution is responsible for the strong coupling of dissolved DNA to the microwave field [1]. The molecular mechanisms characterizing this interaction are of utmost importance.

Particularly, the possibility of resonant microwave absorption at room temperature, by uniform DNA molecules in buffer solution, was a subject of controversy in the scientific literature [2-9]. However, several independent works have reported no resonant absorption by plasmidic DNA in aqueous solution [6-10].

In order to establish the direct absorption in the biopolymer and in the hydration layer system, it is important to determine the microwave absorption in dissolved DNA [8]. This phenomenon might be usefull with regard to the identification of the cellular targets, during the interactions of complex systems with a microwave field [10-13]. Biological effects observed during such interactions, may result from many processes, occuring at levels from the membrane down to DNA [1,13]. The relationship between energy deposition, molecular damage and also cellular components and biological 'end-point' is in radiobiology an obscure matter [1,14].

---

[1] National Institute of Research and Development for Isotopic and Molecular Technologies, R-400293 Cluj-Napoca, P. O. 5, Box 700, Romania .To whom correspondence should be addressed. Telephone: +40-264-584037; Telefax: +40-264-420042; e-mail: cmuntean@s3.itim-cj.ro

[2] National Institute of Research and Development for Materials Physics, P. O. Box MG-7, R-76900 Bucharest-Magurele, Romania

[3] Institute of Biology, Bucharest 77748, Splaiul Independentei 296, Romania

In this work, the relative electric-field attenuation constants and the percentage of the microwave power attributed to pBR322 DNA-hydration layer systems, were calculated on the basis of the scalar microwave characteristics. Method used is applicable to microwave absorption in substances that form hydration layers with water [8,10]. A paper reflecting the behaviour of chromosomal DNA molecules, in the same type of microwave experiment, has already been submitted to publication [10].

The aim of this paper is to study the attenuation and absorption properties of dissolved plamidic pBR322 DNA molecules, in a microwave field, at low-gigahertz frequencies. The molecular interaction mechanisms of dissolved circular 4362 bp DNA with the microwave field are of interest.

2. Materials and methods

Methods refering to in the following were previously used by us [10, 15-17]. Scalar microwave measurements of insertion loss and return loss were carried out, simultaneously, at room temperature, with a Hewlett Packard 8757C Network Analyzer. Low-intensity microwaves (TE10 mode) were used. A teflon sample holder was placed in the X-band waveguide, in a configuration of weak electric field. The power reflected from the sample was monitored by an impedance bridge [10, 16]. The combined mismatches of the sample holder with and without test samples were considered small, with less than 1% of the incident power being reflected in almost all the experimental frequency range (7.3-12.4 GHz). A signal mediated over 16 scans was considered. The schematic diagram of the experimental microwave set-up, used in these type of experiments, was previously presented [10, 16].

Several plasmidic pBR322 DNA samples (4362 base pairs circular DNA), extracted by standard techniques from E. coli have been investigated. Samples, isolated and purified in our laboratories, were prepared independently by separate extractions. After each extraction, DNA molecules were dissolved in a storage buffer (10 mM Tris-HCl, 1 mM EDTA, pH = 8 or 1 mM Tris-HCl, 0.1 mM EDTA, pH = 8). The sample quality was checked by UV spectrophotometric method, using a specord UV-VIS with a pair of tandem cells. In some cases agarose gel electrophoresis with standard markers has been used.

For the same volume of sample and reference, microwave response of a given aqueous solution of DNA was compared with the corresponding microwave response of the standard storage buffer. On the basis of the physics analysis of the measured quantities of insertion loss and return loss [10, 15-17], were calculated for each DNA sample, the relative electric-field attenuation constants and the ratio $\Delta P_{abs}/P_i$ (%)., between the difference in the absorption of DNA solution . $P_{DNA\ solution}$ and that in free buffer P_{buffer}, and the incident power which was the same for the compared samples [10, 15-16].

Here, $P_{DNA\ solution}$ includes the microwave power absorbed in each of the three component volumes - solute volume, hydration layer volume, and free solvent volume [8,10, 15]. The microwave power absorbed in DNA-hydration layer system is calculated by ΔP_{abs}= .$P_{\text{DNA solution}}$ - P_{buffer}.

A computing algorithm was developed by us for calculating the relative electric-field attenuation constants and the percentage of the microwave absorption attributed from this data analysis to dissolved DNA [10, 15-17]. The relative attenuation constants were estimated for each sample in three distinct ways, with minor differences in the values of the attenuation parameters.

3. Results and Discussion

In this work the relative electric field attenuation constants and the percentage of the incident microwave power absorbed in 4362 bp circular DNA-hydration layer system, have been calculated between 7.3-12.4 GHz, for several plasmidic DNA samples extracted in our laboratories. The interaction mechanisms of uniform DNA molecules with the low-intensity microwave field, are of interest.

Examples of data obtained by us on dissolved plasmidic pBR322 DNA samples, are presented in Figures 1-4. The frequency- dependence of the relative electric field attenuation constant and of the percentage of the incident microwave power, attributed to dissolved 4362 bp circular DNA are shown in Figures 1 and 2. DNA was dissolved in a standard storage buffer (10 mM Tris-HCl, 1 mM EDTA, pH=8) at a concentration of 3.94 mg/ml.

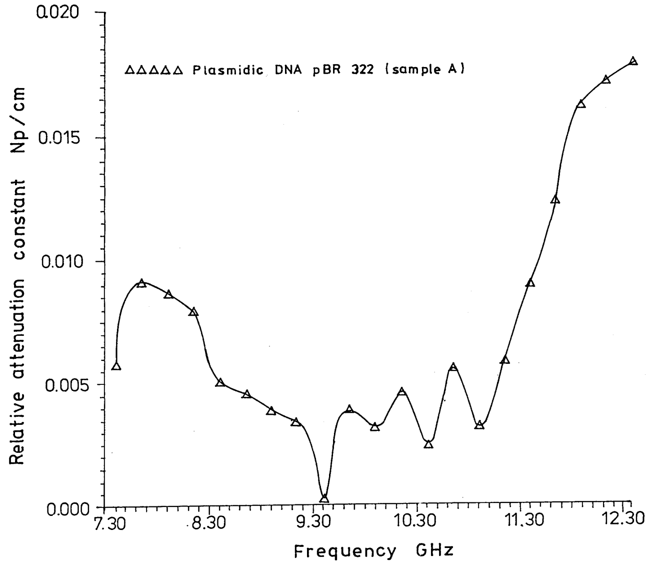

Fig. 1. The frequency-dependence of the relative electric field attenuation constant for 4362 bp circular DNA, dissolved in a standard storage buffer (10 mM Tris-HCl, 1 mM EDTA, pH=8), at a concentration of 3.94 mg/ml.

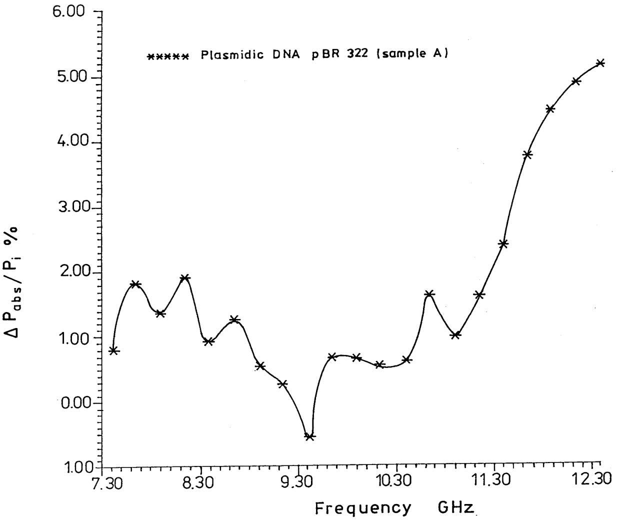

Fig. 2. The frequency-dependence of the percentage of the incident microwave power absorbed in 4362 bp circular DNA-hydration layer system. DNA was dissolved in a standard storage buffer (10 mM Tris-HCl, 1 mM EDTA, pH = 8) at a concentration of 3.94 mg/ml. Relative measurements have background absorption substracted.

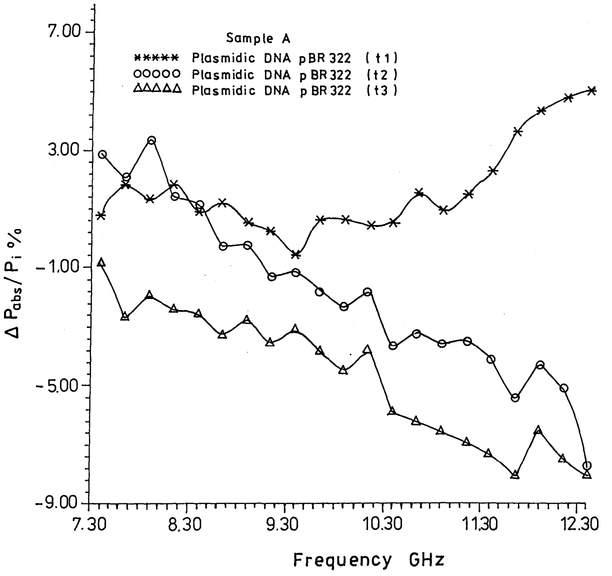

Fig. 3. The frequency-dependence of the percentage of the incident microwave power absorbed in plasmidic pBR322 DNA-hydration layer system, at three distinct times from isolation and purification from E. coli. DNA was dissolved in a standard storage buffer (10 mM Tris-HCl, 1 mM EDTA, pH = 8) at a concentration of 3.94 mg/ml. Relative measurements have background absorption substracted.

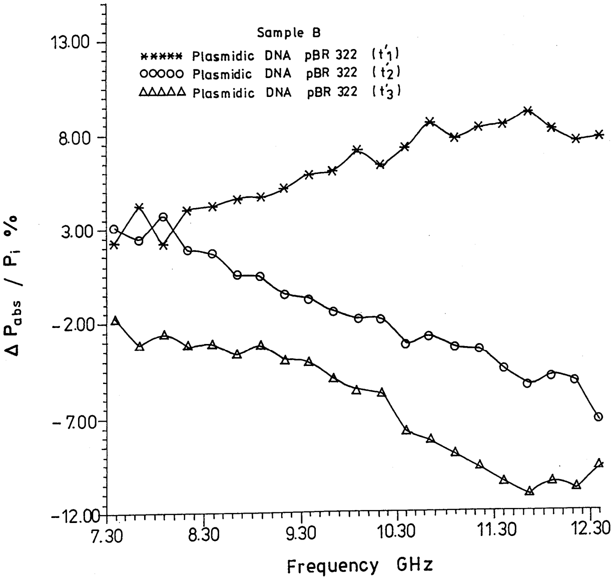

Fig. 4. The frequency-dependence of the percentage of the incident microwave power absorbed in 4362 bp circular DNA and in its hydration layer, at three distinct times from isolation and purification from E. coli. DNA was dissolved in a storage buffer (10 mM Tris-HCl, 1 mM EDTA, pH=8), at a concentration of 2.05 mg/ml. Relative measurements have background absorption substracted.

Besides, the frequency-dependence of the percentage of the incident microwave power absorbed in two plasmidic DNA-hydration layer systems, are presented in Figures 3-4, at three distinct times from isolation and purification from E. coli. The dependence of the microwave absorption in dissolved DNA on the in vitro aging of the biopolymer is of interest. Here, time parameter t_2 refers to one day more than time parameter t_1 and t_3 refers to one day more than t_2. The same time relation is between t'_1, t'_2 and t'_3. The spectrum presented in Fig. 3 (t_1) is the same with the spectrum presented in Fig. 2. The two samples belong to different extractions from bacterial cultures. DNA was dissolved in a standard storage buffer (10 mM Tris-HCl, 1 mM EDTA, pH = 8) at concentrations of 3.94 mg/ml and 2.05 mg/ml.

Data analysis show a broadband influence of low intensity microwaves for dissolved pBR322 plasmids investigated here. In the experimental frequency range, we didn't observe for these samples any resonant spectral feature which might prove the participation of acoustic modes to DNA dynamics. A time dependent microwave absorption signature is to be observed. This is probably due to the in vitro aging of the biopolymer.

Debye type relaxation processes of circular DNA-hydration layer systems can explain the experimental results.

When registering a mediated microwave signal, immediately after a first similar one, no modification of the microwave characteristics has been found. This means, that in these conditions, method used is not sensitive to possible DNA structural changes caused by microwave irradiation.

Attempts to identify the direct microwave absorption in DNA and in the hydration layer surrounding this biopolymer have been made, on the basis of the Debye model of dielectric constants [8]. The microwave absorption of DNA in solution is composed of three parts: absorption in the free water, absorption in the substance and absorption in the hydration layer [8, 10, 15]. Particularly, dielectric characteristics of different regions inside the DNA-hydration layer system are due to the dipole moments of modestly polar bases, less polar sugars, negatively charged phosphates and water molecules [10, 16-18].

In conclusion, in this work the relative electric-field attenuation constants and the percentage of the microwave power attributed to 4362 bp circular DNA-hydration layer, were calculated on the basis of insertion loss and return loss. A broadband influence of the low-intensity microwaves have been found for plasmidic DNA-hydration layer systems. No sharp feature, which might prove the participation of acoustic mode excitation to DNA dynamics, at GHz-frequencies has been observed. A time dependent microwave absorption signature due to the in vitro aging of the biopolymer is to be found. Debye type relaxation processes can explain the experimental results.

Acknowledgements

The authors wish to thank to Mr. O. Petrean for writing the computing algorithm of the attenuation and absorption parameters. We acknowledge fruitful discussions on sample preparation with Dr. I. Vatafu from the Institute of Biology, Bucharest, Romania.

REFERENCES

1. Muntean, C., Aldea, N., Purcaru, M., Dynamical properties of DNA in a microwave field, in T. Theophanides, J. Anastassopoulou and N. Fotopoulos (eds.), Proceedings of the Fifth International Conference on the Spectroscopy of Biological Molecules Proc., Kluwer Academic Publishers, Dordrecht Boston London (1993) 73-74.
2. Edwards, G.S., Davis, C.C., Saffer, J.D., Swicord, M.L., Resonant microwave absorption of selected DNA molecules, Phys. Rev. Lett. 53 (1984), 1284-1287.
3. Edwards, G.S., Lindsay, M., Prohofsky, E.W., Comment on Resonant microwave absorption of selected DNA molecules and Observation of low-lying Raman bands in DNA by tandem interferometry, Phys. Rev. Lett. 54 (1985) 607.

4. Edwards, G.S., Davis, C.C., Saffer, J.D., Swicord, M.L., Microwave-field-driven acoustic modes in DNA, Biophys. J. 47 (1985) 799-807.
5. Davis, C.C., Edwards, G.S., Swicord, M.L., Sagripanti, J., Saffer, J., Direct excitation of internal modes of DNA by microwaves, Bioelectrochem. Bioenergetics, 16 (1986) 63-76.
6. Gabriel, C., Grant, E.H., Tata, R., Brown, P.R., Gestblom, B., Noreland, E., Microwave absorption in aqueous solutions of DNA, Nature 328 (1987) 145-146.
7. Foster, K.R., Epstein, B.R., Gealt, M.A., 'Resonances' in the dielectric absorption of DNA, Biophys. J. 52 (1987) 421-425.
8. Garner, H.R., Ohkawa, T., Tuason, O., Lee, R.L., Microwave absorption in substances that form hydration layers with water, Phys. Rev. A 42 (1990) 7264-7270.
9. Bigio, I.J., Gosnell, T.R., Mukherjee, P., Saffer, J.D., Microwave absorption spectroscopy of DNA, Biopolymers 33 (1993) 147-150.
10. Muntean, C., Ioachim, A., Moldoveanu, D., Microwave absorption in chromosomal DNA molecules, Romanian Reports in Physics, submitted to publication.
11. Koschnitzke, C., Kremer, F., Santo, L., Quick, P., Poglitsch, A., A non-thermal effect of millimeter wave radiation on the puffing of giant chromosomes, Z. Natur forsch. 38 c (1983) 883-886.
12. Belyaev, I.Ya., Alipov, D., Shcheglov, V.S., Chromosome DNA as a target of resonant interaction between Escherichia Coli cells and low-intensity millimeter waves, Electro- and Magnetobiology 11 (1992) 97-108.
13. Saffer, J.D., Profenno, L.A., Sensitive model with which to detect athermal effects of non-ionizing electromagnetic radiation, Bioelectromagnetics 10 (1989) 347-354.
14. Baverstock, K.F., Cundall, R.B., Solitons and energy transfer in DNA, Nature 332 (1988), 312-313.
15. Muntean, C., Ioachim, A., Petrean, O., Evaluation of microwave absorption in DNA - hydration layer systems, în J. C. Merlin, S. Turrell and J. P. Huvenne (eds.), *Proceedings of the 6th European Conference on the Spectroscopy of Biological Molecules,* Kluwer Academic Publishers Dordrecht Boston London (1995) 333-334.
16. Muntean, C.M., Cozar, O., Banciu, G., Pop, S., Microwave absorption spectroscopy of DNA polymers in the presence of Cu(II) ions, Proc. Suppl. Balkan Phys. Lett. 5 (1997) 211-214.
17. Muntean, C.M., Banciu, G., Cozar, O., Ioachim, A., Microwave response of DNA polymers with counterion distribution, in Spectroscopy of Biological Molecules: New Directions, J. Greve, G.J. Puppels and C. Otto (Eds.), Kluwer Academic Publishers, Dordrecht, Olanda (1999) p. 223-224.
18. Yang, L., Weerasinghe, S., Smith, P.E., Pettitt, B.M., Dielectric response of triplex DNA in ionic solution from simulations, Biophys. J. 69 (1995) 1519-1527.
19. Sagripanti, J.L., Swicord, M.L., DNA structural changes caused by microwave radiation, Int. Radiat. Biol. 50 (1986) 47-50.
20. Davis, M.E., VanZandt, L.L., Microwave response of DNA in solution: theory, Phys. Rev. A 37 (1988) 888-901.

21. Fisun, O.I., Katanaev, M.O., Theoretical study of resonant microwave absorption by DNA in aqueous solution, Makromol. Chem. 192 (1991) 2191-2202.
22. Edwards, G., Ying, G., Tribble, J., Role of counterions in the gigahertz relaxation of wet DNA, Phys. Rev. A 45 (1992) R8344-R8347.

STUDIA UNIVERSITATIS BABEŞ-BOLYAI, PHYSICA, L, 2, 2005

STRUCTURAL INVESTIGATION OF Fe_2O_3 - P_2O_5-MO ($MO \Rightarrow CaO$ or Li_2O) GLASS SYSTEMS BY FTIR SPECTROSCOPY

C. ANDRONACHE[1], P. PĂŞCUȚĂ [2] AND I. ARDELEAN [3]

ABSTRACT. Glasses from the systems, $xFe_2O_3\cdot(100-x)[P_2O_5\cdot MO]$ ($MO \Rightarrow CaO$ or Li_2O) with $0 \leq x \leq 50$ mol% were prepared in the same conditions and characterized by IR spectroscopy. It was established the mode in which both Fe_2O_3 and the replacing of the CaO by the Li_2O in these systems influences the local structure of these glasses. The iron ions generally modify in a different way the local structure of these glasses, depending on the presence of the CaO or the Li_2O in the glass matrix. The results shown that phosphate units are the main structural units of the glass system and the iron ions are located in the network.

1. Introduction

In general, the properties of a glass depend on its composition and to a considerable extent upon its structure [1]. The structure of binary and ternary phosphate glasses has been studied by neutron and X-ray diffraction [2, 3], Raman scattering [4 - 8], infrared absorption [8 - 10] and nuclear magnetic resonance [4, 11 - 14]. P_2O_5 is a well-known network former with PO_4 structural units with one of the four oxygen atoms in PO_4 tetrahedron is doubly bonded to the phosphorous with a substantial π - bond character to account for the pentavalency of phosphorous [1, 15]. The PO_4 tetrahedrons are linked together with covalent bridging oxygens [1]. The addition of alkali or alkaline earth oxides such as Li_2O or CaO to P_2O_5 glasses results in conversion of the three-dimensional network, to linear phosphate chains [8, 16, 17]. This linear chain structure results in cleavage of P-O-P linkages and the creation of non-bridging oxygen in the glass. Neighboring phosphate chains are linked together by cross – bonding between the metal cations and two non – bridging oxygen atoms of each PO_4 tetrahedron. In general P – O – P bond between PO_4 tetrahedron is much stronger than the cross – bond between chains via the metal cations [18].

The structure and properties of phosphate glasses containing transition metal oxide such as Fe_2O_3 have attracted considerable interest in recent years because of their structural, optical, electrical and magnetic properties [19 - 21]. The addition of iron ion to phosphate glasses has a significant effect on the glass transition temperature, thermal expansion coefficient and improves the chemical durability [19, 22]. It has been suggested that the excellent chemical

---

[1] Faculty of Physics, Babes-Bolyai University, 400084 Cluj-Napoca, Romania
[2] Department of Physics, North University, 430083 Baia Mare, Romania
[3] Department of Thermothecnics, Technical University, 400641 Cluj-Napoca, Romania

durability of iron phosphate glasses is attributed to the replacement of P – O - P bond by more moisture resistant P – O – Fe bond [19, 23]. The variation in the properties of iron phosphate glasses is consistent with a shortening of the length of the phosphate chains, which leads to a strengthening of the glass network through the formation of P – O – Fe bonds [19, 24].

In the present work two systems, $xFe_2O_3·(100-x)[P_2O_5·MO]$ ($MO \Rightarrow CaO$ or Li_2O) with $0 \leq x \leq 50$ mol% were prepared in the same conditions and characterized by IR spectroscopy in order to understand the role of the Fe_2O_3 and the replacing of CaO by Li_2O on the structure of these glass systems.

2. Experimental

The starting materials used in the present investigation were $(NH_4)_2HPO_4$, $CaCO_3$, Li_2CO_3 and Fe_2O_3 of reagent grade purity. The samples were prepared by weighing suitable proportions of components, powder mixing and mixture melting in sintered corundum crucibles at 1250^oC for 5 minutes. The mixtures were put into the furnace direct at this temperature. The melts were poured onto stainless steel plates. The X-ray patterns of the investigated samples are characteristic for vitreous systems. No crystalline phase was observed up to 50 mol % Fe_2O_3 for both glass systems.

The FT-IR absorption spectra of the glasses in the 400 - 2500 cm^{-1} spectral range were obtained with an Equinox 55 Bruker spectrometer. The IR absorption measurements were done using the KBr pellet technique. In order to obtain good quality spectra the samples were crushed in an agate mortar to obtain particles of micrometer size. This procedure was applied every time to fragments of bulk glass to avoid structural modifications due to ambient moisture.

3. Results and discussion

The experimental IR spectrum for the $xFe_2O_3·(100-x)[P_2O_5·CaO]$ (S1) and $xFe_2O_3·(100-x)[P_2O_5·Li_2O]$ (S2) glass systems were presented in Figures 1 and 2. The absorption bands obtained and their assignments for each those two systems are summarized in Table 1. In the glass matrix spectrum of S1 glasses the following bands are present: ~ 490 cm^{-1}, ~ 530 cm^{-1}, ~ 770 cm^{-1}, ~910 cm^{-1}, ~ 1100 cm^{-1}, ~ 1290 cm^{-1} and ~ 1640 cm^{-1}. The weak band from at ~ 1640 cm^{-1} is ascribed to bending vibration of H – O – H [25]. The band at ~ 1290 cm^{-1} was assigned to asymmetric stretching vibration of P = O [26] and the band ~ 1100 cm^{-1} was ascribed to stretching vibration of $P – O^-$ [10]. A band centered at ~ 910 cm^{-1} is due to the P – O – P bending vibration [10] while the band centered at ~ 770 cm^{-1} corresponds to the stretching vibration of P – O – P [10]. The broad band at ~ 530 cm^{-1} was ascribed to bending harmonics of O = P – O [1] and the band at ~ 490 cm^{-1} was ascribed to the bending harmonics of O – P – O [1].

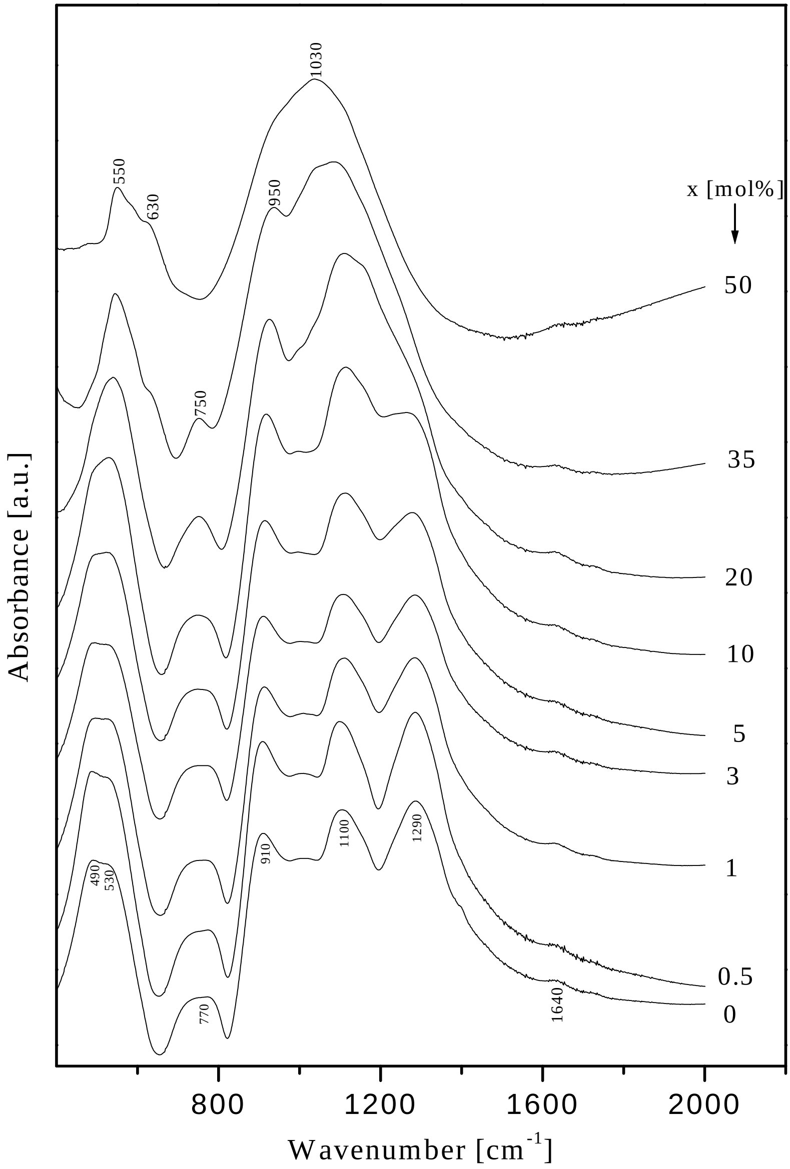

Fig. 1. Infrared absorption spectra of $xFe_2O_3{\cdot}(100\text{-}x)[P_2O_5{\cdot}CaO]$ glasses.

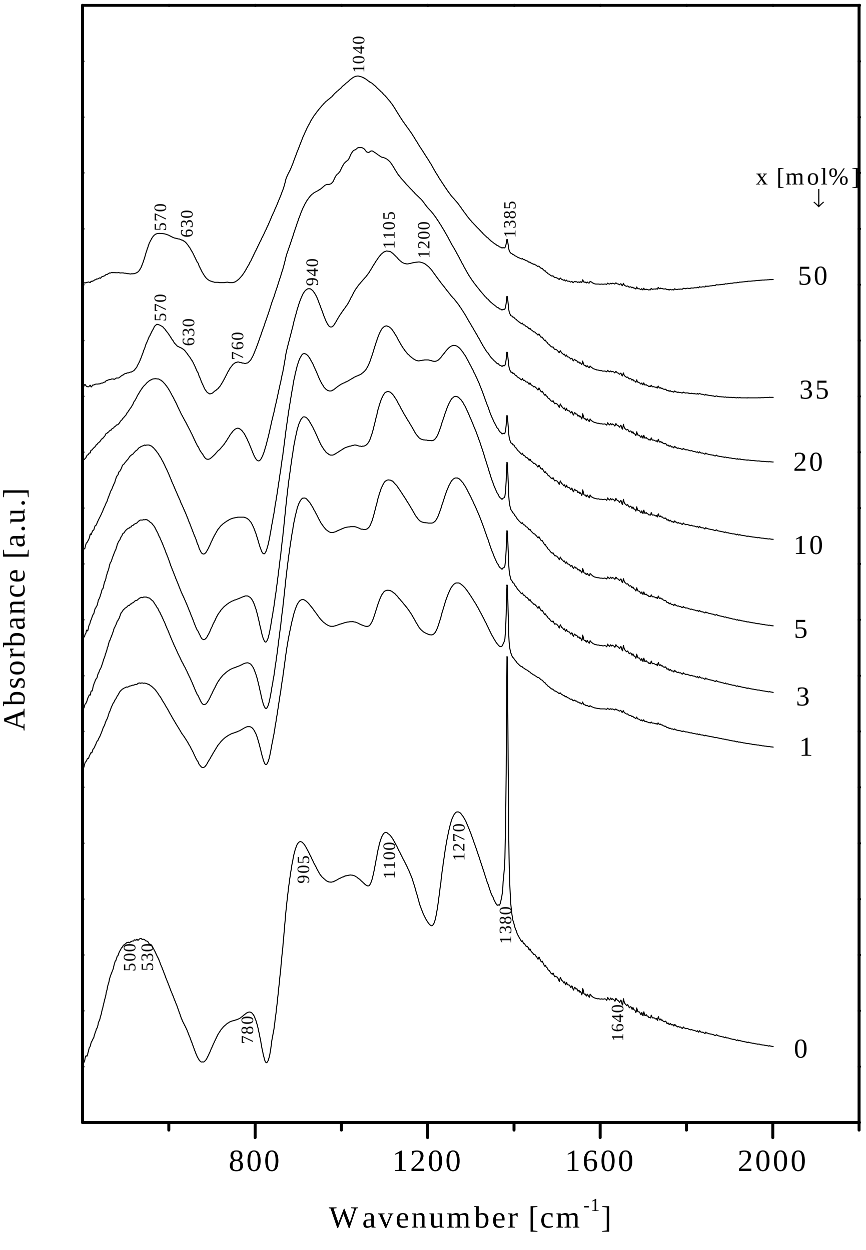

Fig. 2. Infrared absorption spectra of $xFe_2O_3·(100-x)[P_2O_5·Li_2O]$ glasses.

Table 1.
Frequencies and their assignments for IR spectra of $xFe_2O_3 \cdot (100-x)[P_2O_5 \cdot CaO]$ (S1) and of $xFe_2O_3 \cdot (100-x)[P_2O_5 \cdot Li_2O]$ (S2) glasses.

Wavenumber [cm^{-1}]		Assignments
S1 glasses	**S2 glasses**	
~490	~500	Bending harmonics of O – P – O
~530	~530	Bending harmonics of O = P – O
~550	~570	Vibrations of Fe-O bonds in FeO_4 units
~630	~630	Vibrations of Fe-O bonds in FeO_6 units
~770	~780	Stretching vibration of P – O – P
~750	~760	Stretching vibration of P – O – P
~910	~905	Bending vibration of P – O – P
~950	~940	Bending vibration of P – O – P
~1030	~1040	Stretching vibration of P – O^-
~1100	~1100	Stretching vibration of P – O^-
~1290	~1270	Symmetric stretching vibration of P = O
	~1380	Asymmetric stretching vibration of P = O
~1640	~1640	Bending vibration of H – O – H

The replacing of the CaO by the Li_2O in glass matrix leads to the apparition of the band centered at ~ 1380 cm^{-1}, which were assigned to symmetric stretching vibration of P = O [10]. The bands at ~ 490 cm^{-1}, ~770 cm^{-1}, ~910 cm^{-1} and ~ 1290 cm^{-1} shift to ~ 500 cm^{-1}, ~780 cm^{-1}, ~905 cm^{-1} and ~ 1270 cm^{-1}, respectively. How it was being expected, in this wevenumber range the CaO and Li_2O doesn't present the absorption bands.

The addition of iron ions to calcium- and lithium-phosphate glasses produces some changes in the IR spectrum. The intensity of the band at ~ 1380 cm^{-1} decreases with the increasing of Fe_2O_3 content. The band in the high frequency region, 1270-1290 cm^{-1}, gradually disappears by integration into the ~ 1100 cm^{-1} band in the glasses with x = 20 mol% for S1 glasses and x = 35 mol% for S2 glasses. The band from ~ 1100 cm^{-1} gradually shift to lower wavenumber at ~ 1030 cm^{-1} for x = 50 mol% in S1 glasses and ~ 1040 cm^{-1} for x = 50 mol% in the S2 glasses and broadens with increasing of x. The shift in the position of the band of the ionic groups PO_4^{3-} (1010 – 1090 cm^{-1}) may be considered as an indication for the formation of more non-bridging oxygen ions [27]. Moreover, these facts are due to the breaking of the P = O bonds and the reduced force constant between P and O [28]. This may be due to an increase in the charge density on the PO_4 tetrahedral group, which leads to more ionic and hence less covalent bonding. The band in the 905-910 cm^{-1} region, shifts to higher wavenumber at ~ 940 cm^{-1} for x = 35 mol% in S1 glasses and at ~ 950 cm^{-1} for x = 20 mol% in S2 glasses and disappears by merging into ~ 1100 cm^{-1} band for higher x. The intensity of the band, 740-750 cm^{-1}, decreases with the increasing of the Fe_2O_3 content and disappears for x > 35 mol% for both systems. So, we can say that at higher content of iron ions the P – O – P bonds are probably replaced by more chemically resistant P – O – Fe bonds [19, 22, 23]. The band from ~ 530 cm^{-1} gradually shifts to higher wavenumber and finally transforms into a band centered at ~ 550 cm^{-1} with a shoulder at ~ 630 cm^{-1} in S1 glasses and at ~ 570 cm^{-1} with a shoulder at ~ 630 cm^{-1} in S2 glasses. The band in the 550-570 cm^{-1} regions is ascribed to vibrations of Fe-O bonds in FeO_6 units [29] and the band at ~ 630 cm^{-1} is assigned to vibrations of Fe-O bonds in FeO_4 units [29].

4. Conclusions

It can be remake that in the same preparation conditions, in the studied glass systems were formed homogeneous glasses up to x = 50 mol% for both glass systems.

The replacing of the CaO by the Li_2O in glass matrix leads to the apparition of the band centered at ~ 1380 cm^{-1}. At higher content of iron ions the P =O bonds are breaking, the P – O – P bonds are replaced by P – O – Fe bonds and appears the FeO_4 units together with the FeO_6 units for both systems. The bands corresponding to the IR absorption of CaO and Li_2O are not directly evident.

REFERENCE

1. P. Subbala Kshmi and N. Veeraiah, *J. Non-Crst. Solids* **298**, 89 (2002). U. Hope, G. Walter, R. Kronold and D. Stachel, *J. Non-Cryst. Solids* **263&264**, 29 (2000).
2. K. Suzuya, D.L. Price, C.K. Loong and S.W. Martin, *J. Non-Cryst. Solids* **234&234**, 650 (1998).
3. R. K. Brow, D.R. Tallant, S.T. Myers and C.C. Phifer, *J. Non-Cryst. Solids* **191**, 45 (1995).
4. Y.S. Babovich, *Opt. Spectrosc.* **13**, 274 (1962).
5. B.C. Sales, R.S. Ramsey, B. Bates and L.A. Boatner, *J. Non-Cryst. Solids* **87**, 137 (1986).
6. P.P. Proulx, G. Cormier, J.A. Copobianco, B. Champagnon and M. Bettinelli, *J. Phys: Condens. Matter* **6**, 275 (1994).
7. G. Le Saout, F. Fayon, C. Bessada, P. Simon, A. Blin and Y. Vaills, *J. Non-Cryst. Solids* **293&295**, 657 (2001).

8. E. Efimov, *J. Non-Cryst. Solids* **209**, 209 (1997).
9. C. Dayanand, G. Bhikshamaiam, V.J. Tyagaraju, M. Salegram and A.S.R. Krishna Murthy, *J. Mater. Sci.* **31**, 1945 (1996).
10. F. Fayon, C. Bessada, A. Douy and D. Massiot, *J. Magn. Reson.* **137**, 116 (1999).
11. F. Fayon, C. Bessada, J.P. Coutures and D. Massiot, *Inorg. Chem.* **38**, 5212 (1999).
12. Lai, A. Musinu, G. Piccaluga and S. Puligheddu, *Phys. Chem. Gla*sses **38**, 173 (997).
13. G.N. Greaves, S.J. Gurman, L.F. Gladden, C.A. Spence, P.Cocs, B.C. Sales, L.A. Boatner and R.N. Jenkins, *Philos. Mag.* **B58**, 271 (1988).
14. A.A. Bahgat, M.M. El-Samanoundy and A.I. Sabry, *Phys. Chem. Solids* **60**, 1921 (1999).
15. B.C. Bunker, G.W. Arnold and J.A. Wilder, *J. Non-Cryst. Solids* **64**, 291 (1984).
16. Y.B. Peng and D.E. Day, *Glass Technol.* **5**, 166 (1991).
17. N.H. Ray, *Brit. Polym. J.* **11**, 163 (1979).
18. A.M. Milankovic, A. Santic, A. Gajovic and D.E. Day, *J. Non-Crst. Solids* **325**, 76 (2003).
19. A.M. Milankovic and D.E. Day, *J. Non-Crst. Solids* **162**, 275 (1993).
20. S. Muthupari and K.J. Rao, *J. Phys. Chem. Solids* **57**, 553 (1996).
21. X.J. Xu, D.E. Day, G.J. Long and R. K. Brow, *J. Non-Cryst. Solids* **215**, 21 (1997).
22. R.K.Brow, C.M. Arens, X. Yuand, D.E. Day, *Phys. Chem Glasses* **35**, 132 (1994).
23. A.M. Milankovic, B. Pivac, K. Furic and D.E. Day, *Phys. Chem. Glasses* **38**, 74 (1997).
24. L. Jun, X. Shyping and G. Shiyang, *Spectrochim. Acta* **51A(4)**, 519 (1995).
25. B.V.R. Chowdari, K.I. Tan, W.T. Chia and R. Gopalakrishnam, *J. Non-Cryst. Solids* **119**, 95 (1990).
26. Y. M. Moustafa and K. El-Egili, *J. Non-Cryst. Solids* **240**, 144 (1998).
27. J.J. Hudgens and S.W. Martin, *J. Am. Ceramic. Soc*. **76**, 1691 (1994).
28. R. Iordanova, Y. Dimitriev, V. Dimitrov, S. Kassabov and D. Klissurski, *J. Non-Cryst. Solids* **204**,141 (1996).

STUDIA UNIVERSITATIS BABEŞ-BOLYAI, PHYSICA, L, 2, 2005

HEAT GENERATION AND TEMPERATURE PROFILE IN IBA CYCLOTRON TL-TARGETS FOR HOMOGENEOUS TARGET CURRENT DENSITY

PIERRE VAN DEN WINKEL[1],L. DARABAN[2]

ABSTRACT. The use of a cylindrical collimator in stead of a square one, for IBA cyclotron. Tl-targets reduces the maximum target current by a factor 1,49. In any case the beam current density on target is limited to 0,493 μA.mm^{-2}. Taking into account the θ (6°) beam target geometry, the maximum current density at the collimator cross section area is donne for a gaussian current distribution. The reduction of the thickness of the Cu carrier to 0,5 mm allows the total target current to increased to 495 μA (cylindrical collimator) and to 738 μA for a square collimator, total target current in case of homogeneous irradiation i.e. a factor of 1,91 higher then when a cylindrical collimator and 2 mm Cu-backing are used. The sophisticated fin-fitted target carrier can be replaced by a simple flat backing: the cross sectional area O equals 0,300 cm^2 for a channel width of 2,5 mm, an area that is really equal to that of the fin-fitted version (O = 0,317 cm^2). Due to the reduced surface area of the ellipse, the total target current is limited to 495 μA. At the collimator outlet plane the maximum current density equals 6,31 μA.mm^{-2}. Reducing the Cu backing from 2 mm to 0,5 mm and doubling the flowrate of the coolant allows the current density to be increased by a factor 1,96. At the collimator exit plane the maximum current density equals 9,65 μA.mm^{-2}.

1. The model

The IBA Tl target can be considered as a three-layer system facing the accelerator vacuum one side and the coolant fluid on the other (see Fig. 1.)

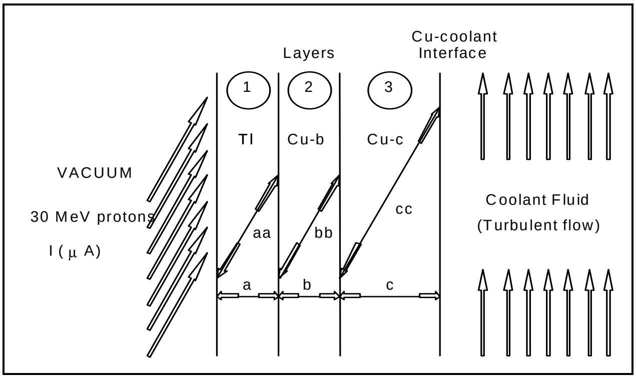

Fig. 1. The three layer system.

---

[1]. Enheid Cyclotron, Vrije Universiteit Brussel, Belgium

[2]. Faculty of Physics, University Babes-Bolyai, Cluj-Napoca,Romania

Layer ①, the ^{203}Tl deposit, has a physical thickness of 80.10^{-4} cm. In this layer ^{201}Pb is produced by the ^{203}Tl(p,3n)^{201}Pb threshold reaction provoked by 30 MeV protons [1], impinging under a θ° beam-target angle. Due to excitation, ionization and bremstralung, protons do loose kinetic energy in this layer that is converted into heat. Assuming homogeneous irradiation i.e. the current density (□A.mm^{-2}) is constant over the whole surface area S (= 11,69 cm^2) the total heat production rate q_{Tl} (J.s^{-1}) and the heat production rate per unit of volume q'''_{Tl} (J.cm^{-3}.s^{-1}) in this layer are related as :

$$q_{Tl} = q'''_{Tl} * a * S \tag{1}$$

Layer-②, The Cu-b layer, has a physical thickness of b cm. In this layer protons emerging from the Tl layer are stopped completely. The heat production rate q_{Cu} and the heat production rate per unit of volume q'''_{Cu} in this layer are linked by:

$$q_{Cu} = q'''_{Cu} * b * S \tag{2}$$

Layer ③, the Cu-c layer, has a physical dimension of c cm and merely serves as mechanical support for the Tl layer. The total heat (q_T) produced in the layers ① and ② is transferred to the coolant fluid through this layer by conduction.

$$q_T = q_{Tl} + q_{Cu} \tag{3}$$

At the Cu-c/coolant interface, the heat is transferred to the coolant by convection solely i.e. no subcooled nucleate boiling occurs and the bulk temperature of the coolant is a constant (T_W) [2,3]. In steady state conditions, the heat and heat transfers do result in a temperature profile represented in Fig. 2.

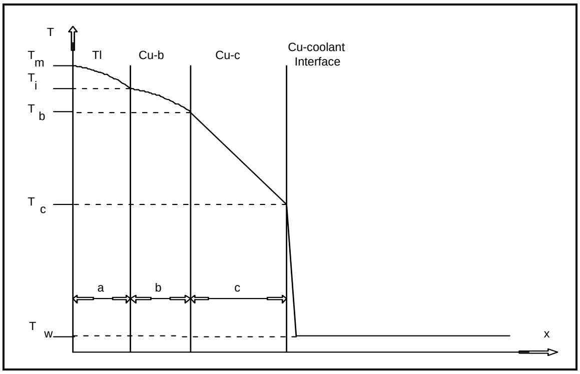

Fig. 2. *Temperature profile. where: T = temperature*

T_m = maximum temperature at the vacuum/Tl interface
T_l = temperature at the Tl/Cu-b interface
T_b = temperature at the Cu-b/Cu-c interface
T_c = temperature at the Cu-c/coolant interface
T_w = temperature of the coolant

The steady state temperature profile can be calculated applying :
-Poisson's equation to layers ① and ② where K represents the thermal conductivity of the metal involved in (J.cm^{-1}.s^{-1}.K^{-1}) and q$^{'''}$ is the heat production rate per unit volume in J.cm^{-3}.s^{-1}

$$\frac{d^2T}{dx^2} = -\frac{q^{'''}}{K} \qquad (4)$$

-Laplace's equation to layer ③;

$$\frac{d^2T}{dx^2} = 0 \qquad (5)$$

-Newton's equation to the Cu-c/coolant interface

$$q_T = h * S * \Delta T \qquad (6)$$

Here h represents the convective heat transfer coefficient in J.cm^{-2}.s^{-1}.K^{-1}. Under turbulent flow conditions of the coolant h can be obtained from the Dittius-Boelter equation (7):

$$h = c * \frac{K_c}{D_e} * R_e^{\,m} * P_r^{\,n} \qquad (7)$$

where : c, m, n = constants
h = the convective heat transfer coefficient in J.cm^{-2}.s^{-1}.K^{-1}
R_e = Renold's number (dimensionless)
P_r = Prandtl's number
D_e = equivalent diameter of the coolant channel (cm)
K_c = conductivity of the coolant fluid in J.cm^{-1}.s^{-1}

2. The theoretical temperature profile

The temperature profile is easily obtained by integrating the Poisson and Fourrier equations by means of Laplace transformations introducing appropriate boundary conditions.

2.1. Layer ①

$$\frac{d^2T(x)}{dx^2} = -\frac{q_{Tl}^{'''}}{K_{Tl}} \tag{8}$$

with boundary conditions:

-T(0) = T_m i.e. maximum temperature at vacuum/Tl interface

-T'(0) = 0 i.e. no heat flow from vacuum into Tl layer

We solve eq.(8) by Laplace transforms.

For x = a; $T_a = T_i$

$$T_m - T_i = \frac{q_{Tl}^{'''}}{2.K_{Tl}}.a^2 \quad (0 \le x \le a) \tag{9}$$

Introducing the total heat production rate in the Tl layer (eq(1)) results in

$$T_m - T_i = \frac{q_{Tl}}{2.K_{Tl}}.\frac{a}{S} \quad (0 \le x \le a) \tag{10}$$

2.2. Layer ②

$$\frac{d^2T(x)}{dx^2} = -\frac{q_{Cu}^{'''}}{K_{Cu}} \tag{11}$$

with boundary conditions:

-T(0) = $T(a)_{Tl} = T_i$ i.e. no temperature discontinuity at Tl/Cu-b interface

$-K_{Tl}.T^{'}(a)_{Tl} = K_{Tl}.(-\frac{q_{Tl}^{'''}}{K_{Tl}}.a) = K_{Cu}.T^{'}(0)_{Cu}$ and

$T^{'}(0) = T^{'}(0)_{Cu} = -\frac{q_{Tl}^{'''}}{K_{Cu}}.a$ i.e. heat generated in Tl layer quantitatively flows into the Cu-b layer at the Tl/Cu-b interface.

Laplace transform of eq (11) gives for x = b; T(x) = T_b and (a ≤ x ≤ b):

$$T_i - T_b = \frac{q_{Tl}^{'''} * a * b}{K_{Cu}} + \frac{q_{Cu}^{'''}}{2 * K_{Cu}} . b^2 \tag{12}$$

Introducing the total heat production rates results in :

$$T_i - T_b = \frac{q_{Tl}}{K_{Cu}} . \frac{b}{S} + \frac{q_{Cu}}{2 * K_{Cu}} . \frac{b}{S} \tag{13}$$

2.3. Layer③

$$\frac{d^2T(x)}{dx^2} = 0 \tag{14}$$

-T(0) = $T(b)_{Cu\text{-}b}$ = T_b i.e. no temperature discontinuity at Cu-b/Cu-c interface

- $K_{Cu}.T^{'}(b)_{Cu-b} = K_{Cu}.T^{'}(0)$ and $T^{'}(0) = T^{'}(b)_{Cu-b} = -\frac{q_{Tl}^{'''}}{K_{Cu}}.a - \frac{q_{Cu}^{'''}}{K_{Cu}}.b$

i.e. total heat ge-nerated in Tl layer and Cu-b layer quantitatively flows into the Cu-c layer at the Cu-b/Cu-c interface.

Inverse Laplace transform gives for x = c; T(x) = T_c :

$$T_b - T_c = (\frac{q_{Tl}^{'''} * a}{K_{Cu}} + \frac{q_{Cu}^{'''} * b}{K_{Cu}}) \cdot c \tag{15}$$

Introducing the total heat production rates results in :

$$T_b - T_c = \frac{q_T}{K_{Cu}} . \frac{c}{S} \tag{16}$$

2.4. At the Cu-c/coolant interface

$$q_T = h * S * (T_c - T_w) \tag{17}$$

where : $q_T = q_{Tl} + q_{Cu}$ ($J.s^{-1}$)
h = convective heat transfer coefficient ($J.s^{-1}.cm^{-2}.K^{-1}$)
T_c = temperature in Cu-c layer at x = c
Tw = bulk temperature of the coolant

Hence:

$$T_c - T_w = \frac{q_T}{h*S} \tag{18}$$

from the above it follows:

$T_m - T_i = \frac{q_{Tl}}{2.K_{Tl}}.\frac{a}{S}$ (eq. 10) i.e. temperature decrement over Tl layer

$T_i - T_b = \frac{q_{Tl}}{K_{Cu}}.\frac{b}{S} + \frac{q_{Cu}}{2*K_{Cu}}.\frac{b}{S}$ (eq. 13) i.e. temperature decrement over Cu-b layer

$T_b - T_c = \frac{q_T}{K_{Cu}}.\frac{c}{S}$ (eq. 16) i.e. temperature decrement over Cu-c layer

$T_c - T_w = \frac{q_T}{h*S}$ (eq. 18) i.e. temperature decrement at the Cu-c/coolant interface

Summing both sides results in :

$$T_m - T_w = \frac{q_{Tl}}{2*K_{Tl}}.\frac{a}{S} + \frac{q_{Tl}}{K_{Cu}}.\frac{b}{S} + \frac{q_{Cu}}{2*K_{Cu}}.\frac{b}{S} + \frac{q_T}{K_{Cu}}.\frac{c}{S} + \frac{q_T}{h*S} \tag{19}$$

-The values of q_{Tl}, q_{Cu} and q_T can be calculated from the beam current, the energy loss of protons per cm in Tl an Cu and the physical thickness of the layers (a and b).

-The value of h can be obtained as stated above from the Dittius Boelter equation (eq. 7)

3. The heat generation in Tl and Cu-b layers, heat transfer h and coolant bulk temperature (T_W)

3.1. The heat generation in Tl layer (q_{Tl} and q'''_{Tl})

The heat generation can be calculated from the mean energy loss per cm (L_{Tl}) of protons in the Tl layer and the total number of protons entering this layer. From the ^{203}Tl(p,3n)^{201}Pb excitation curve it follows that for 30 MeV protons entering the layer under a θ = 6° angle, the exit energy is 21 MeV. Therefore, L_{Tl} is given by :

$$L_{Tl} = \frac{\Delta E_p}{\overline{a}\overline{a}} = \frac{\Delta E_p}{a} * \sin\theta = \frac{9(MeV)}{8.10^{15}(cm)} * 0{,}1 = 112{,}5(\frac{MeV}{cm}) \tag{20}$$

$$L_{Tl} = 0,018.10^{-9}(\frac{J}{cm})$$

The total number (N) of protons entering the layer per second, can be calculated from the beam current I (µA) and the charge of the protons q_p (C)

$$N = \frac{I*10^{-6}(\frac{C}{s})}{q_p(C)} = \frac{10^{-6}}{1,6.10^{-19}} = 6,25.10^{12}*I(s^{-1}) \qquad (21)$$

The total heat generation per s is then given by :

$$q_{Tl} = L_{Tl}*\frac{a}{\sin\theta}*N = \frac{6,25.10^{12}*0,018.10^{-9}*8.10^{-3}*I}{0,1} = 9,0*I \qquad (22)$$

The heat generation per unit of volume and time equals :

$$q'''_{Tl} = \frac{q_{Tl}}{a*S} = \frac{9*I}{8.10^{-3}*11,69} \qquad (23)$$

where S = surface of the Tl layer = 11,69 cm^2.

$$q'''_{Tl} = 96,2*I(J.cm^{-3}.s^{-1}) \qquad (24)$$

3.2. The heat generation in Cu-b layer (q_{Cu} and q'''_{Cu})

The Cu-b layer has a physical thickness b (cm) such that the 21 MeV protons entering the layer under a θ = 6° angle are completely stopped.
The range of 21 MeV protons in Cu equals 850 µm = $\bar{b}\bar{b}$.

Hence

$$b = \bar{b}\bar{b}*\sin\theta = 85.10^{-4}\,cm \qquad (25)$$

and

$$L_{Cu} = \frac{\Delta E'_p}{\bar{b}\bar{b}} = \frac{\Delta E'_p}{b}*\sin\theta = \frac{21(MeV)}{85.10^{14}(cm)}*0,1 = 247(\frac{MeV}{cm}) \qquad (26)$$

$$L_{Cu} = 0,0359.10^{-9}(\frac{J}{cm})$$

The total number (N) of protons entering the layer per second being given by

$$N = 6{,}25.10^{12} * I(s^{-1}) \tag{27}$$

The total heat generation per s is then given by :

$$q_{Cu} = L_{Cu} * \frac{b}{\sin\theta} * N = \frac{6{,}25.10^{12} * 0{,}0395.10^{-9} * 85.10^{-4} * I}{0{,}1} = 21 * I(\frac{J}{s}) \tag{28}$$

The heat generation per unit of volume and time equals :

$$q_{Cu}^{'''} = \frac{q_{Cu}}{b * S} = \frac{21 * I}{85.10^{-4} * 11{,}69} \tag{29}$$

and

$$q_{Cu}^{'''} = 211 * I(\frac{J}{s.cm^3})$$

3.3. Total heat generation (q_T)

The total heat generation q_T ($J.s^{-1}$) is the sum of the heat production rates in the Tl and the Cu-b layer

$$q_T = q_{Tl} + q_{Cu} = 9 * I + 21 * I \tag{30}$$

$$q_T = 30 * I(\frac{J}{s}) \tag{31}$$

3.4. Convective heat transfer coefficient h.

Assuming turbulent convective cooling only - i.e. no subcooled nucleate boiling occurs - at the Cu-c/coolant interface, the temperature difference T_c - T_w can be calculated by Newton's equation

$$q_T = h * S * (T_c - T_w) \tag{32}$$

3.4.1. The condition for turbulent cooling flow is governed by the magnitude of the Reynolds's number R_e.

$$R_e = \frac{D_e * v * \rho}{\mu} \tag{33}$$

where: D_e = equivalent diameter of coolant channel (cm)
v = average linear velocity of coolant (cm.s^{-1})
ρ = density of coolant (=1)
μ = fluid viscosity (cm^2.s^{-1}) = 1.10^{-2} cm^2.s^{-1}

The value of D_e is given by :

$$D_e = 4 * \frac{cross - sectional - area - of - coolant - channel}{wetted - perimeter - of - the - coolant - channel} = 4 * \frac{O}{L} \qquad (34)$$

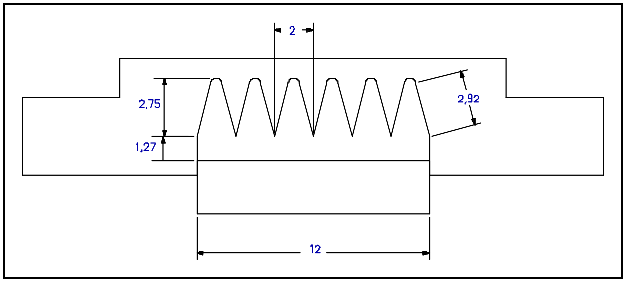

Fig 3. IBA Tl target with fins

For IBA targets it follows from Fig. 3.

$$O = 0{,}317\,cm^2 \qquad L = 4{,}95\,cm \qquad D_e = 0{,}256\,cm$$

The value of v can be obtained from the applied flow rate f (50 l/min or 833 cm^3/s) and the cross sectional area (0,317 cm^2) of the coolant channel

$$v = \frac{f}{O} = 2627\left(\frac{cm}{s}\right) \qquad (35)$$

Introducing D_e, v, ρ and μ in eq(33) $\quad R_e = 67251$

As R_e >> 10000, the coolant moves in fully developed turbulent flow.

3.4.2. Convective heat transfer coefficient h.

Apart from the R_e number, the Nusselt (N_u) and the Prandtl (P_r) numbers are required for application of the Dittius-Boelter equation with :

$$N_u = \frac{h * D_e}{k_{H_2O}} \qquad (36)$$

with: D_e = equivalent diameter of the coolant channel (0,256 cm)

h = convective heat transfer coefficient $(\frac{J}{s*cm^2*K^\circ})$

k_{H2O} = conductivity of the coolant fluid $0{,}597.10^{-2}(\frac{J}{s*cm*K^\circ})$

and

$$P_r = \frac{c_p*\mu}{k_{H_2O}} \tag{37}$$

and c

and c_p = specific heat of coolant fluid $4{,}18(\frac{J}{cm^3*K^\circ})$

μ = viscosity of coolant fluid (cm^2/s)

Hence: $P_r = 7{,}0$

Under turbulent conditions :

$$N_u = \frac{h*D_e}{k_{H_2O}} = c*R_e{}^m*P_r{}^n \tag{38}$$

and

$$h = c*\frac{k_{H_2O}}{D_e}*R_e{}^m*P_r{}^n \tag{39}$$

With: c = 0,023
m = 0,8
n = 0,4

$$h = 0{,}023*\frac{0{,}597*10^{-2}}{0{,}256}*67{,}25^{0,8}*7{,}0^{0,4} = 8{,}5(\frac{J}{s*cm^2*^\circ K}) \tag{40}$$

3.5. Coolant bulk temperature (T_w).

Under adiabatic conditions, the bulk temperature can be calculated from the total heat generation (q_T) and the flow rate f ($cm^3.s^{-1}$) of the coolant

$$T_W = \frac{q_T}{c_p*f} + T_i \tag{41}$$

With: T_i = the coolant temperature at the inlet of the coolant channel = 21° C
c_p = specific heat of the coolant 4,18 ($J.cm^{-3}.K^{-1}$)
f = flow rate = 833 $cm^3.s^{-1}$
With q_T = 30 * I (eq(31)), eq (42) results in :

$$T_W = \frac{30*I}{c_p * f} + T_i = 21 + 0{,}0086*I \qquad (42)$$

Neglecting the influence of I, T_w = 21° C

3.6. Summary

For the application of eq(19) the following values are to be taken into account

a	80.10^{-4} cm	(43)
b	85.10^{-4} cm	
c	0.2 cm	
q_{Tl}	9 * I $J.s^{-1}$	(44)
q_{Cu}	21 * I $J.s^{-1}$	
q_T	30 * I $J.s^{-1}$	
K_{Tl}	0,461 $J.s^{-1}.cm^{-1}.K^{-1}$	(45)
K_{Cu}	4,0 $J.s^{-1}.cm^{-1}.K^{-1}$	
h	8,5 $J.s^{-1}.cm^{-2}.K^{-1}$	(46)
T_m	275° C = temperature of thermal shock quality test	(47)
T_W	21 + 0,0086 * I	(48)

4. Current temperature profile as a function of total target current - maximum current density i (µA/mm²) tolerated by IBA-Tl targets

Introducing the values (43) - (48) in eq(19) from the above Table i.e.

$$T_m - T_w = (T_m - T_i) + (T_i - T_b) + (T_b - T_c) + (T_c - T_w) \qquad (49)$$

and introducing the total target current I

$$T_m - T_w = (\frac{9*I}{2.K_{Tl}}.\frac{a}{S}) + (\frac{9*I}{K_{Cu}}.\frac{b}{S} + \frac{21*I}{2*K_{Cu}}.\frac{b}{S}) + (\frac{30*I}{K_{Cu}}.\frac{c}{S}) + (\frac{30*I}{h*S}) \qquad (50)$$

for 2 mm Cu backing

$$T_m - T_w = 0{,}00668 \ * I + 0{,}00354 \ * I + 0{,}1283 \ * I + 0{,}3019 \ * I \qquad (51)$$

and

$$T_m - T_i = 0{,}00668\ * I \tag{52}$$

$$T_i - T_b = 0{,}00354\ * I \tag{53}$$

$$T_b - T_c = 0{,}1283\ * I \tag{54}$$

$$T_c - T_m = 0{,}3019\ * I \tag{55}$$

Calculations of temperature as a function of the total target current are summarized in Table 1

Table 1.

Temperature decrements over IBA-Tl targets
Homogeneous irradiation and c = 0,2 cm

I(µA)	T_m-T_i	T_i-T_b	T_b-T_c	T_c-T_w	T_m-T_w
100	0,668	0,354	12,830	30,19	44,04
200	1,336	0,706	25,660	60,380	88,08
300	2,004	1,062	38,490	90,57	132,12
400	2,672	1,416	51,320	120,76	176,16
500	3,340	1,770	64,150	150,95	220,2
600	4,008	2,124	76,980	181,14	264,2
700	4,676	2,478	89,810	211,33	308,3
800	5,344	2,832	102,640	241,52	352,3
900	6,012	3,186	115,470	271,71	396,4
1000	6,680	3,540	128,300	301,9	440,4

Eq(51) gives:

$$T_m - T_w = 0{,}440 * I \tag{56}$$

and

$$I_m = \frac{T_m - T_w}{0{,}440} = \frac{T_m - T_w}{K} \tag{57}$$

i.e. for a given acceptable temperature difference T_m - T_w, the maximum current tolerated by IBA-Tl targets is given by eq(58). For T_m = 275° C and T_i = 21° C, I_m = 577 µA and the maximum tolerated current density equals:

$$i_m = \frac{I_m}{S} = \frac{577}{1169} = 0{,}493 \mu A.mm^{-2} \tag{58}$$

4.1. Influence of the collimator geometry.

Eq(57) is valid for homogenous irradiation of the complete target surface S i.e. 11,69 cm^2. As a cylindrical collimator is used, only the surface area of an ellipse - 6° projection of a circle with radius R = 5 mm - is irradiated.

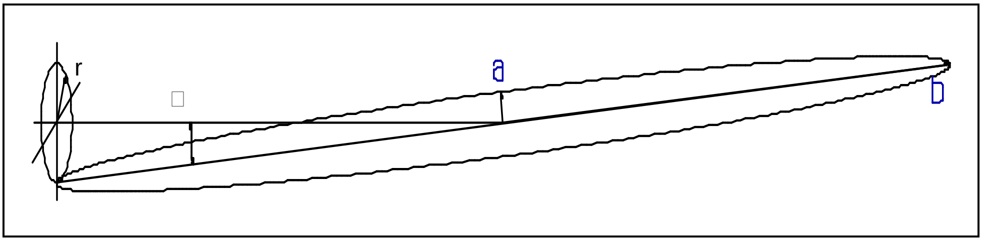

Fig. 4. The 6° projection of a circle with radius R

The axes a = R = 0,5 cm

b = R/sinθ = 5 cm

and the surface area

$$O = \pi . a . b = 7{,}85 cm^2 = 785 mm^2 \tag{59}$$

and

$$I_m^{'} = i_m * O = 0{,}493 * 785 = 387 \mu A \tag{60}$$

In conclusion : The use of a cylindrical collimator in stead of a square one, reduces the maximum target current by a factor 1,49. In any case the beam current density on target is limited to 0,493 μA.mm^{-2}. Taking into account the θ (6°) beam target geometry, the maximum current density at the collimator cross section area equals: i_m = 4,93 μA·mm^{-2}.

and

$$i(r) = 4{,}93 * e^{-a^2 r^2} \tag{61}$$

for a gausian current distribution.

4.2. Influence of the thickness c of the Cu carrier on the maximum target current

The influence of the thickness of c = 2 mm for calculation of eq(68) and eq(75)) on the maximum target current can be calculated from eq(68), putting c = 3, 2, 1, 0,5 and 0 mm.

Table 2.
Influence of the thickness c of the Cu carrier
on the maximum target current

c (mm)	K	I_m (square collimator)	I'_m (Cylindrical collimator)
3	0,504	503	337
2	0,440	577	387
1	0,376	675	453
0,5	0,344	738	495
0	0,312	814	546

We conclude that: the reduction of the thickness of the Cu carrier to 0,5 mm allows the total target current to increased to 495 μA (cylindrical collimator) and to 738 μA for a square collimator. Use of a square collimator and of a Cu-c backing of 0,5 mm allows a total target current of 738 μA in case of homogeneous irradiation i.e. a factor of 1,49 * 1,28 = 1,91 higher then when a cylindrical collimator and 2 mm Cu-backing are used. In the extreme case Cu-c = 0 mm and total Cu backing Cu-b + Cu-c = 85 μm, the total current burden of the target is increased to 814 μA i.e. a gain of a factor 2,10.

4.3. Influence of the nature of the Tl-carrier

In the above, the Tl carrier was assumed to be Cu showing a thermal conductivity of 4 $J.s^{-1}.cm^{-1}.K^{-1}$. Substituting Cu for Ag could enhance the maximum permissible target current slightly (K_{Ag} = 4,294 $J.s^{-1}.cm^{-1}.K^{-1}$) but enormously increases the price of the carrier [4]. However, if it were possible to manufacture a pyrolytic graphite carrier for which heat transfer occurs parallel to the layer plans ((K_C= 19,5 4 $J.s^{-1}.cm^{-1}.K^{-1}$) and if it is possible to plate Tl on a graphite backing with current efficiency and layer quality similar to that obtained with Cu carriers, the maximum permissible target current could be increased by a factor 1,32.

Indeed, resuming eq(50) and substituting K_C for K_{Cu} gives eq(62)

$$T_m - T_w = (\frac{9*I}{2.K_{Tl}}.\frac{a}{S}) + (\frac{9*I}{K_C}.\frac{b}{S} + \frac{21*I}{2*K_C}.\frac{b}{S}) + (\frac{30*I}{K_C}.\frac{c}{S}) + (\frac{30*I}{h*S}) \qquad (62)$$

with: a = 8010^{-4} cm
b = 0,07 cm (Range of 30 MeV protons in C = 7 mm)
c = 0,13 cm (2 mm graphite backing)

K_{Tl} = 0,461 J.s^{-1}.cm^{-1}.K^{-1}
K_C = 19,5 4 J.s^{-1}.cm^{-1}.K^{-1}
S = 11,69 cm^2
h = 8,8 J.s^{-1}.cm^{-1}.K^{-1}
T_m = 275° C (= maximum temperature for thermal shock quality test)
T_w = 21° C

Substituting these values on eq(62) yields

$$T_m - T_w = 0{,}00668 \ * I + 0{,}00276 \ * I + 0{,}0171 * I + 0{,}3019 \ * I \qquad (63)$$

and

$$T_m - T_w = 0{,}332 * I_m \qquad (64)$$

We deduce:

$$I_m = \frac{T_m - T_w}{0{,}332} \qquad (65)$$

I_m =765 µA.

Eq(65) gives the maximum permissible target current burden for homogeneous irradiation using a 2 mm C backing.

In conclusion : As compared to a 2 mm Cu backing the maximum current gain equals 765/577 (Table 2 square collimator) = 1,32 i.e. substituting a 2 mm Cu backing for a 2 mm C backing results in about the same gain as the reduction of the Cu backing from 2 mm to 0,5 mm (g = 1,28). Reduction of the thickness of Cu backing is to preferred from practical point of view.

4.4. Influence of the geometry of the coolant channel and of the linear flow of the coolant

4.4.1. Omitting the fins The calculation of the convective heat transfer coefficient was done for the fin-fitted target carrier represented in Fig. 3. Omitting the fins and reducing the channel width to 2,5 mm gives an effective diameter D_e :

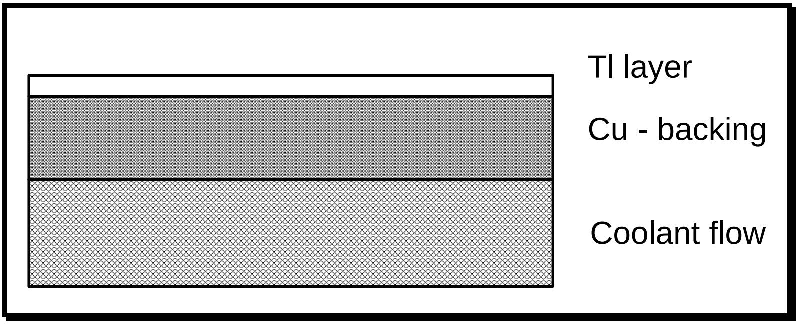

Fig 5. The coolant channel

$$D_e = 4 * \frac{O}{L} = 4 * \frac{1{,}2 * 0{,}25}{2 * 1{,}45} = 0{,}413\,cm \tag{66}$$

The linear flow rate then equals :

$$v = \frac{f}{O} = \frac{833\,cm^3.s^{-1}}{0{,}300\,cm^2} = 2776\,cm.s^{-1} \tag{67}$$

and R_e number

$$R_e = \frac{D_e * v * \rho}{\mu} = \frac{0{,}413 * 2776 * 1}{1.10^{-2}} = 114648 \tag{68}$$

As R_e >> 10000 the flow is turbulent
With:

$$P_r = \frac{c_p * \mu}{K_{H_2O}} = \frac{4{,}18.10^{-2}}{0{,}597.10^{-2}} = 7{,}0 \tag{69}$$

the convective heat transfer coefficient h is given by:

$$h = 0{,}023 * \frac{K_{H_2O}}{D_e} * R_e^{\;0{,}8} * P_r^{\;0{,}4} \tag{70}$$

and we obtain:

$$h = 8{,}04\,J.cm^{-1}.s^{-1}.K^{-1}$$

Compared with the h value obtained for the fin-fitted carrier (h = 8,5) the h value is only 5% less.

In conclusion: the sophisticated fin-fitted target carrier can be replaced by a simple flat backing: the cross sectional area O equals 0,300 cm^2 for a channel width of 2,5 mm, an area that is really equal to that of the fin-fitted version (O = 0,317 cm^2).

4.4.2. Doubling the coolant flow rate (f = 1666 $cm^3.s^{-1}$) gives:

$$v = \frac{1666}{0{,}300} = 5553\,cm.s^{-1}$$

$$R_e = \frac{D_e * v * \rho}{\mu} = \frac{0{,}413 * 5553 * 1}{1.10^{-2}} = 229398 \qquad (71)$$

With a Prandtl number equal to 7,0, the convective heat transfer coefficient h is given by :

$$h = 0{,}023 * \frac{0{,}597.10^{-2}}{0{,}413} * 229538^{0,8} * 7^{0,4} \qquad (72)$$

$$h = 14\ J.cm^{-1}.s^{-1}.K^{-1}$$

Therefore:doubling the flow rate nearly doubles the convective heat transfer coefficient

4.5. Influence of the nature of the coolant-charge to subcooled nucleate boiling regime.

From the above it is obvious that the thermal resistance at the Cu-c/coolant interface is the major limiting factor as far as the maximum target current is concerned. Therefore, the use of a coolant with melting point much less than 0° C could be envisaged allowing the T_m -T_w value to be increased. One such coolant is glycol (CH_2OH-CH_2OH). The physical properties of this coolant fluid are as follows:

T_{melt} = -13° C
T_{boil} = 197° C
ρ = 1,11
c_p = 2,39 $J.g^{-1}.K^{-1}$ = 2,65 $J.cm^{-3}.K^{-1}$
K_{glycol} = 0,25 $J.s^{-1}.m^{-1}.K^{-1}$ = 0,0025 $J.s^{-1}.cm^{-1}.K^{-1}$
Dynamic viscosity = μ_D = 16,1.10^{-3} Pa.s

Kinematic viscosity $\mu = \dfrac{\mu_D}{\frac{kg}{m^3}} = \dfrac{16{,}1.10^{-3}}{1110} = 0{,}145 cm^2 . s^{-1}$

Introducing these values in eq(33), (37) and (39), using an equivalent radius of the coolant channel D_e = 0,256 cm and a linear flow velocity of v = 2627 $cm.s^{-1}$ results in

$$R_e = \frac{D_e * v * \rho}{\mu} = \frac{0{,}256 * 2627 * 1{,}11}{0{,}145} = 5148 \tag{73}$$

As R_e <<10000 the coolant flow is not turbulent. To obtain turbulent flow, the linear flowrate should be doubled at least.
For v = 5254 $cm.s^{-1}$ (100 $l.min^{-1}$) $R_e = 10296 > 10000.$
The Prandtl number equals:

$$P_r = \frac{c_p * \mu}{K_{glycol}} = \frac{2{,}65 * 0{,}145}{0{,}0025} = 153 \tag{74}$$

Therefore the convective heat transfer coefficient is given by

$$h = 0{,}023 * \frac{K_{glycol}}{D_e} * (R_e)^{0,8} * (P_r)^{0,4} \tag{75}$$

and $h = 2{,}72 (J.s^{-1}.cm^{-2}.K^{-1})$ results:

The value of h is more then 3 times less than the one for water. Hence, glycol is not suited at all. Change the coolant from H_2O to $CH_2OH\text{-}CH_2OH$ is not acceptable at all. The same holds for other classical coolants.
The only valuable recommendation is to use a coolant showing a low boiling point to take advantage of enhanced heat exchange by subcooled nucleate boiling of the coolant. NH_3 could be used for this purpose. Technical problems such as complex formation ($Cu(NH_3)_4^{++}$) make this option less attractive.

5. Maximum permissible target current density for homogeneous irradiation of IBA Tl targets when Cu-c is reduced to 0,5 mm (0,05 cm)

Resuming eq(50): with the above values we obtains:

$$T_m - T_w = (\frac{9*I}{2.K_{Tl}}.\frac{a}{S}) + (\frac{9*I}{K_{Cu}}.\frac{b}{S} + \frac{21*I}{2*K_{Cu}}.\frac{b}{S}) + (\frac{30*I}{K_{Cu}}.\frac{c}{S}) + (\frac{30*I}{h*S}) \quad (76)$$

with: a = 80.10^{-4} cm
b = 85.10^{-4} cm
c = 0,05 cm
K_{Tl} = 0,461 $J.s^{-1}.cm^{-1}.K^{-1}$
K_{Cu} = 4,0 $J.s^{-1}.cm^{-1}.K^{-1}$
S = 11,69 cm^2
h = 8,5 $J.s^{-1}.cm^{-1}.K^{-1}$
T_m = 275° C (= maximum temperature for thermal shock quality test)
T_w = 21° C

Introducing in (69) eq.we obtained: $I_m = 738 \mu A$

and the maximum current density equals $i_m = 0{,}631 \mu A.mm^{-2}$

Conclusion: Reducing the Cu-backing from 2 mm to 0,5 mm allows the current density to be increased by a factor 0,631/0,493 = 1,28 i.e. 28% increase. Due to the reduced surface area of the ellipse, the total target current is limited to 0,631 * 785 = 495 µA. At the collimator outlet plane the maximum current density equals 6,31 $\mu A.mm^{-2}$.

6. Maximum permissible target current density for homogeneous irradiation when Cu backing is reduced to 0,5 mm and the flowrate of the coolant is doubled (100 $l.min^{-1}$)

Resuming eq(50) $I_m = 1128 \mu A$

and the maximum current density equals $i_m = 0{,}965 \mu A.mm^{-2}$

Conclusion: Reducing the Cu backing from 2 mm to 0,5 mm and doubling the flowrate of the coolant allows the current density to be increased by a factor 0,965/0,496 = 1,96. At the collimator exit plane the maximum current density equals 9,65 $\mu A.mm^{-2}$. This project was applied by [4].

REFERENCES

1. S.M. Quaim, R. Weinreich, H. Ollig, *Production of* ^{201}*Tl and* ^{203}*Pb via proton induced nuclear reactions on natural thalium*, Int.J.Appl.Radiat.Isot., **30**, 85-97(1979)
2. R.F. Seiler, M.R. Cleland, H.E. Wegner, Rev.Sci.Instr., **38**, 972 (1967)
3. I.E. Teodorescu, *Generatoare de neutroni*, Ed. Acad.RSR, p.161, Bucuresti (1969)
4. G.Raisali*, Production of medical radioisotopes in NRCAM using Cyclone 30*, The 5 ICI Conference on Isotopes, Brussels, Belgium, 25- 29 april, Abstract Conference, p.4-5 (2005).

STUDIA UNIVERSITATIS BABEŞ-BOLYAI, PHYSICA, L, 2, 2005

NON HOMOGENEOUS CYCLOTRON TARGET IRRADIATION: GAUSSIAN CURRENT DENSITY DISTRIBUTION - CYLINDRICAL COLLIMATOR

P. VAN DEN WINKEL[1], L. DARABAN[2]

Abstract: When a Gaussian current density distribution without wobbling is applied and a 400 μA accelerator current is possible, the maximum permissible current equals 247 μA, i.e. 37,7 % of the available accelerator current is collected on the collimator. The cyclotron operator should adjust the accelerator parameters, such that conditions given by the deduced equations are satisfied. When a^2 = 0,108 (value used in IBA calculations) the present IBA-Karadj target only tolerates a maximum current of 133,8 μA (a value that is confirmed experimentally) when no wobbling is applied. The current density distribution in that case is also represented.

1. Beam- (I_B) and target (I_T) current and beam current efficiency

Assuming a gaussian current density distribution at the exit of a cylindrical collimator i.e. [1]

$$i = i_m . e^{-a^2 r^2} \qquad (1)$$

with:

i_m = maximum current density (μA.mm^{-2})
a^2 = gaussian exponent (mm^{-2})
r = radial distance from collimator circle

The total beam current I_B is given by :

$$I_B = \int_0^\infty i_m . e^{-a^2 . r^2} .2.\pi.r.dr = -\frac{\pi * i_m}{a^2} . \int_0^\infty d(e^{-a^2 . r^2}) = \frac{\pi * i_m}{a^2} \qquad (2)$$

and the target current I_T

$$I_T = \int_0^R i_m . e^{-a^2 . r^2} .2.\pi.r.dr = -\frac{\pi * i_m}{a^2} . \int_0^R d(e^{-a^2 . r^2}) \qquad (3)$$

---

[1] Enheid Cyclotron, Vrije Universiteit Brussel, Belgium
[2] Faculty of Physics, University Babes-Bolyai, Cluj-Napoca, Romania

$$I_T = \frac{\pi * i_m}{a^2}(1 - e^{-a^2.R^2}) \tag{4}$$

The beam current efficiency ε_B can be defined as

$$\varepsilon_B = \frac{I_T}{I_B} = (1 - e^{-a^2.R^2}) * 100 \tag{5}$$

i.e. the percentage of the total beam current sticking the target.
From experimental point of view, target I_T and collimator I_C are measured

$$I_C = I_B - I_T = \frac{\pi * i_m}{a^2}.e^{-a^2.R^2} \tag{6}$$

and

$$\frac{I_B}{I_C} = e^{-a^2.R^2} \tag{7}$$

and

$$a^2 = \frac{1}{R^2} * \ln(\frac{I_B}{I_C}) = \frac{1}{R^2} * \ln(\frac{I_T + I_C}{I_C}) \tag{8}$$

Substituting eq. (8) in eq. (2) yields :

$$i_m = \frac{1}{\pi * R^2} + (I_T + I_C) * \ln(\frac{I_T + I_C}{I_C}) \tag{9}$$

From eq. (8) and (9) it follows for a given collimator radius, i_m and a^2 can be calculated from the measured target and collimator currents.
Example: For the Karadj targets (R = 5 cm), I_C = 25 µA and I_T = 350 µA. Hence

$$a^2 = \frac{1}{R^2} * \ln(\frac{I_B}{I_C}) = \frac{1}{5^2} * \ln(\frac{375}{25}) = 0{,}108(mm^{-2}) \tag{10}$$

$$i_m = \frac{1}{\pi * R^2} + (I_T + I_C) * \ln(\frac{I_T + I_C}{I_C}) = \frac{1}{\pi * 5^2} + (350 + 25) * \ln(\frac{350 + 25}{25}) = 12{,}93(\mu A.mm^{-2}) \tag{11}$$

$$\varepsilon_B = \frac{I_T}{I_B} * 100 = \frac{350}{375} * 100 = 93{,}3\% \tag{12}$$

1.1. Influence of the gaussian exponent a^2 on the current efficiency ε_B and the maximum permissible target current ($I_{T,m}$)

In Table 1 the beam current efficiency is represented as a function of a^2. In the same table $I_{T,m}$ for i_m = 4,93 μA and $I_{T,m}/\varepsilon_B$ are summarized in

Table 1.

Beam current efficiency ε_B and I_T/i_m as a function of a^2

a^2 (mm^{-2})	ε_B (%)	I_T/i_m (mm^2)	$I_{T,m}$ (μA)	$I_{B,m}$ (μA)	RA
0,200	99,3	15,60	76,9	77,4	5,03
0,150	97,6	20,45	100,8	103,3	3,84
0,108	93,3	27,13	133,8	143,4	2,89
0,100	91,8	28,83	142,1	154,8	2,72
0,090	89,5	31,23	153,9	171,9	2,51
0,080	86,5	33,95	167,4	193,5	2,31
0,070	82,6	37,10	182,9	224,9	2,12
0,060	77,7	40,67	200,5	254,0	1,93
0,050	71,3	44,82	220,9	309,8	1,75
0,040	63,2	49,65	244,7	387,2	1,58
0,030	52,8	55,25	272,4	515,9	1,42
0,020	39,3	61,80	304,7	775,3	1,27

From the calculation in 4.1.,[1] it follows that for a 2 mm Cu backing, the maximum permissible current density at the collimator exit equals:

$$i_m = 4{,}93\,\mu A.mm^{-2}$$

By multiplying I_T/i_m with i_m, the maximum target current $I_{T,m}$ as a function of a^2 is obtained. Assuming a maximum beam current of 400 □A, [2,3], the smallest value of a^2 that can be applied practically, follows from the ε_B, $I_{T,m}$ combination that satisfies eq. (13)

$$I_{B,m} = \frac{I_{T,m}}{\varepsilon_B} = 400(\mu A) \tag{13}$$

Plotting $I_{T,m}/\varepsilon_B$ as a function of a^2 (Fig.1.) gives:

$a^2 = 0{,}039$
$\varepsilon_B = 62{,}28\%$
$I_T/i_m = 50{,}17$

$I_{T,m}$ = 247,3 µA
$I_{T,m}/\varepsilon_B$ = 397 µA ≅ 400 µA

This result can also be obtained directly from eq.(5), putting I_B = 400 µA and
i_m = 4,93µA.mm^{-2}.
Hence

$$a^2 = 0{,}0387(mm^{-2})$$

and

$$\varepsilon_B = 62{,}0\%$$

In general i_m, a^2 and the total accelerator output current I_B are related as follows :
From eq. (8) and eq. (9)

$$\frac{a^2}{i_m} = \frac{\pi}{I_B} \tag{9 bis}$$

For I_B = 392 µA (≅ 400µA

$$\frac{a^2}{i_m} = 0{,}080\mu A^{-1} \tag{14}$$

In conclusion:When a Gaussian current density distribution without wobbling is applied and a 400 µA accelerator current is possible, the maximum permissible current equals 247 µA. This target current is possible on conditions that:

$$i_m = 4{,}93\ \mu A.mm^{-2} \qquad a^2 = 0{,}039\ mm^{-2} \tag{15}$$

i.e. when:

$$I_T = 247\ \mu A \qquad I_C = 153\ \mu A \tag{16}$$

i.e. 37,7 % of the available accelerator current is collected on the collimator. The cyclotron operator should adjust the accelerator parameters, such that conditions given by eq.(15) or eq.(16) are satisfied. The current density distribution in this case is given in Fig 1.as I_{CAL}.

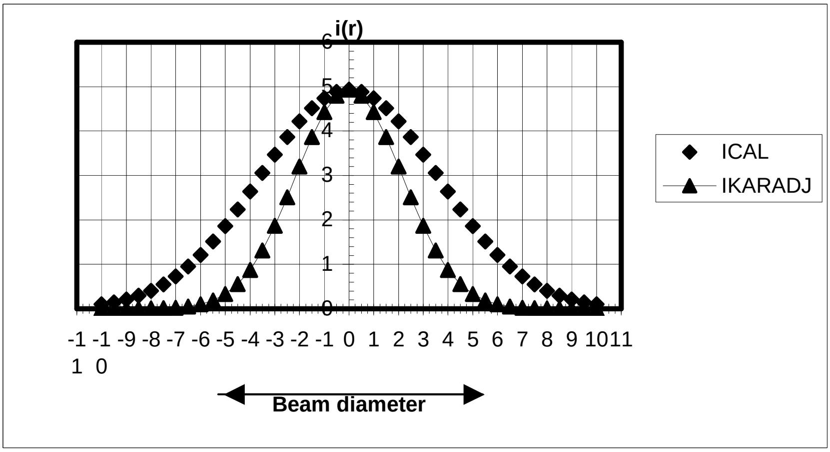

Fig 1. IBA Karadj Tl target

In IBA heat calculations it was assumed that

$$i_m = 13{,}93\ \mu A.mm^{-2}$$
$$a^2 = 0{,}108\ mm^{-2} \qquad (17)$$

or

$$I_T = 350\ \mu A$$
$$I_C = 25\ \mu A \qquad (18)$$

Comparison of eq.(17) and eq.(18) shows that the maximum current density is 2,6 times to high, which without wobbling, will result in local melting of the Tl. When a^2 = 0,108 (value used in IBA calculations) the present IBA-Karadj target only tolerates a maximum current of 133,8 µA (a value that is confirmed experimentally) when no wobbling is applied. The current density distribution in that case is also represented in Fig .1 as I_{KARADJ}.

1.2. Gaussian current density distribution versus homogeneous irradiation

In either case the total target current is limited by the maximum permissible current density i_m

For gaussian current density distribution

$$I_{T,G} = \frac{\pi * i_m}{a^2}(1 - e^{-a^2.R^2}) \qquad (19)$$

and for homogeneous irradiation with the same im:

$$I_{T,H} = \pi.R^2.i_m \qquad (20)$$

Therefore, the ratio of maximum permissible target currents is given by

$$R_A = \frac{I_{T,H}}{I_{T,G}} = \frac{a^2.R^2}{1-e^{-a^2.R^2}} \tag{21}$$

Hence, this ratio is a function of $a^2.R^2$ only. For low values of a^2, $1\text{-}e^{(-a2R2)} \cong a^2.R^2$ and

$$R_A = 1$$

i.e. for irradiations with gaussian current density distribution showing a large full width half maximum value, the total target current burdens approximate 1, resulting however in a low beam current efficiency. The R_A-values are for i_m = 4,93 μA.mm^{-2} also represented in Table 2 from [1]. From the practical point of view, R_A can be calculated from I_T and I_C measurements:

$$R_A = \frac{I_T + I_C}{I_T} * \ln\left(\frac{I_T + I_C}{I_C}\right) \tag{22}$$

as can be readily shown by substituting eq.(8) and eq.(9) into eq.(22). Graphically, R_A can be represented as a ratio of the volumes of a cylinder (R = radius of the Base, i_m = height) and the volume of a body of revolution obtained by rotation of the gaussian curve around the vertical axis. This property - total current proportional to volume - is used in the CIRCWOB.BAS code allowing current density distribution and total beam and target currents calculations by numeric integration for cylindrical collimators applying circular wobbling

2. Circular wobbling - Gaussian current density distribution

From the above it is obvious that with the present current density limit (4,93 μA.mm-2 $\cong$ 5 μA.mm^{-2}) at the collimator exit plane, the maximum target current is limited to 247 □A i.e. the beam efficiency is 62,2 % only (a^2 = 0,039). Further increases of the beam current can be obtained by circular wobbling. Therefore the gaussian distribution is shifted over a distance R_W, the wobler circle radius, from the collimator axis where after the proton beam is forced to rotate around the axis (Fig. 2).

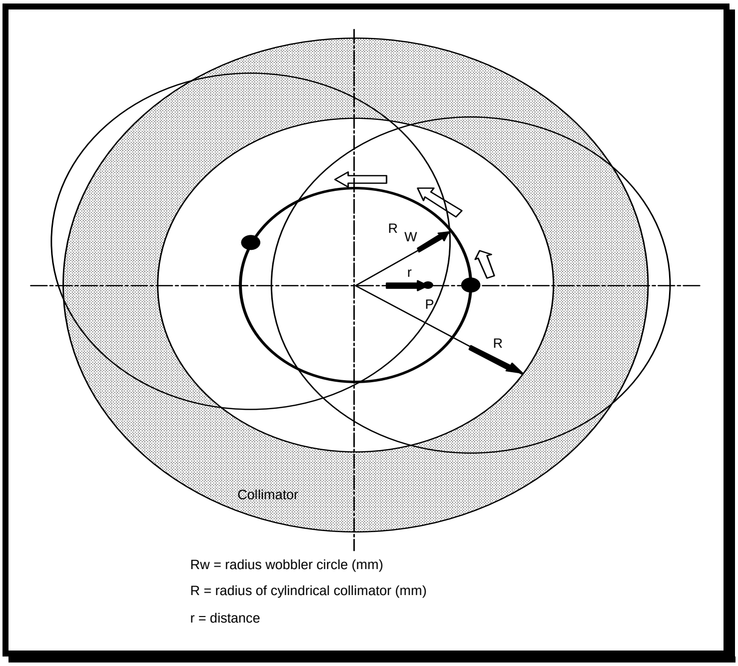

Fig 2. Circular Wobbling

Though a part of the beam is collected on the collimator body, further increase of the target current can be expected by optimizing the radius of the wobler circle.

The calculations of the mean current density distribution and of the total beam and target current cannot be done analytically: numeric integration is required. This is done by means of the CIRCWOB.BAS code, a qbasic program required as imput

i_0 = maximum current density (µA.mm^{-2})
a^2 = gaussian exponent (mm^{-2})
R = radius of the collimator (5mm)
I_{RCW} = increment of radius of wobbler circle (mm)
T = period of wobbler in sec.

To fully exploit the maximum beam current I_B = 392 µA the values i_0 and a^2 are related as

$$\frac{a^2}{i_m} = \frac{\pi}{I_B} \qquad (23)$$

and

$$\frac{a^2}{i_0} = 0{,}0080(\mu A^{-1})$$

The output is the current density distribution (i(r) (μA.mm^{-2})) as a function of of the wobbler radius (mm), the total beam and target current (μA) and the beam efficiency ε_B (%) i.e. the percentage of the total beam current sticking the target.

For each set (i_0, a^2), a wobbler radius $R_{W,m}$ for witch the maximum allowed current density (5 μA.mm^{-2}) is not exceded, is obtained, together with the associated values for I_T, T_C and ε_B.

By plotting I_T, I_T/I_C, R_W and $(I_T/I_C)_{RW=0}$ (i.e. the ratio of target over collimator current for R_W = 0) as a function of $i_0(a^2)$, the optimum conditions can be obtained.

In Table 2 the values of R_w, i_m, I_T, I_B, ε_B and $(I_T/I_C)_{RW=0}$ are summerized for i_0 = 10, 15, 20, 25, 30, 35 and 40 μA.mm^{-2}.

Table 2.

Optimization of accelerator parameters IBA-KARADJ-Tl-Targets
as a function of maximum current density collimator output (i_M)
Circular Wobbling applied

i_M	a^2	R_W	i_m	I_T	I_C	I_B	ε_B	I_T/I_C
(μA.mm^{-2})	(mm^{-2})	(mm)	(μA.mm^{-2})	(μA)	(μA)	(μA)	(%)	
10	0,080	2,94	5	277	115	392	70,66	2,408
10	0,080	000	10	339	53	392	86,47	6,396
15	0,120	3,04	5	295	97	392	75,25	3,041
15	0,120	000	15	372	20	392	94,89	18,60
20	0,160	3,16	5	310	82	392	79,1	3,780
20	0,160	000	20	385	7	392	89,1	55,00
25	0,200	3,37	5	313	79	392	79,8	3,952
25	0,200	000	25	389	3	392	99,3	129,6
30	0,240	3,61	5	307	85	392	78,3	3,612
30	0,240	000	30	391	1	392	99,7	391,0
35	0,280	3,85	5	297	95	392	75,8	3.126
35	0,280	000	35	392	0,39	392	99,9	1005
40	0,320	4,08	5	283	109	392	72,2	2,596
40	0,320	000	40	392	<<0,39	392	>99,9	>>1005

1. I(r) = $i_M.e^{-a^2.r}$ [$0 \le r \le 5$ mm; a^2 = gaussian exponent] gaussian current density distribution

2. Three parameter equation $\frac{a^2}{i_m} = \frac{\pi}{I_B}$

I_B = maximum beam current $= 392\,\mathrm{mA} = \int_0^{\infty} 2.\mathrm{i}_{\mathrm{M}}.e^{-a^2.r^2}.\pi.r.dr$

$a^2 = 0{,}0080\ i_M$

3. R_W = radius of the wobbler circle in mm
4. i_m = (maximum current density * 10) tolerated by 2 mm Cu-backing target = 5 µA.mm^{-2}
5. I_T, I_C target and collimator currents in µA for R_W ;
   $(I_T/I_C)_{RW=0}$ ratio for no wobbling i.e. $R_W = 0$
6. $\varepsilon_B = (I_T/I_C) * 100$ = beam current efficiency

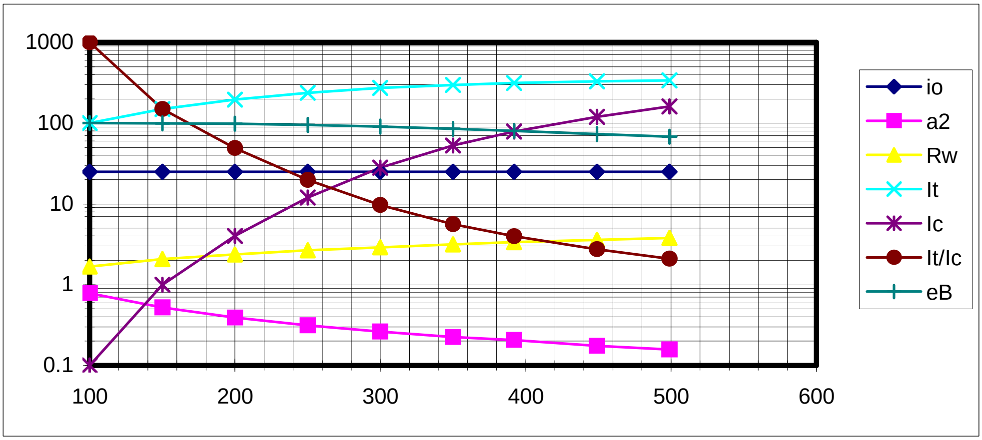

Fig. 3 Optimization of accelerator parameters IBA-KARADJ-Tl-Taregets as a function of maximum current density collimator output (i_M)Circular Wobbling applied

Fig. 3 represents the graphic plot of this data. From this figure it follows that the maximum target current is obtained for the following conditions:i_0 = 25µA.mm^{-2}; a^2 = 0,200 mm^{-2};
R_W = 3,37 mm.
Resulting in :

$$I_T = 313\mu A$$

$$I_B = 392\mu A$$

$$\frac{I_T}{I_C} = 3,96$$

$$(\frac{I_T}{I_C})_{R_W=0} = 129,6$$

$$\varepsilon_B = 79,8\%$$

Fig.9 shows i(r) = $25.e^{-0{,}200.r^2}$ for different values of the wobbler circle radius. The optimum radius (R_W = 3,37 mm) is the one for which the maximum value i(r), is equal to the maximum alloable current density (5μA.mm^{-2}).

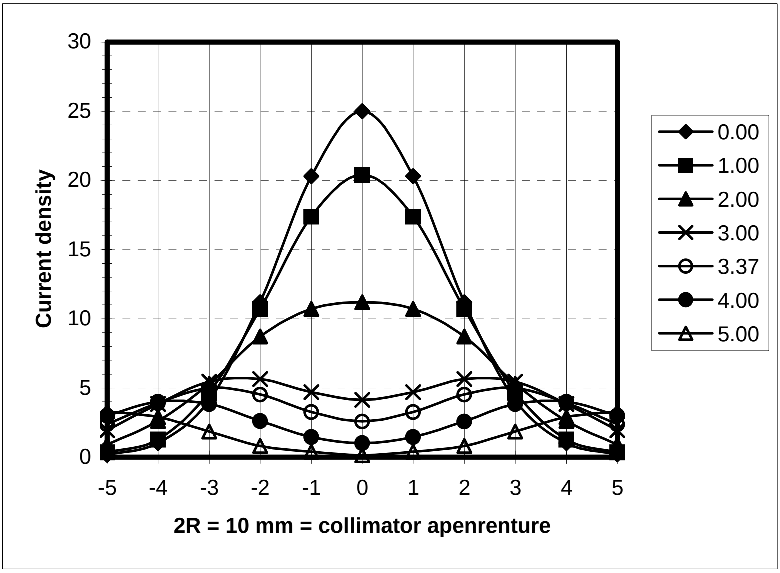

Fig. 4 Current density distribution i(r) = $25.e^{-0{,}200.r^2}$

Fig. 4 shows the current density distribution on target. This figure is obtained by 6° projection of the optimum current density distribution curve.

To adjust the beam transport parameters such that the maximum target current is obtained, the operator should use two target carriers : one contains a Cu-backing only, the second holds the Tl/Cu target.

1. With the Cu-carrier only and without application of wobbling, the operator should adjust the beam transport parameters such that

$$I_B = 392\mu A$$

$$\frac{I_T}{I_C} = 129{,}6$$

2. Next wobbling should be started and the excentricity (R_W = 3,37 mm) should be adjusted so that

$$\frac{I_T}{I_C} = 3{,}96$$

where after the current should be cut-off by the Faradaycup.
3. The Cu-carrier should be removed and the Tl/Cu target placed in position
This study was applied in the cyclotron project [2-5].

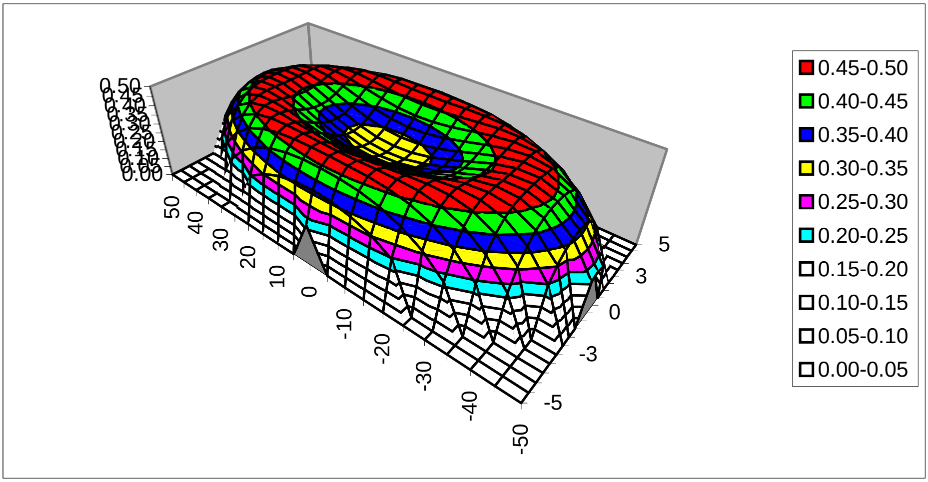

Fig. 5. The 3D representation of the current density

REFERENCES

1. P. Van den Winkel, L. Daraban, Studia univ B-B,ser.Physica -early paper (p.19-) 2006

2. S.M. Quaim, R. Weinreich, H. Ollig, *Production of ^{201}Tl and ^{203}Pb via proton induced nuclear reactions on natural thalium*, Int.J.Appl.Radiat.Isot., **30**, 85-97(1979)

3. I. E. Teodorescu, Generatoare de neutroni, Ed. Acad.RSR, p.161, Bucuresti (1969)

4. A. Sattari, N. Shadanpour, K. Kamali Moghadam, G. Aslani, *A fast way of determination of ^{202}Tl impurity in ^{201}Tl, 5 ICI Conference on Isotopes*, Brussels, Belgium, 25-29 april, Proc. Conference, pp.27-32 (2005).

5. G. Raisali, N. Hajilo, S. Haimidi, G. Aslani, *Energy spectrum and dose distribution of neutrons and gamma rays in the labyrinth through the NRCAM Cyclone 30 shield*, *5 ICI Conference on Isotopes*, Brussels, Belgium, 25-29 april, Abstract Conference, p.47(2005).

STUDIA UNIVERSITATIS BABEŞ-BOLYAI, PHYSICA, L, 2, 2005

PRELIMINARY STUDIES ON THE PLASMA NEEDLE

SORIN DAN ANGHEL[1], ALPÁR SIMON AND ELŐD HAINAL-FILLA

ABSTRACT. This paper presents the preliminary results obtained for the plasma needle. It has been generated at atmospheric pressure in He, by means of radio-frequency excitation, using a very simple configuration: the sharpened central conductor of a 50 Ω coaxial cable. The plasma has been characterized from both electrical and thermal point of views. It could be operated at various He gas flow-rates (0.25 – 2.5 l/min) with RF absorbed power levels below 1 W, having a temperature in the range of 50 – 110 °C.

1. Introduction

A cold plasma at atmospheric pressure could be obtained using the same experimental conditions as for the hotter plasmas ($T_{gas} \sim 10^2 - 10^3$ K) but some very important aspects have to be kept in sight: a) the plasma gas flow-rate has to be reduced; b) smaller operating voltages has to be used; c) the plasma volume has to be reduced. The interest about non-thermal atmospheric pressure plasmas are in continuous increasing all in the worldwide for theirs tremendous applications in medicine, biology, technology and many others. The most important applications to mention are: sterilization [1], high precision cellular removal [2] (in surgery), plasma display panels, and plasma surface treatments. Plasmas are ionized gases, but the very high temperatures would immediately kill living cells. The “plasma needle” represents atmospheric pressure non-thermal plasma around a sharp metallic electrode and it is obtained usually in He gas flow. Its main characteristic is that it is non destructive for living cells, it is obtained at room temperature and has a small penetration depth [3]. Also these atmospheric pressure cold plasmas represent sources of charged particles, UV radiation (in the range of 300-400 nm) and active oxygen radicals (O^*, OH^*). These particles can interact with the bacteria; by breaking the cellular wall (see reference [1] for the Gram-positive and Gram-Negative bacteria study). In this way this can be a perfect, nondestructive method for the sterilization of sensitive medical instruments, too. With the “plasma needle” one can obtain the stable glow discharge with RF frequencies around 13.56 MHz with the He gas flow around 1 l/min, of course it will work with Ar, N_2, He and air mixtures. To make the needle usable in other domains one

---

[1] "Babeş-Bolyai" University, Faculty of Physics, M. Kogalniceanu 1, 400084 Cluj, Romania
E-mail: anghels@phys.ubbcluj.ro; asimon@phys.ubbcluj.ro

must study its characteristics, behavior in different operating conditions, must create a theoretical model to understand all the phenomena in the discharge.

This paper is dealing with the preliminary analysis of the plasma needle. There are presented some experimental results about our first laboratory prototype, with the intention to describe its behavior and properties in different operating conditions.

2. Experimental

The plasma needle was generated using an RF oscillator described elsewhere [4]. As compared to the experimental set-up used by other authors to generate the plasma needle, we have exploited the possibility of obtaining various RF voltages from the resonant circuit of the free running type RF oscillator. The maximum RF power could be achieved easily by adjusting the coupling factor between the oscillating circuit's coil and the reaction coil. The needle is presented in Fig 1.

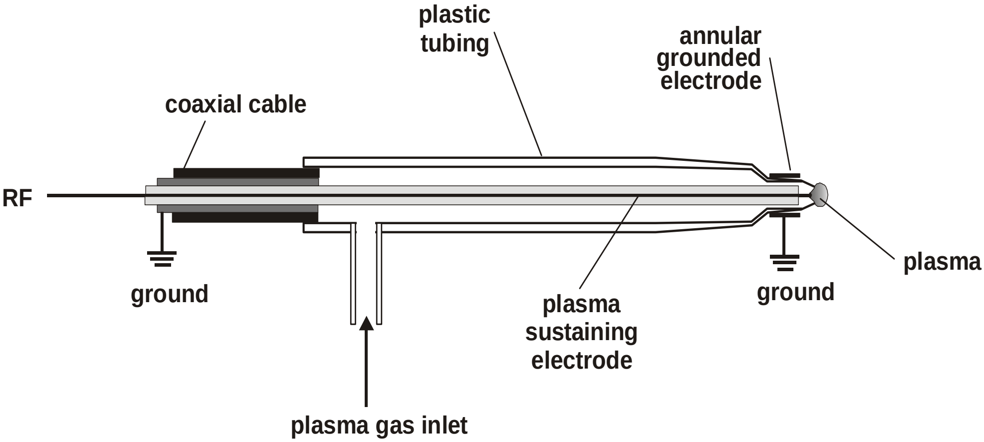

Fig. 1. The plasma needle configuration

The RF power is transmitted from the generator towards the needle via coaxial cable (50 Ohm). A 410 mm long coaxial cable with BNC connector was attached on the free end of the coil L_2 in the resonant circuit of the oscillator. On the free end of the cable the external insulation was removed on a length of 65 mm along with the shielding. The central insulation was removed on a length of 1 mm and the central copper conductor was sharpened. The whole system was placed inside of plastic tubing as shown in Fig.1. The dimensions of this device are: 67 mm length, 9 mm o.d., 7 mm i.d. and the exit nozzle with 5 mm o.d. and 3 mm i.d, respectively. The gas inlet is perpendicular on the body of the device and it has a 6 mm o.d. and 4 mm i.d., respectively.

The voltage of the sharp tip was measured using a laboratory made voltage probe [5]. The voltage probe is an L shaped copper wire antenna (40 mm the long arm, 10 mm the short arm) placed parallel to the plasma-sustaining electrode at a distance of 3.5 mm from the plasma electrode, as shown in Fig.2. The induced voltage in antenna is proportional to the voltage of the tip of the plasma electrode. The proportionality factor was determined by detaching the ensemble of the plasma torch and antenna, applying of a known voltage at a frequency of 7 MHz on the plasma-sustaining electrode and measuring the induced voltage into antenna, via a TDS 220 oscilloscope (Tektronix). The proportionality factor between the electrode voltage and the antenna voltage was found to be 62.72 (see the plot shown in Fig 2). We suppose that this factor is the same over a larger range of RF voltages applied to the plasma-sustaining electrode. The temperature was measured with a K type thermocouple using a MAS 345 type MASTECH auto-range, dual display digital multimeter (see Fig.2). The presence of the thermocouple does not perturb the discharge if its presence does not induce the formation of electric arcs.

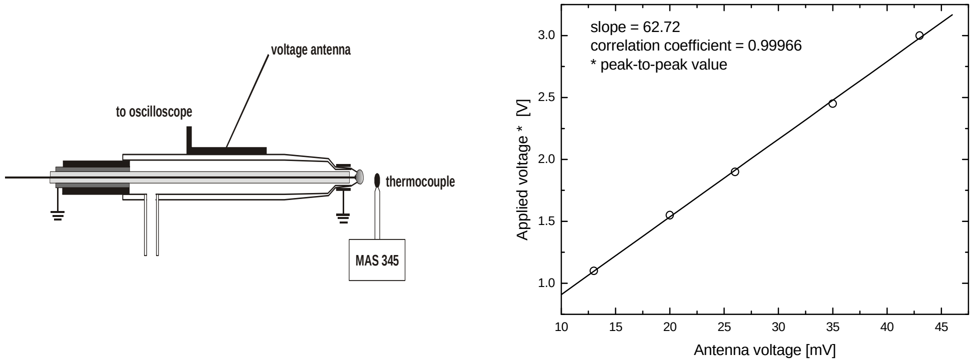

Fig. 2. The voltage probe and its calibration plot. The experimental set-up for temperature measurements.

3. Results and Discussions

The influence of the DC voltage supplying the RF oscillator on the absorbed RF power is presented in Fig.3 and as it was expected, the power increases when the supply voltage is increased.

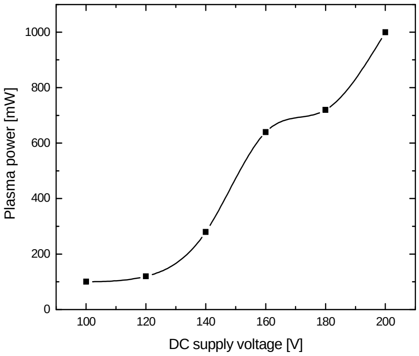

Fig. 3. Absorbed plasma power as function of DC supply voltage

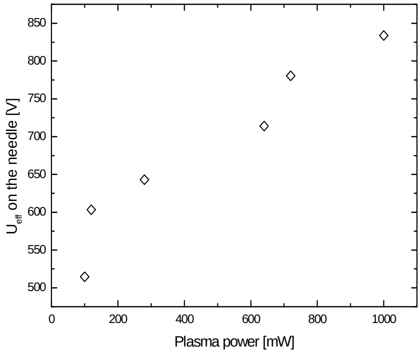

Fig. 4. Effective voltage on the needle as function of absorbed RF plasma power

At lower voltages (below 120 V) the change in the absorbed power is small. At higher voltage values there is an almost linear increase for the absorbed power as function of DC supply voltage. These facts could be easily explained: at lower DC supply voltages (smaller plasma power levels) the voltage of the needle is smaller and the plasma has a lower ionization degree and the electron-neutral collision frequency is smaller, too. At higher DC supply voltages (when more power is absorbed) the plasma has a higher ionization degree. The relationship between the plasma power and the effective voltage of the needle is presented in Fig.4.

The plasma has various shapes as function of gas flow rate and RF power from a luminous point (100 mW) to a well formed “ball” (200 mW and 1 l/min He) or almost jet like longed shape (high flow-rates, up to 7-10 l/min). The color of the plasma is also changed at higher He flow-rates, from light blue to a white-green-blue mixture (Fig.5).

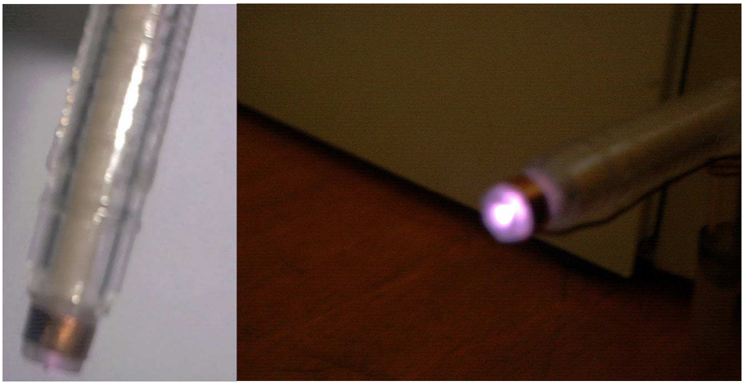

Fig. 5. The working plasma needle

The needle voltage and the plasma behavior are influenced by the supply voltage. At a He flow-rate of 1 l/min, the gas breakdown occurs for a DC supply voltage of 90 V (497 V effective voltage of the needle). At this value the plasma has a point like shape on the tip of the central electrode. The further increase in the DC supply voltage will induce a linear increase in the needle voltage and a well-defined ball like discharge will be formed on the tip. At higher voltages a luminous shield will surround the electrode. Lowering the supply voltage, the plasma shutdown will appear at 70 V (435 V effective voltage of the needle). Breakdown and shutdown voltages as function of He flow-rate are shown in Fig.6.

The temperature as function of the axial distance between the thermocouple and the needle for the lowest and highest power level is shown in Fig.7.

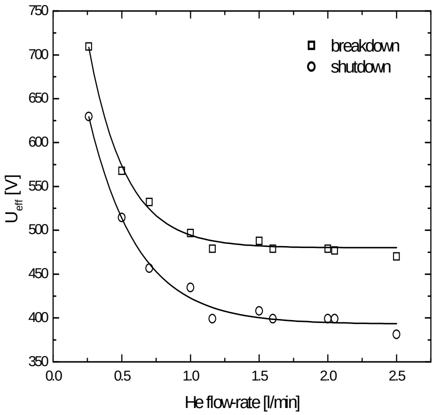

Fig. 6. Breakdown and shutdown voltages as function of He flow-rate

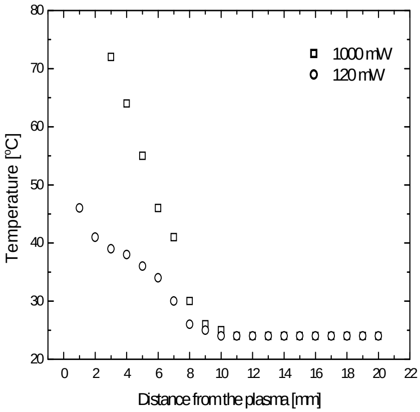

Fig. 7. Temperature determined via thermocouple as function of distance to the tip

For distances higher than 8 mm there is no significant change in the ambient temperature. Between 8 and 1 mm from the tip the temperature exhibits a linear increase. Below 1 mm between the needle and the thermocouple the plasma is perturbed due to the tendency of the discharge to become and electric arc. Therefore, the indications of the temperature measurement system in this situation are not correct. For the other power levels the dependency has a similar shape. Analyzing these dependences one can say that the thermal effect of the needle is directly related to the plasma power and detectable at distances closer than 10 mm from the needle tip.

The preliminary results presented in this paper obtained on an atmospheric pressure, capacitively coupled He plasma needle serves as an introductory study towards further extensive research conducted in our laboratory regarding electrical modeling, optical and biological characterization and biomedical applications, respectively.

REFERENCES

1. M. Laroussi, I. Alexeff, J.P. Richardson and F.F. Dier, *IEEE Trans. Plasma Sci.* **30,** 158 (2002)
2. E. Stoffels, A.J. Flikweert, W.W. Stoffels and G.M.W. Kroesen, *Plasma Sources Sci. Technol.* **11**, 383 – 388 (2002)
3. E. Stoffels, *High Temp. Material Processes* **6**, 191 (2002)
4. S.D. Anghel, *IEEE Trans. Plasma Sci.* **30**, 660 (2002)
5. S.D. Anghel, A. Simon and T. Frentiu, *J. Anal. At. Spectrom.* **-** in press (2005), www link: http://www.rsc.org/publishing/journals/JA/article.asp?doi = B502818C

STUDIA UNIVERSITATIS BABEŞ-BOLYAI, PHYSICA, L, 2, 2005

ZERO SOUND IN TWO DIMENSIONS

I. GROSU[1], O. BUNĂU

ABSTRACT.Using a simple repulsive contact interaction model we calculated the dispersion relation for the zero sound mode in two dimensional interacting Fermi systems. The almost linear dispersion relation reduces to the linear form in the long-wave limit. The damping of the mode appears at a critical wavevector which was calculated.

Zero sound mode is a collective mode that occurs in a neutral Fermi system at zero temperature. A repulsive contact interaction (short-range interaction,$V(r)\propto\delta$ (r)) is sufficient to produce such a mode [1,2]. The zero sound mode represents an oscillation of the Fermi surface with a velocity larger than Fermi velocity v_F , and with a linear dispersion relation. Landau analyzed this collective mode, and in three dimensions the dispersion relation is given by Landau equation [3]:

$$\frac{\omega}{qv_F}\ln\left|\frac{\omega+qv_F}{\omega-qv_F}\right|=2+\frac{2}{N(0)V} \tag{1}$$

as long as the collective mode in well defined ($\omega>\omega^0_{pq}$, with $\omega^0_{pq}=\frac{p_Fq}{m}+\frac{q^2}{2m}$). Here $N(0)$ is the electron density of states, V the strength of the fermion-fermion interaction, p_F the Fermi momentum, and q the wavevector. In the weak-coupling limit ($N(0)V << 1$), Eq. (1) possesses the solution:

$$\omega=qv_F\left[1+\frac{2}{e^2}\exp\left(-\frac{2}{N(0)V}\right)\right] \tag{2}$$

The damping of the zero sound mode occurs at a critical wavevector q_c that is given by the condition when the collective mode spectrum overlaps the electron-hole excitation spectrum:

$$q_c=\frac{4}{e^2}p_F\exp\left(-\frac{2}{N(0)V}\right) \tag{3}$$

Here we will reconsider the problem of the zero sound mode in two dimensional interacting Fermi systems, using the equation of motion method for an electron-hole pair $c^+_{\vec{p}+\vec{q},\sigma}c_{\vec{p},\sigma}$, and the Random Phase Approximation

---

[1] Department of Theoretical Physics, University of Cluj, 3400 Cluj, Romania

(RPA). In this approximation, and in the absence of damping, the dispersion relation is given by:

$$1=2V(q)\int\frac{d^2p}{(2\pi)^2}\left(\frac{1}{\omega-\frac{pq}{m}\cos\theta-\frac{q^2}{2m}}-\frac{1}{\omega+\frac{pq}{m}\cos\theta+\frac{q^2}{2m}}\right)\equiv 2V(q)(I_1-I_2) \quad (4)$$

V(q) is the Fourier transform of the contact interaction. The integrals from Eq.(4) will be calculated in a similar way of Stern [4], and Ando et al.[5], concerning the properties of two dimensional systems:

$$I_1=\frac{1}{(2\pi)^2}\int_0^{p_F}dpp\int_0^{2\pi}\frac{d\theta}{(\omega-\frac{q^2}{2m})-\frac{pq}{m}\cos\theta}\equiv\frac{1}{(2\pi)^2}\int_0^{p_F}dppI_1' \quad (5)$$

We will consider the case when $\omega>\frac{q^2}{2m}$. For the angular integral we use:

$$\int_0^{2\pi}\frac{d\theta}{a+b\cos\theta}=\begin{cases}\frac{2\pi}{\sqrt{a^2-b^2}}; & a>|b|\\ 0 \quad ; & |a|<|b|\end{cases} \quad (6)$$

with:

$$a=\omega-\frac{q^2}{2m} \qquad b=-\frac{pq}{m} \quad (7)$$

From the condition $a>|b|$ it follows that:

$$p<p_0\equiv\frac{m\omega}{q}-\frac{q}{2} \quad (8)$$

and:

$$I_1'=\begin{cases}\frac{2\pi}{\sqrt{\left(\omega-\frac{q^2}{2m}\right)^2-\left(\frac{pq}{m}\right)^2}}; & p<p_0\\ 0 \quad ; & p>p_0\end{cases} \quad (9)$$

For the integral I_1 we have two distinct cases:

- For: $p_0<p_F$:

$$I_1=\frac{1}{(2\pi)^2}\left[\int_0^{p_0}dppI_1'+\int_{p_0}^{p_F}dppI_1'\right]=\frac{1}{(2\pi)^2}\int_0^{p_0}dppI_1' \quad (10)$$

when:

$$I_1=\frac{m}{2\pi}\left(\frac{m\omega}{q^2}-\frac{1}{2}\right) \qquad p_0<p_F \quad (11)$$

- For: $p_0>p_F$:

$$I_1 = \frac{1}{(2\pi)^2}\int_0^{p_F} dp\,p I_1' = \frac{1}{(2\pi)^2}\int_0^{p_F} dp\,p \frac{2\pi}{\sqrt{(\omega - \frac{q^2}{2m})^2 - (\frac{q}{m})^2 p^2}} \tag{12}$$

and:

$$I_1 = \frac{m}{2\pi}\left(\frac{m\omega}{q^2} - \frac{1}{2}\right)\left[1 - \sqrt{1 - \left[\frac{p_F}{q\left(\frac{m\omega}{q^2} - \frac{1}{2}\right)}\right]^2}\,\right] \qquad p_0 > p_F \tag{13}$$

Collecting the results (11) and (13), one can write:

$$I_1 = \begin{cases} \frac{m}{2\pi}\left(\frac{m\omega}{q^2} - \frac{1}{2}\right) & ; q > q_1 \\ \frac{m}{2\pi}\left(\frac{m\omega}{q^2} - \frac{1}{2}\right)\left[1 - \sqrt{1 - \left[\frac{p_F}{q\left(\frac{m\omega}{q^2} - \frac{1}{2}\right)}\right]^2}\,\right] & ; 0<q<q_1 \end{cases} \tag{14}$$

Here:

$$q_1 = p_F\left(-1 + \sqrt{1 + \frac{2m\omega}{p_F^2}}\right) \tag{15}$$

In a similar way, one obtains:

$$I_2 = \begin{cases} \frac{m}{2\pi}\left(\frac{m\omega}{q^2} + \frac{1}{2}\right) & ; q_2 < q < q_3 \\ \frac{m}{2\pi}\left(\frac{m\omega}{q^2} + \frac{1}{2}\right)\left[1 - \sqrt{1 - \left[\frac{p_F}{q\left(\frac{m\omega}{q^2} + \frac{1}{2}\right)}\right]^2}\,\right] & ; 0 < q < q_2, \quad q > q_2 \end{cases} \tag{16}$$

with:

$$q_2 = p_F\left(1 - \sqrt{1 - \frac{2m\omega}{p_F^2}}\right) \tag{17}$$

$$q_3 = p_F\left(1 + \sqrt{1 - \frac{2m\omega}{p_F^2}}\right) \tag{18}$$

and with the condition:

$$0<\frac{2m\omega}{p_F^2}<1 \tag{19}$$

and: $0<q_1<q_2<q_3$.

In the case when no damping is present, we have the additional condition:

$$\omega>\omega_{pq}^0\equiv\frac{p_F q}{m}+\frac{q^2}{2m} \tag{20}$$

which is equivalent with:

$$0<q<q_1 \tag{21}$$

Intersecting this condition with (14) and (16), we get ($0<q<q_1$):

$$I_1=\frac{m}{2\pi}\left(\frac{m\omega}{q^2}-\frac{1}{2}\right)\left[1-\sqrt{1-\left[\frac{p_F}{q\left(\frac{m\omega}{q^2}-\frac{1}{2}\right)}\right]^2}\right] \tag{22}$$

$$I_2=\frac{m}{2\pi}\left(\frac{m\omega}{q^2}+\frac{1}{2}\right)\left[1-\sqrt{1-\left[\frac{p_F}{q\left(\frac{m\omega}{q^2}+\frac{1}{2}\right)}\right]^2}\right] \tag{23}$$

Using the density of states in two dimensions:

$$N(0)=\frac{m}{2\pi} \tag{24}$$

and taking the Fourier transform of the contact interaction:

$$V(q)=\frac{V}{2} \tag{25}$$

the dispersion relation, obtained from Eq.(4), is:

$$\omega=qv_F\sqrt{1+\frac{N(0)V}{2}\frac{1}{1+\frac{1}{2N(0)V}}+\left(\frac{q}{2p_F}\right)^2\left(1+\frac{1}{N(0)V}\right)^2} \tag{26}$$

with the condition (from Eq.(20)):

$$\omega>qv_F\left(1+\frac{q}{2p_F}\right) \tag{27}$$

In the long-wave limit ($q\to 0$, $q/2p_F<<1$), Eq.(26) becomes:

$$\omega \cong q v_F \sqrt{1 + \frac{N(0)V}{2} \frac{1}{1 + \frac{1}{2N(0)V}}} \qquad (28)$$

In the weak-coupling limit (consistent with RPA), $N(0)V << 1$, and Eq.(28) reduces to:

$$\omega \cong q v_F \left[1 + \frac{1}{2} (N(0)V)^2 \right] \qquad (29)$$

The almost linear dispersion relation (26) becomes linear in the long-wave limit, and the velocity is larger than Fermi velocity v_F. Using Eq.(29), the critical wavevector in two dimensions becomes:

$$q_c = p_F [N(0)V]^2 \qquad (30)$$

In the strong-coupling limit, the dispersion relation is given by:

$$\omega \cong q v_F \sqrt{\frac{N(0)V}{2}} \qquad (31)$$

a result with a similar form to the relation in three dimensions [1].

Conclusions

In conclusion, we calculated, using a simple model, the dispersion relation for the zero sound mode in two dimensions. Such a mode can occur in interacting Fermi systems (e.g. ^3He thin layers). However, the ^3He case seems to be much more complicated, and has to be carefully analyzed [6]. Additionally, strong interacting systems (e.g. high-temperature superconductors) have a non-Fermi character (even in two dimensions) [7], and require a separate treatment.

REFERENCES

1. A.L.Fetter, J.D.Walecka, "Quantum theory of many-particle systems", McGraw-Hill, (1971)
2. D.Pines, P.Nozieres, "The theory of quantum liquids", vol.I, Benjamin, New York, (1966)
3. L.D.Landau, Sov.Phys.JETP 3, 920, (1956); 5, 101, (1957)
4. F.Stern, Phys.Rev.Lett.18, 546, (1967)

5. T.Ando, A.B.Fowler, F.Stern, Rev.Mod.Phys.54, 437, (1982)
6. D.Vollhardt, Rev.Mod.Phys.56, 99, (1984)
7. P.W.Anderson, "The theory of superconductivity in the high-T_c cuprates", Princeton University Press, New Jersey, (1997)

STUDIA UNIVERSITATIS BABEŞ-BOLYAI, PHYSICA, L, 2, 2005

THE SPECIES ABUNDANCES DISTRIBUTION IN A NEUTRAL COMMUNITY MODEL

ZOLTÁN NÉDA*,1, MÁRIA RAVASZ1, ADALBERT BALOG2 AND ARANKA DERZSI1

ABSTRACT. Analytical approximations and computer simulations are considered for determining the Species Abundances Distribution in neutral community ecological model. The neutral community model considered by us has many common features with the generally accepted model introduced by S. Hubbell [1]. The analytically obtained distribution function describes well the computer simulation results and real measurement data on large-scale neutral type ecological systems. Our solution leads also to an interesting relation between the total number of individuals, total number of species and the size of the most abundant species in the considered metacommunity. Computer simulations on the considered model prove also the validity of this scaling relation.

I. Introduction

Communities of ecologically similar species that compete with each other solely for resources are often described by neutral community models (NCM) [1-4]. These models proved to be successful and useful in describing many of the basic patterns of biodiversity such as the distribution of abundance, distribution of range, the range-abundance relation and the species-area relation [2,3]. The neutral theory is considered by many ecologists as a radical shift from established niche theories and generated considerable controversy [5-9]. The relevance of NCM for describing the dynamics and statistics of real communities is still much debated and criticized [10].

Nowadays NCM are studied both by Monte Carlo type computer simulations [3,2,11], and analytic approximations [12-14]. One of the key issues that macro-ecologist are often investigating is the species abundances distribution (SAD), introduced for characterizing the frequency of species with a given abundance [15-17]. In the case of the most generally accepted neutral model defined by Hubbell [1] the shape of the SAD is called Zero Sum Multinomial (ZSM) distribution [11,18]. Recently, an exact solution was given for the analytical form of ZSM [13].

The aim of the present paper is to define a novel version of the neutral community models and to give an analytical mean-field type approximation for

---

[1] Babeş-Bolyai University, Department of Theoretical Physics str. Kogălniceanu 1, RO-400084 Cluj-Napoca, Romania

[2] EMTE-Sapientia University, Department of Engeneering, RO-4300, Tirgu-Mureş, Romania

[*] E-mail: zneda@phys.ubbcluj.ro

the SAD generated by this model. By using the invariance of the system against the intrinsic fluctuations characteristic for NCM, we derive an analytic solution that describes well the results of computer simulations on this model. The derived analytical form of SAD leads also to an interesting relation between the total number of individuals, total number of species and the size of the most abundant species of the considered meta-community. This novel scaling relation is confirmed by computer simulations on neutral models. We also show, that the obtained shape of SAD describes well measurement results on real neutral type ecological systems.

II. Neutral Community Models

NCM are usually defined on lattice sites, on which a given number of $S_{\max}$ species can coexist [1,2,11] and compete for resources. Each lattice site can be occupied by many individuals belonging to different species, however the total number of individuals for each lattice site is limited to a fixed $N_{\max}$ value. This limiting value models the finite amount of available resources in a given territory. As time passes individuals in the system can give birth to individuals belonging to the same species, can die or can migrate to a nearby site. The neutrality of the model implies that all individuals (regardless of the species they belong to) are considered to be equally fit for the given ecosystem, and have thus the same b multiplication, d death and q diffusion rate. The system is considered also in contact with a reservoir, from where with a small $w << 1$ probability per unit time an individual from a randomly chosen species can be assigned to a randomly chosen lattice site. This effect models the random fluctuations that can happen in the abundances of species. The dynamics of the considered community is than as follows:

- A given number of individuals from randomly chosen species are assigned to randomly chosen lattice sites.
- With the initially fixed probabilities we allow each individual to give birth to another individual of the same species, to die or to migrate to a nearby site.
- We constantly verify the saturation condition at each site. Once the number of individuals on a site exceeds the $N_{\max}$ value, a randomly chosen individual is removed from that site.
- We apply the random fluctuations resulting from the reservoir.

After on each lattice site saturation is achieved, a dynamical equilibrium sets in, and one can study the statistical properties of several relevant quantities. Computer simulations usually focus on generating SAD and on studying several scaling relations like species-area and range-abundance relations.

The neutral community model defined by Hubbell [1] is characterized by a master equation written for SAD, where Hubbell defined some birth and death probabilities for each species with a given number of individuals. The model considered by us follows roughly all the above rules, the master equation written for SAD is the same as for the Hubbell model, the difference is only in the defined birth and death probabilities [13]. While in the version defined by Hubbell the total number of individuals in the considered system is exactly conserved, we will see that our model and analytic solutions allow a realistic fluctuation for this number. A second main difference relative to the model defined by Hubbell is that in Hubbell's model there is an extra mutation probability for each species, which is absent in our model.

III. Species Abundances Distribution in our version of the neutral community model

Let us consider a fixed area in a NCM (a delimited region in the lattice) on which we study SAD (Species Abundances Distribution). In the selected area we denote by $S(x,t)$ the number of species with size x at the time moment t (x is a discrete variable $x=1,2,...k...$). $S(x,t)$ divided by the total number of species yields the mathematically rigorously defined SAD. We mention here that in most of the papers dealing with SAD, instead of this rigorously defined distribution function a histogram on intervals increasing as a power of 2 is constructed [15-17]. On a log-normal scale this histogram usually has a Gaussian shape, and thus SAD is called a log-normal distribution. Without arguing on the relevance of this histogram (a nice treatment on this subject is given by May [16]) for the sake of mathematical simplicity we will not use this representation, and calculate instead the mathematically rigorous distribution function. It is of course anytime possible to re-plot the obtained distribution function in the form that is usually used by ecologists, using instead of the x variable the $z=\log_2(x)$ variable.

In the framework of the model considered by us the time evolution of $S(x,t)$ for a unit time $dt=1$ can be approximated by the master-equation:

$$\begin{aligned} S(x,t+1) = S(x,t) + [W_+(x-1)S(x-1,t) + W_-(x+1)S(x+1,t) - \\ - W_+(x)S(x,t) - W_-(x)S(x,t)] \end{aligned} \qquad (1)$$

This equation is the same as in all previous analytical studies [12-14].

In the above equation $W_+(x)$ denotes the probability that one species with size x increases its size to $x+1$ in unit time (birth probability) and $W_-(x)$ denotes the probability that one species with size x decreases its size to $x-1$ in unit time (death probability). We neglected here the possibility that in the chosen unit time-interval one species increases or decreases its size by more than one individual. It is also worth mentioning that this master equation is not applicable in the neighborhood of the limiting values of x since here either $x-1$ or $x+1$ do not exist. We expect thus that the shape of SAD determined from (1) can have problems for very low and very high values of x.

We assume now that SAD reaches a steady-state in time. All computer simulations on neutral models shows that this is true. This means that $S(x,t)$ should be time invariant concerning the fluctuations governed by equation (1). Under this stationarity assumption we get the equation:

$$W_+(x-1)S(x-1,t)+W_-(x+1)S(x+1,t)-W_+(x)S(x,t)-W_-(x)S(x,t)=0 \quad (2)$$

We have to approximate now the $W_+(x)$ and $W_-(x)$ probabilities. We will work with the assumptions of the NCM, and consider all species having the same birth, death and migration rate. Let us denote by P_+ the probability that one individual multiplies itself in unit time (we assume P_+ is the same for all individuals and species). Let us denote by P_- the probability that one individual disappears from the considered territory in unit time (again the same for all individuals and species). Further we assume that:

$$\begin{aligned} P_+ &<< 1 \\ P_- &<< 1 \end{aligned} \quad (3)$$

By simple probability theory we get:

$$W_+(x) = xP_+[1-(P_+ + P_-)]^{x-1} \quad (4)$$

The above equation tells us, that the increase by unity of the size of one species can be realized if any of the x individuals from a selected species multiplies itself, while the other individuals remain unchanged. (Of course, there are many other possibilities involving the birth and death of more than one individual. However, since we considered the (3) assumption all other possibilities will be orders of magnitude smaller). It is also worth mentioning that for the selected local community the effect of migration and the stochastic contribution from the reservoir can be taken into account through the birth and death processes, changing slightly the values of their probabilities. Migration inside the considered area is equivalent with a birth process, while migration outside from the considered territory is equivalent with death of individuals.

Using the assumptions (3) we can make now the following approximations:

$$W_+(x) = xP_+[1-(P_+ + P_-)]^{x-1} = xP_+[1-(P_+ + P_-)]^{[1/(P_+ + P_-)](P_+ + P_-)(x-1)} \approx \\ \approx xP_+ e^{-(P_+ + P_-)(x-1)} \tag{5}$$

In the same manner, one can write:

$$W_-(x) = xP_-[1-(P_+ + P_-)]^{x-1} \approx xP_- e^{-(P_+ + P_-)(x-1)} \tag{6}$$

The birth and death probabilities defined by equations (5) and (6) are different from those defined in the original model of Hubbell [1]. In this manner the model considered by us is also different from the model solved in [13]. As we already emphasized, the main difference is that in the neutral models considered up to now the total number of individuals in the system was exactly kept constant, and no realistic fluctuations of this quantity were allowed. In our model the mutation probability is also absent, in this manner our model is somehow oversimplified and an important fluctuation source is missing.

Now, instead of P_+ and P_- we introduce two new notations:

$$s = P_+ + P_- \tag{7}$$

$$q = P_+ - P_- \tag{8}$$

from where:

$$P_+ = \frac{s+q}{2} \tag{9}$$

$$P_- = \frac{s-q}{2} \tag{10}$$

From the assumptions (3) it is clear that it also holds:

$$s \ll 1 \tag{11}$$

$$q \ll 1 \tag{12}$$

Let us assume now that

$$|P_+| = |P_-| \rightarrow q = 0 \tag{13}$$

which would mean that the probability of multiplication and death is the same, so there is a constant number of individuals in the considered local community. In other words this means that the territory is saturated, and although the size of different species fluctuates, the total number N_t of population is constant.

The probability density for the species abundances distribution (SAD) is given than as:

$$\rho(x,t) = \frac{S(x,t)}{S_t} \tag{14}$$

Instead of x let us introduce now a new variable $y = x / N_t$ ($N_t >> 1$ is the total number of individuals in the system).

For $\rho(y,t)$ we have the (2) equation:

$$W_+(yN_t - 1)\rho(y - \frac{1}{N_t}, t) + W_-(yN_t + 1)\rho(y + \frac{1}{N_t}, t) - W_+(yN_t)\rho(y,t) \\ - W_-(yN_t)\rho(y,t) = 0 \tag{15}$$

Since $\rho(y,t)$ is a limiting distribution (not depending on t anymore), we will simply denote it as $\rho(y)$.

$$W_+(yN_t - 1)\rho(y - \frac{1}{N_t}) + W_-(yN_t + 1)\rho(y + \frac{1}{N_t}) - W_+(yN_t)\rho(y) - W_-(yN_t)\rho(y) = 0 \tag{16}$$

We can use now the Taylor series expansion to get $\rho(y - \frac{1}{N_t})$ and $\rho(y + \frac{1}{N_t})$:

$$\rho(y - \frac{1}{N_t}) = \rho(y) - \frac{1}{N_t}\rho^{'}(y) + \frac{1}{2N_t^2}\rho^{''}(y) \tag{17}$$

$$\rho(y+\frac{1}{N_t})=\rho(y)+\frac{1}{N_t}\rho'(y)+\frac{1}{2N_t^2}\rho''(y) \tag{18}$$

We denoted here by $\rho'(y)$ and $\rho''(y)$ the first and second order derivatives of the $\rho(y)$ function, respectively. Taking account of $q=0$, the values of $W_{\pm}(y)$ are given by (5, 6) as follows:

$$W_+(yN_t-1)=\frac{(yN_t-1)s}{2}\exp[-(yN_t-2)s] \tag{19}$$

$$W_-(yN_t+1)=\frac{(yN_t+1)s}{2}\exp[-yN_ts] \tag{20}$$

$$W_+(yN_t)=\frac{yN_ts}{2}\exp[-(yN_t-1)s] \tag{21}$$

$$W_-(yN_t)=\frac{yN_ts}{2}\exp[-(yN_t-1)s] \tag{22}$$

Inserting all these in equation (16):

$$\begin{aligned}&\frac{(yN_t-1)s}{2}\exp[-(yN_t-2)s][\rho(y)-\frac{1}{N_t}\rho'(y)+\frac{1}{2N_t^2}\rho''(y)]+\\&\frac{(yN_t+1)s}{2}\exp[-yN_ts][\rho(y)+\frac{1}{N_t}\rho'(y)+\frac{1}{2N_t^2}\rho''(y)]=\frac{yN_ts}{2}\exp[-(yN_t-1)s]\rho(y)\end{aligned} \tag{23}$$

Simplifying both sides with $s\cdot\exp[-yN_ts]$, some immediate algebra yields the following second order differential equation for $\rho(y)$:

$$\begin{aligned}&\rho(y)[\frac{yN_t}{2}(e^{2s}-2e^s+1)-\frac{1}{2}(e^{2s}-1)]+\rho'(y)\frac{1}{N_t}[\frac{yN_t}{2}(1-e^{2s})+\frac{1}{2}(1-e^{2s})]+\\&+\rho''(y)\frac{1}{2N_t^2}[\frac{yN_t}{2}(e^{2s}+1)+\frac{1}{2}(1-e^{2s})]=0\end{aligned} \tag{24}$$

Since $s << 1$ the following approximations are justified

$$e^{2s} \approx 1 + 2s \tag{25}$$

$$e^{s} \approx 1 + s \tag{26}$$

and the differential equation becomes:

$$-\rho(y)s + \rho^{'}(y)\frac{1}{N_t}[s + 1 - yN_t s] + \rho^{''}(y)\frac{1}{2N_t^2}[yN_t + yN_t s - s] = 0 \tag{27}$$

For solving this differential equation, in the **first approximation** we neglect all terms that are proportional with the $1/N_t \to 0$ quantity. This yields a first order differential equation:

$$s\rho(y) = -ys\rho^{'}(y) \tag{28}$$

This equation has the immediate solution

$$\rho_I(y) = C_1 / y \tag{29}$$

with C_1 an integration constant.

The histogram $\sigma(z)$ that is usually used for SAD can be immediately determined from (29), writing the $\rho_I(y)$ distribution as a function of the $z = \log_2(x) = \log_2(yN_t)$ variable. It is immediate to realize that this would yield a constant distribution ($\sigma_I(z) = C$).

A **better approximation** can be achieved by keeping the terms proportional with $1/N_t$ and neglecting the small $1/N_t^2$ and s/N_t terms. This yields the

$$-s\rho(y) + \rho^{'}(y)\frac{1}{N_t}[1 - yN_t s] + \rho^{''}(y)\frac{1}{2N_t}y = 0 \tag{30}$$

differential equation. Going back now to the $x = yN_t$ variable

$$-s\rho(x)+\rho'(x)[1-xs]+\rho''(x)\frac{x}{2}=0 \tag{31}$$

we get the general solution

$$\rho_{II}(x)=\frac{C_1}{x}+\frac{e^{2sx}C_2}{x} \tag{32}$$

where C_1 and C_2 are two integration constants.

By visually comparing with the experimental and simulated SAD curves, we can conclude that we need $C_1>0$ and $C_2<0$ to get the right shape. The general solution for SAD, should write thus

$$\rho_{II}(x)=\frac{K_1}{x}(K_2-e^{2sx}) \tag{33}$$

with K_1 and K_2 two real, positive constants.

It is immediate to observe that the obtained distribution for SAD, has a cutoff, i.e. there is a maximum value of x until $\rho(x)$ is acceptable (remains positive). This result is not surprising, since due to the finite number of individuals in the system and the finite value of the number of species one would naturally expect a cutoff in the distribution.

There are three fitting parameters in the mathematical expression of $\rho_{II}(x)$ (K_1, K_2 and s). Since $\rho_{II}(x)$ has to be normalized, we can determine K_1 as a function of K_2 and s. The normalization of this distribution function is not easy and cannot be done analytically, since there is no primitive function for $\exp(\alpha x)/x$.

However, if we can use the $sx<<1$ assumption and consider a Taylor expansion in the exponential we obtain the more simple distribution

$$\rho_{II}(x)\approx F_n\frac{F_1-x}{x} \tag{34}$$

(F_n and F_1 are again two positive real constants), which has a cutoff for $x=F_1$. This distribution function is exactly the same as the one proposed by Dewdney using totally different arguments [19], and named *logistic-J distribution*. As argued in [19] it describes well the SAD for many real communities.

The normalization condition for this distribution function is:

$$\int_1^{F_1} F_n \frac{F_1 - x}{x} dx = 1 \tag{35}$$

and immediately gives:

$$F_n = \frac{1}{F_1 \ln(F_1) - F_1 + 1} \tag{36}$$

The approximated normalized distribution function for SAD is then:

$$\rho_{II}(x) = \frac{1}{F_1 \ln(F_1) - F_1 + 1} \frac{F_1 - x}{x} \tag{37}$$

We can consider thus the above simple one-parameter fit to approximate the results for SAD on NCM.

The shape of $\sigma(z)$ can be again quickly obtained from $\rho_{II}(x)$, by changing the variable in this distribution function to $z = \log_2(x)$. A simple calculation yields the form

$$\sigma_{II}(z) = C(F_1 - 2^z) \tag{38}$$

where C is another normalization constant. It is important to realize, that $\sigma(z)$ given by the above approximation does not show the generally observed bell shaped curve, and for small values of z it is a constant. We must remember however that the shape of SAD given by our approximation can not be trusted for small z values, since in this limit the starting master equation (1) is not valid.

IV. SAD from computer simulations

In order to check the validity of our analytical approximation for SAD we performed computer simulations on the model presented in Section 2. We considered a lattice of size 20×20, $S_t = 400$ species, and $N_{\max} = 1000$ for each lattice site. We studied a local community on a square of 9×9 lattice sites, and we fixed several values for the dynamical parameters d/b and q/b. We used periodic boundary conditions, and the efficient kinetic or resident time Monte Carlo algorithm was implemented. The simulations were made on a $Pentium^{(TM)}4$ cluster. As a general result, we obtained that the analytical form given by (37) describes well the simulation data for SAD. In Figure 1 we present a characteristic fit for the simulation data. The parameters used in the simulation were $d/b = 0.3$ and $q/b = 0.2$. The obtained best fit parameter for equation (37) was $F_1 = 14500$. The rigorously defined $\rho(x)$ distribution function suggests that in NCM SAD has a scale-invariant nature. The finite size of the system introduces a natural cutoff in this scale-invariant behavior.

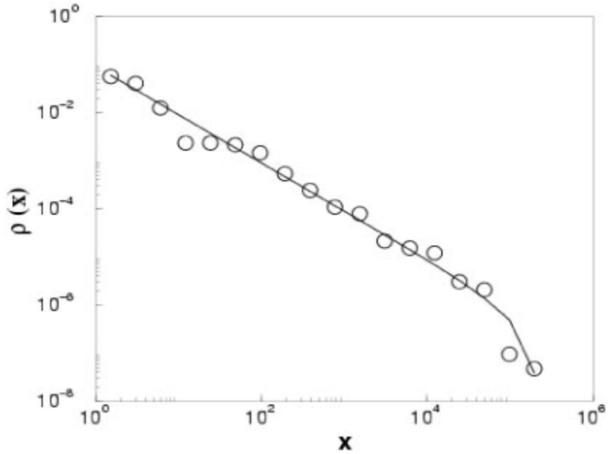

FIG. 1. *Characteristic fit (continuous line) with equation (37) for the simulation results (circles) on Species Abundances Distribution in Neutral Community Models. Simulations done on a* 20×20 *lattice,* $S_t = 400$, $N_{\max} = 1000$, $d/b = 0.3$ *and* $q/b = 0.2$. *The best fit parameter for SAD yield* $F_1 = 14500$.

Computer simulations on NCM prove thus the applicability of our analytical approximations for the form of the SAD.

V. Comparison with experimental results

We will fit now several large experimental datasets using the form (37) for SAD. To achieve this task, we re-plotted the publicly available results from the Barro Colorado Island (BCI) tree dataset [20,21], from the North American Breeding Bird Survey (BBS) database [22,23] and the light-trap measurements of Dirks [24], Seamans (unpublished data, results taken from [25]]) and Williams [26] on moths (Insecta: Lepidoptera). In the first graph of Figure 2 the BCI measurement results for SAD are re-plotted and fitted with the form (37). The measurements are for three different years and yield very similar data. All these data can be fitted acceptably by choosing the value of $F_1 = 13000$.

Similar results were obtained using the BBS data on the whole state of Alabama. Studying the survey for 1980 and 1990 one obtains again quite close data points, and the shape of SAD can be successfully approximated using $F_1 = 4100$ (second graph on Figure 2). The light-trap measurements on moths are plotted and fitted on the last graph of Figure 2. For the independent measurements made by Dirks and Seamans the best fit parameters are $F_1 = 1000$, and $F_1 = 4500$, respectively. Very similar results can be obtained re-plotting the results of Willimas [12], however this graph is not shown here since it would overcrowd the plot.

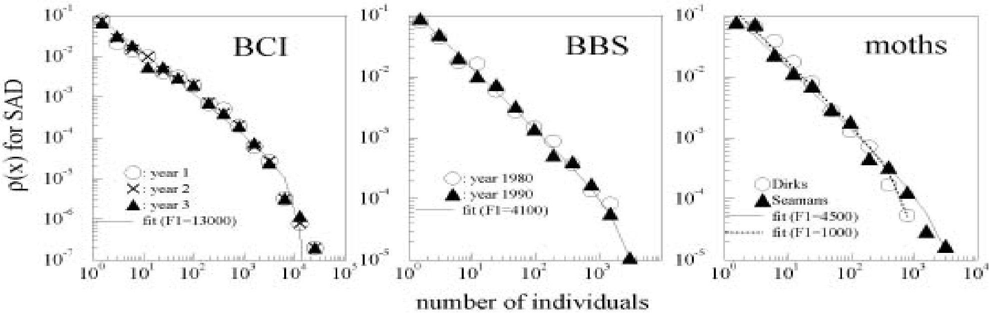

FIG. 2. *Experimental results on SAD fitted by the form (37). Results for the BCI dataset on three different years (best fit parameter* $F_1 = 13000$ *for all years), for the BBS dataset on the whole state of Alabama for 1980 and 1990 (best fit parameter* $F_1 = 4100$ *for both years) and for moths as measured by Dirks and Seamans (best fit parameter* $F_1 = 1000$ *and* $F_1 = 4500$*, respectively).*

As a conclusion, direct comparison with experimental results confirm that the form (37) describes reasonably well the species abundances distribution for many real meta-communities.

VI. Scaling laws resulting from SAD

Starting from the analytical approximation (37) for the form of SAD, we can derive an interesting relation between the size of the most abundant species (N_s), the total number of individuals (N_t) and the number of detected species (S_t) in the considered meta-community. The distribution function (37) has a cutoff at $x = F_1$, from where it results that $F_1 \approx N_s$. It is also immediate to realize that from the definition of $\rho(x)$ it results

$$N_t = \int_1^{N_s} Cx \frac{\rho(x)}{F_n} dx = C \int_1^{N_s} x \frac{N_s - x}{x} dx \tag{39}$$

$$S_t = \int_1^{N_s} C \frac{\rho(x)}{F_n} dx = C \int_1^{N_s} \frac{N_s - x}{x} dx \tag{40}$$

where C is a normalization constant, which normalizes $\rho(x)$ to the total number of species in the local community. The above two integrals are easily calculated and lead to the following two coupled differential equations:

$$N_t = CN_s(N_s - 1) - \frac{C}{2}(N_s^2 - 1) \tag{41}$$

$$S_t = CN_s \ln(N_s) - C(N_s - 1) \tag{42}$$

Working on relatively large habitats, one can use the $N_s >> 1$ assumption, and the coupled equation system from above can be simplified:

$$N_t \approx \frac{C}{2} N_s^2 \tag{43}$$

$$S_t \approx CN_s[\ln(N_s) - 1] \tag{44}$$

Eliminating from this system the normalization constant C we obtain the important relation:

$$\frac{S_t N_s}{N_t[\ln(N_s) - 1]} = 2 \tag{45}$$

Computer simulation results on NCM supports again the validity of the magic formula from above. (The simulations were made on a 20×20 lattice, and we choose $S_t = 400$, $N_{\max} = 1000$, $d/b = 0.3$ and $q/b = 0.2$). In Figure 3 we plotted the simulation results for different local community sizes, and the plot shows that equation (45) works well, however the constant on the right side of the equation seems to be slightly different from 2. We think that this slight difference is the result of our crude approximation: $F_1 \approx N_s$, and in reality we should have F_1 slightly bigger than N_s. The simulation data from Figure 2 was obtained after averaging over several local communities of size A.

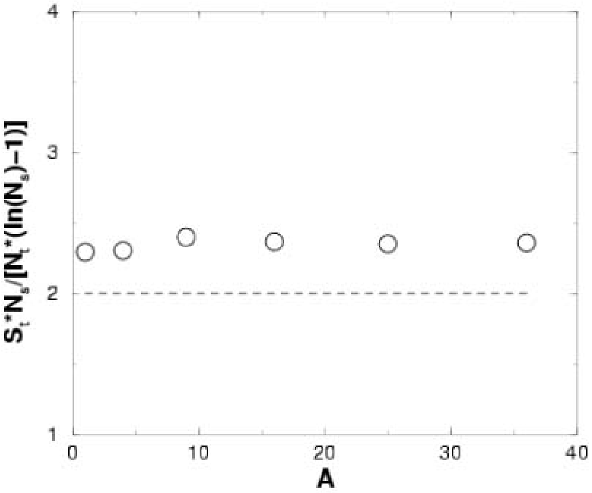

FIG. 3. *Validity of the (45) equation. Circles are simulation data and the dashed line indicates the expected value of 2. Parameters of the simulation are the same as in Figure 1.*

Increasing the size A of the considered habitat one would naturally expect $N_t \sim A$. Using equation (45) one would immediately get thus the interesting scaling-law:

$$\frac{S_t N_s}{\ln(N_s)-1} \sim A \qquad (46)$$

The (46) scaling relation can be also immediately verified in computer simulations on NCM. Results for a 20×20 lattice, $S_t = 400$, $N_{\max} = 1000$, $d/b = 0.3$ and $q/b = 0.2$ are shown on Figure 4. On the figure with a dashed line we indicated the power-law with exponent 1. As seen from the figure, the simulation data supports the scaling-law given by our analytical approach.

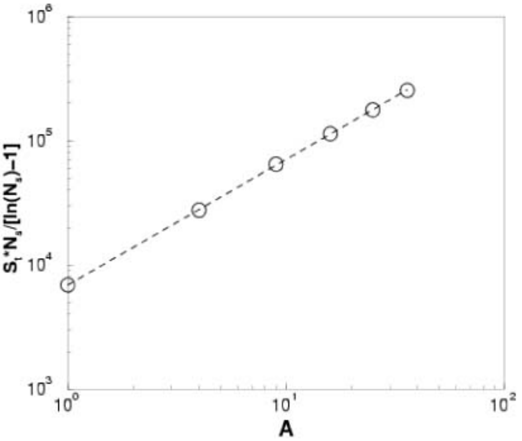

FIG. 4. *Validity of the (46) scaling law. Circles are simulation data and the dashed line indicates a power-law with exponent 1. Parameters of the simulation are the same as in Figure 1.*

VII. Conclusions

We have presented here a novel version of the neutral model introduced by Hubbell, and studied it for the species abundances distribution function both by computer simulations and a mean-field type analytical approximation. By using the invariance of this distribution regarding the internal fluctuations characteristic for the model, we derived an analytical approximation for the distribution function which describes well the simulation data obtained on the model. The obtained distribution suggest a power-law nature with exponent -1 in the limit of rare species and has a natural cutoff, governed by the finite extent of the system. Experimental results on several large databases show that the form of SAD obtained by us describes well the measurement data. Our results proved also the existence of an interesting relation between the total number of individuals, total number of species and the size of the most abundant species, found in the considered habitat. Computer simulations on the considered neutral model confirm the validity of this relation. Proving the existence of this connection in real experimental data is a challenge for further work in the field.

VIII. Acknowledgments

The present study was supported by the Sapientia KPI foundation for interdisciplinary research. We are grateful for Dr. N. Stollenwerk for helpful suggestions and discussions. We also thank Dr. V. Markó for introducing us in this fascinating interdisciplinary field, and for providing us a lot of interesting bibliography on the subject.

REFERENCES

1. S.P. Hubbell, *The Unified Neutral Theory of Biodiversity and Biogeography* (Princeton Univ. Press, Princeton, New Jersey, 2001)
2. G. Bell, Neutral Macroecology, *Science*, 293, 2413-2418 (2001)
3. J. Chave, Neutral theory and community ecology, *Ecology Letters*, 7, 241-253 (2004)
4. S. Norris, Neutral Theory: A New, Unified Model for Ecology, *BioScience*, 53, 124-129 (2003)
5. J.M. Levine, Species diversity and relative abundance in metacommunities, *Trends Ecol. Evol.* 17, 99-100 (2002)
6. B.J. Enquist, J. Sanderson and M.D. Weisser, Modeling macroscopic patterns in ecology, *Science* 295, 1835-1837 (2002)
7. P.A. Abrams, A world without competition, *Nature* 412, 858-859 (2001)
8. Clark, Macroecology comes of age, *Trends Ecol. Evol.* 17, 352-353 (2002)
9. J.Chave, H. C. Muller-Landau and S.A. Levine, *The American Naturalist* 159, 1-23 (2002)
10. S. Nee and G. Stone, *Trends Ecol. Evol.* 18, 433-434 (2003)
11. B.J. McGill, A test of the unified neutral theory of biodiversity, *Nature*, 442, 881-885 (2003)
12. B. Houchmandzadeh and M. Vallade, Clustering in neutral ecology, *Phys. Rev. E.* 68, 061912 (2003)
13. M. Vallade and B. Houchmandzadeh, Analytical solution of a neutral model of biodiversity, *Phys. Rev. E* 68, 061902 (2003)
14. Volkov, J.R. Banavar, S.P. Hubbell and A. Maritan, Neutral Theory and Relative Species Abundance in Ecology, *q-bio.PE/0504018* (2005)
15. F.W. Preston, The commonness and rarity of species, *Ecology* 29, 254-283 (1948)
16. R.M. May, Patterns of Species Abundance and Diversity, in *Ecology and Evolution of Communities* eds. M.L. Cody and J.M. Diamond (the Belknap Press of Harvard University Press, Cambridge, Massachusets and London, 1976)
17. E.C. Pielou, Mathematical Ecology, chapter 18 Species Abundances Relations (Wiley-Interscience, New-York 1977)
18. R. Condit et. al, Beta diversity in tropical forest trees, *Science*, 295 666-669 (2003)
19. A.K. Dewdney, A dynamical model of communities and a new Species-Abundance Distribution, *Biol. Bull.* 198 pp. 152-165 (2000)
20. R. Condit, S.P. Hubbell, and R.B. Foster, Changes in tree species abundance in a Neotropical forest: impact of climate change. *Journal of Tropical Ecology* 12 231-256 (1996)

21. R. Condit, Tropical Forest Census Plots (Springer-Verlag and R. G. Landes Company, Berlin, Germany, and Georgetown, Texas, 1998)

22. J. Price, S. Droege. and A. Price, The summer Atlas of North American Birds (Academic Press, San Diego, 1995)

23. C.S. Robbins, D. Bystrak and P.H. Geissler, The breeding Bird Survey: Its First Fifteen Years, 1965-1979 (US Department of Interior, Fish and Wildlife Service, Washington D.C, 1986)

24. C.O. Dirks, Biological studies of Maine moths by light trap methods. *The Maine Agriculture Experiment Station*, Bulletin no. 389, (Orono, Me, 1937)

25. F.W. Preston, The commonness and rarity of species, *Ecology* 29, 254-283 (1948)

26. R.A. Fisher, A.S. Corbet and C.B. Williams, The relation between the number of species and the number of individuals in a random sample of animal population *J. Anim. Ecol.* 12, 42-58 (1943)

STUDIA UNIVERSITATIS BABEŞ-BOLYAI, PHYSICA, L, 2, 2005

GAMMA AND BETA SPECTROMETRY STUDY ON NEUTRON ACTIVATED VITREOUS BIOACTIVE SYSTEMS CONTAINING YTTRIUM

D. CACAINA[1*], D. BARBOS[2], H. YLANEN[3], S. SIMON[1]

ABSTRACT. Radioactive and bioactive microspheres incorporating ^{90}Y radioisotope were investigated as a potential material for *in situ* radiotherapy of cancers. The glass samples obtained by melt annealing and sol-gel methods were neutron activated in a TRIGA nuclear reactor. The radioisotopes induced were analysed by gamma and beta spectrometry. The data indicate the occurrence of ^{90m}Y, ^{24}Na, trace of ^{42}K in all samples. ^{90}Y was obtained only in the samples prepared by sol-gel method. In the glass samples obtained by melts annealing procedure ^{198}Au was also evidenced. The experimental data correlated with the theoretical results regarding the neutron activation suggest the possibility to obtain radioactive microspheres with the required activity for therapeutic applications.

Keywords: bioactive and radioactive micro spheres, yttrium radioisotope, neutron activation.

Introduction

Biodegradable and nonbiodegradable materials containing neutron activable rare earth elements are widely investigated as radiation carriers inside the cancer tumors, in order to provide a high and localized dose of beta radiation [1-4]. In this way by internal radiotherapy the dose of radiation that reaches the tumours significantly increases beyond 30 Gy, which is the limit in the external radiotherapy, up to 100 Gy [4]. Biodegradable materials incorporating beta emitters could be obtained by various methods such as melt annealing or sol-gel method [1, 4]. The sol-gel method allows obtaining at relative low temperatures materials of high purity and homogeneity, with controlled rate of biodegradability. These features make the sol-gel processing a potential technique for the encapsulation of isotopes for therapeutic application [1]. Silica microspheres containing neutron activable yttrium were prepared using this procedure The materials used in radiotherapeutic applications must have high chemical purity in order to avoid the activation of undesired impurity radioisotopes [4]. The samples are designed to biodegrade after the radioisotopes decay. The chemical reactions occurring on the glass-fluid interface lead to a progressive

---

[1] Babes-Bolyai University, Faculty of Physics, Cluj-Napoca, Romania
* E-mail: cdana@phys.ubbcluj.ro
[2] Nuclear Research Institute, Pitesti, Romania.
[3] Abo Akademi University, Process Chemistry Centre, Turku, Finland

biodegradation of the glasses. It is well known that the specific feature of bioactive materials is their chemical and biological activity when exposed to physiological fluids [5]. Yttrium samples were irradiated in a nuclear reactor under thermal neutron flux, where ^{89}Y is neutron activated to form the beta emitting ^{90}Y radioisotope [6].

The aim of this study is the identification of the radioisotopes obtained by neutron activation in vitreous bioactive materials after short irradiation times, and the evaluation of their specific activity.

Materials and methods

Yttrium containing bioactive glasses were manufactured by adding different amount of yttrium oxide to the oxide mixture given in Table I. The glasses were prepared by mixing analytical grade Na_2CO_3, K_2CO_3, MgO, $CaCO_3$, $CaHPO_4(2H_2O)$, Y_2O_3 and commercial Belgian quartz sand and melting the batches in a Pt- crucible at 1360°C for 3 hours. For the glasses with high yttrium oxide content the melting temperature was 1450 °C. The glasses were cast, annealed, crushed and remelted to improve the sample homogeneity.

Table 1.

The composition of the yttrium containing glasses (wt%).

Glass	SiO_2	Na_2O	P_2O_5	CaO	B_2O_3	K_2O	MgO	Y_2O_3
HY1	48.15	5.45	3.64	18.18	0	10.91	4.55	9.09
HY1.1	46.09	5.22	3.48	17.39	0	10.43	4.35	13.04
HY3	43.91	17.39	0	15.22	0	6.52	3.91	13.04
LY1	46.09	5.22	1.74	19.13	0.87	9.57	4.35	13.04
LY2	51.96	4.35	0	13.04	2.61	9.78	5.22	13.04
LY2.1	47.8	4	0	12	2.40	9	4.8	20
LYS	53	6	2	10	0	12	2	15

Sol-gel microspheres of less than 50 μm of diameter incorporating yttrium cations were prepared by sol-gel and spray drying methods. The samples contain around 7 (7Y0) and 20 wt % (20Y0) yttrium oxide. The sols were obtained by the hydrolysis and polycondensation of tetraethoxysilane (TEOS 98 %, Aldrich) and yttrium (III) nitrate hexahydrate 99,9 % ($Y(NO_3)_3 \cdot 6 H_2O$) used as precursors.

The samples prepared by rapid quenching of melts have been neutron irradiated in a TRIGA reactor for 2125 s in a thermal neutron flux of 2.2×10^{12} n/cm²/s with $E_0 = 0.55$ eV. The ratio between the thermal neutron flux and the epithermal neutron flux was around 11.03. The gamma activity of the samples was analysed after six days by gamma spectrometry using a HpGe detector, with a volume of 100 cm³, with 20 % relative efficacy and the resolution of 1.8 keV at 1.332 MeV. The activity was measured at 10 cm distance between source and detector.

The sol-gel microspheres were placed in the neutron beam for 4245 s in a thermal neutron flux of $3.8 \cdot 10^{13}$ n/cm^2/s. The ratio between the thermal neutron flux and the epithermal neutron flux at this location was around r = 11.56. The gamma activity was measured after 20 hours delay time and beta activity after the complete decay of ^{90m}Y si ^{24}Na. The beta measurements were carried out using a system calibrated with a Sr-Y source, with 53% efficacity of the detector.

Results and discussion

Gamma spectrometry indicates the presence of ^{90m}Y, ^{24}Na, trace of ^{42}K and also ^{198}Au for the glass samples obtained by melt annealing procedure. ^{90}Y was not obtained in the samples for these irradiation conditions. The ^{198}Au activation allowed to identify the impurification of the samples melted in platinum crucibles with gold used as alloy elements beside Pt in the crucible material. The undesired transfer of gold in the melts points out that the platinum crucibles used are not proper for the preparation of high purity radiotherapeutic glasses. The use of pure platinum crucible is required for preparing radiotherapeutic glasses. The identified radioisotopes come from the neutron capture reactions:

$$^{197}\mathrm{Au}\,(n,\gamma)\,^{198}\mathrm{Au} \qquad (\sigma_o = 98.8\ \mathrm{b})$$

$$^{23}\mathrm{Na}(n,\gamma)\,^{24}\mathrm{Na} \quad (\sigma_o = 0.53\mathrm{b})$$

$$^{41}\mathrm{K}(n,\gamma)^{42}\mathrm{K} \qquad (\sigma_o = 1.45\mathrm{b})$$

where σ_o is the thermal neutron cross section of the isotopes [6,7].

The concentration of ^{198}Au was determined and the values are listed in the Table II. The presence of the Au as a impurity in the samples was confirmed also by Inductively Coupled Plasma Mass Spectroscopy (ICP-MS).

Table 2.

The specific activity of the radioisotopes induced by neutron irradiation and the concentration of Au in the samples.

Sample's code	m (g)	T_{delay} (hours)	Specific activity (µCi/g) (± 3%)		Au concentration (ppm) (±3%)
			^{198}Au	^{24}Na	
HY1	0.24896	142.6	0.367	0.35	15.41
HY1.1	0.20164	141.84	0.605	0.423	25.18
HY3	0.25046	146.72	0.846	1.172	37.12
LY1	0.30518	187.55	0.247	-	16.77
LY2	0.23388	145.26	0.525	0.261	22.6
LY2.2	0.33481	163.14	0.45	0.101	23.39
LYS	0.23694	146.014	0.67	0.428	22.02

The beta and gamma spectrometry measurements on the sol-gel irradiated microspheres indicate the presence of ^{90m}Y, ^{24}Na and trace of ^{152}Eu si ^{140}La. These traces of the ^{152}Eu and ^{140}La radioisotopes come from the precursor yttrium material used for preparing the samples. In the gamma spectra of the samples were also observed the ^{88}Y radionuclide. This radionuclide appears as a result of the ^{89}Y(n, 2n)^{88}Y reaction and has the a half time of $T_{1/2}$=106.6d, and the neutron cross section σ = 156 μb [7].

The beta measurements were carried out after the complete decay of the ^{90m}Y and^{24}Na ($T_{1/2}$ = 14.66h). Therefore the beta spectrometry results are related only to ^{90}Y radioisotopes.

The beta activity results obtained after two different delay times, T_{d1} = 18,92 h and T_{d2} = 215,25 h, from 0.0085 g of 7YO sample and 0.0103 g of 20YO sample respectively, are listed in Table III and Table IV. The radionuclide concentrations measured by Neutron Activation Analysis (NAA) are also listed. Λ_1, Λ_2 represent the activity of the samples measured after T_{d1} and T_{d2} and Λ_0 is the activity at the end of the neutron irradiation.

Table 3.
Specific activity and the concentration of radionuclides induced in the 7YO sample.

Radionuclide	Λ_0 (Bq/g)	Λ_1 (Bq/g)	Λ_2 (Bq/g)	Conc.
^{24}Na	1.95*10^{5}	7.74*10^{4}	-	-
^{90m}Y	2.96*10^{6}	4.24*10^{4}	-	2.3 wt%
^{152}Eu	1.99*10^{3}	-	1.99*10^{3}	0.68 ppm
^{140}La	1.54*10^{4}	-	378.7	0.55 ppm
^{88}Y	127.18	-	127.15	-
^{90}Y	-	-	8.776*10^{6}	-

The specific activity can be estimated depending on the activation time according to the equation [8]:

$$\Lambda_s = 10^{-9} \cdot \Phi \cdot [N\sigma(1-e^{-\lambda \cdot t_{irr}})e^{-\lambda \cdot t}]$$

where Λ_s is the specific activity at the considered time t (GBq/g), Φ is the thermal neutron flux (cm^{-2}s^{-1}), N is the number of radioisotopes in a gram of sample (g^{-1}), σ is the cross section for thermal neutron activation (cm^{-2}), λ - decay constant (h), t_{irr} is the thermal neutron activation time (h).

Table 4.
Specific activity and the concentration of radionuclides induced in the 20YO sample.

Radionuclide	Λ_0 (Bq/g)	Λ_1 (Bq/g)	Λ_2 (Bq/g)	Conc.
^{24}Na	$5.25*10^5$	$2.15*10^5$	-	-
^{90m}Y	$5.44*10^6$	$8.92*10^4$	-	3.3 wt%
^{152}Eu	3242	-	3238	1.1 ppm
^{140}La	$1.26*10^4$	-	298.13	0.96 ppm
^{88}Y	200.78	-	200.75	-
^{90}Y	-	-	$1.257*10^7$	-

The beta spectrometry measurements show that it is possible to obtain ^{90}Y radioisotope by thermal neutron activation of ^{89}Y. The NAA results indicate that the incorporation of yttrium in the 7YO sample is better than for the 20YO sample. This suggests that the preparing parameters must be adjusted function of the amount of yttrium added to the samples.

A high chemical purity of the raw materials is required in order to avoid the activation of impurities contained in these materials, like sodium, europium and lanthanum identified as ^{24}Na, ^{152}Eu, ^{140}La radioisotopes.

Conclusions

The gamma and beta spectrometry results show that ^{89}Y can be convenient activated to ^{90}Y by neutron irradiation in the investigated sol-gel samples using proper irradiation conditions. The incorporation of yttrium in the microspheres prepared by sol-gel and spray-drying methods strongly depends on the preparation conditions. The presence of gold in the samples prepared by melt annealing method indicates their contamination during the preparation procedure. The high purity of the starting materials and of crucible used for obtaining the samples is crucial in order to avoid the activation of undesired impurity radioisotopes.

REFERENCES

1. W.S. Roberto, M.M. Pereira and T.P.R. Campos: Artificial Organs 27(5) (2003), p. 420-424.
2. U.O. Häfeli, W.K. Roberts, G.J. Pauer, S.K. Kraeft and R.M. Macklis: Applied Radiation and Isotopes 54 (2001), p.869-879.
3. J. F. W. Nijsen, A. D. van het Schip, W .E. Hennink, D. W. Rook, P. P. van Rijk and J. M. H. de Klerk, Current Medicinal Chemistry 1 (2002) 73-82.

4. J.E. White and D.E. Day: Key Engineering Materials 94-95 (1994), p. 181-208.
5. L.L. Hench and J. Wilson: An Introduction to Bioceramics (World Scientific, Singapore,1993).
6. L. Moens, F. de Corte - J of Radioanalytical and Nucl. Chem. 82/2 (1984), 385-452.
7. G. Erdtmann - Neutron activation tables, Verlag Chemie-Weinhein. (1976).
8. S. Conzone, U. Hafeli, D. Day and G. Ehrhardt, J. Biomed. Mat. Res. 42, (1998) 617.

STUDIA UNIVERSITATIS BABEŞ-BOLYAI, PHYSICA, L, 2, 2005

NMR AND IR INVESTIGATION OF ALUMINOSILICATE GLASSES AS COMPONENTS OF DENTAL MATERIALS

S. SIMON*, M. VASILESCU*, M. MOLDOVAN, V. SIMON***

ABSTRACT. Aluminosilicate glasses containing approximately the same Al_2O_3 amount, usable as component of dental materials, are investigated by means of ^{27}Al Magic Angle Spinning Nuclear Magnetic Resonance (MAS-NMR) and Fourier transform infrared (FTIR) spectroscopies. Beside oxide components the sample also contain fluoride and the investigated glass powders were treated with silane. The local order around aluminium differs in the investigated samples showing changes of aluminium coordination function of glass composition. NMR technique is more sensitive than IR to describe the local aluminium environment in aluminosilicate glass systems, but IR is much proper to describe the silanisation of these glasses for a better adhesion to bone.

Introduction

Bioactive glasses are surface-active bone substitutes that have shown good biocompatibility both with bone and with soft tissue and are used in oral and maxillofacial bone augmentation [1]. Developments are directed towards the production of porous implants or implants with a suitable surface which will become invaded by bone or by connective tissue and thus held more securely but still good mechanically in place. It would be preferable if chemical bonding could be achieved between the implant and the tissues and suggestions have been made that adhesion should be possible between the collagen of bone and bioglass.

This study is mainly focussed on the structural changes occurred in aluminium surrounding in several aluminosilicate glass systems usable as filler in dental implants.

Experimental

The composition of the investigated aluminosilicate systems is given in Table 1. The fluorides were added to the oxide components in order to diminish the melts viscosity [2]. The samples were prepared by quikly undercooling to room temperature from 1300, 1350 or 1400℃, function of composition. The finely ground samples were treated with silane A-174 for obtaining a better coupling with the biologic phase, because on the surface of the powder glass samples coated with silane is expected to develop a bioactive layer in biologic media.

---

* Babes-Bolyai University, Faculty of Physics, Cluj-Napoca, Romania

**Raluca Ripan Institute of Chemistry, 3400 Cluj-Napoca, Romania

Table 1.
Composition (wt %) of aluminosilicate glass samples.

Sample Component	S1	S2	S3	S4
SiO_2	45	40	35	40
Al_2O_3	10	10	10	12
B_2O_3	17	10		5
BaO	20			
ZnO		30		
CaO			10	
Yb_2O_3			3	
P_2O_5			4.6	
ZrO_2				8
SrO			22.4	27
fluorides	8	10	15	8

Thermal analysis measurements were carried out using a MOM equipment. Thermogravimetric, differential thermogravimetric and differential thermal analysis curves were recorded in the temperature range 20-1000^{0}C, with a rate of 10^{o}C/min.

^{27}Al MAS NMR spectra were recorded at room temperature from powder samples on MAS NMR AVANCE 400 Bruker spectrometer, at 104.2MHz, in magnetic field of 9.4 T and spinning frequency 15 kHz, using $Al(NO_3)_3$ water solution as reference. The FTIR spectra were recorded on a Bruker spectrometer at room temperature using the KBr disk technique.

Results and discussions

The vitreous state of the investigated samples is attested by the X-ray diffraction patterns that consist of a large line centred around $2\theta = 27^o$. According to thermal analysis data the silane phase differently adheres on the powders obtained from the investigated glass systems as indicates the wasting of the adhered silane at temperatures up to 400^{o}C. The silane adherence is confirmed also by occurrence of silane corresponding IR absorption bands around 1720 cm^{-1} (Fig. 1). As can be seen, they are better developed in the case of S1 and S2 samples, indicating that for these glasses the silanisation process as more efficient. For the sample S3 these bands are extremely weak and for the sample S4 they are very broad. The intense IR band recorded around 1033 cm^{-1} is assigned to the asymmetric stretching of the ν(Si-O-Si) bridges affected by adjacent oxygen atoms [3-6].

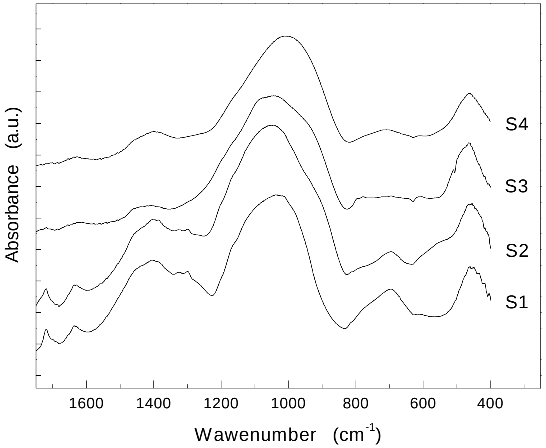

Fig. 1. Infrared spectra of aluminosilicate glass samples.

With respect to aluminium local structure, the FTIR spectra have to be inspected in the region below 900 cm^{-1}, wherein occur the contributions from the aluminum polyhedra. The spectra show for all samples the existence of chemical bonds between aluminum and oxygen atoms forming coordination groups of AlO_4 and AlO_6 types [7], with characteristic stretching vibrations typical for the Al-O bonds in the AlO_4 tetrahedra (900-650 cm^{-1}) and AlO_6 octahedra (650-400 cm^{-1}). The correlation between IR absorption bands and different types of aluminate polyhedra in glasses is based on the IR results obtained for aluminate crystals. The Al-O stretching vibrations of tetrahedral AlO_4 groups are related to the bands in the region 900 – 750 cm^{-1} and the bands in 650 – 400 cm^{-1} region are assigned to stretching modes of AlO_6 octahedra. Between these two relatively large regions would appear bands corresponding to penta-coordinated aluminium atoms, if there are [8]. On the other hand it has to be taken into account that in aluminosilicate samples also the Si–O–Si bend vibrations lead to an IR absorption peak around 460 cm^{-1} [9]. Due to this superposition of the bands it is not possible to appreciate quantitatively the relative coordination of aluminium in AlO_4 and AlO_6 structural units from IR data. The weak narrow band recorded from sample S3 at 508 cm^{-1} can be assigned to hexacoodrinated aluminium atoms partially coordinated with flour.

NMR investigation of ^{27}Al nuclei inform more properly on aluminium surrounding in aluminosilicate systems. Figure 2 shows the recorded ^{27}Al MAS NMR spectra of investigated glasses. The spectra are extended from 54 ppm to 12 ppm. Usually the ^{27}Al MAS NMR spectra in amorphous and crystalline aluminates [10-17] consist of three lines centred at 0-10 ppm, 20-40 ppm and 50-70 ppm corresponding to three types of aluminium: hexa- penta- and tetra-coordinated with oxygens, respectively. In the case of our samples the spectra show that the main contributions are coming from aluminium tetra-coordinated and hexa-coordinated. In order to estimate the relative number of tetracoordinated to hexacoordinated aluminium atoms we considered the ratio between the areas under the two corresponding peaks of the NMR spectra, taking into account that at these frequencies the right side of the AlO_4 peak is very asymmetric, reaching above –10 ppm [2]. The values obtained are summarised in Table 2. The AlO_4 structural units are prevalent versus AlO_6 ones. The tetracoordinated aluminium represents the usual structural units in aluminosilicates [2]. The fluoride addition to aluminosilicate glass systems promotes the occurrence of hexacoordinated aluminium species [18]. The maximum amount of aluminium hexacoordinated is observed in the sample S3, where a combined effect due to the presence of phosphorous and the less amount of silicon favour an octahedral environment for an important part of aluminium.

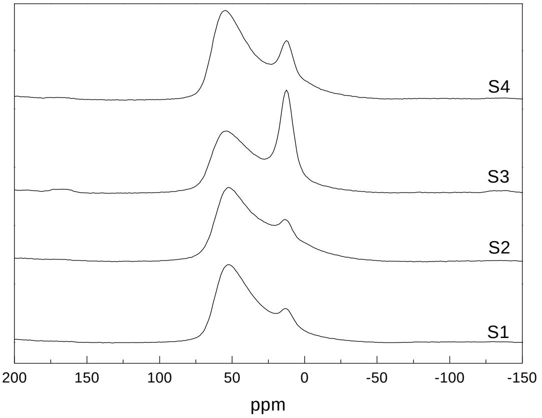

Fig. 2. ^{27}Al MAS-NMR spectra of aluminosilicate glass samples.

Table 2.

Number of tetra- and hexacoordinated aluminium estimated from ^{27}Al MAS-NMR spectra.

Sample	N_{tetra}/N_{hexa}	N_{tetra} (%)	N_{hexa} (%)
S1	28.21	96.6	3.4
S2	33.52	97.1	2.9
S3	3.51	77.8	22.2
S4	10.86	91.6	8.4

This effect is evidenced also in the IR spectrum recorded from sample S3, wherein the band centred around 690 cm^{-1}, corresponding to Al-O stretching vibrations of tetrahedral AlO_4 groups, is scarcely observable.

The number of tetracoordinated aluminium is less diminished if only SrO is added to the aluminosilicate matrix, as can be observed comparing the data for sample S4 with those for S1 and S2 glasses (Table 2). This result is reflected also in the IR spectrum of S4 sample, where the absorption band characteristic for tetracoordinated aluminium is very large but much better evidenced than for S3 sample.

Conclusions

The local structure in the investigated filler materials depend on glass composition. Both tetra- and hexacoordinated aluminium atoms are evidenced. Neither IR nor NMR results indicate pentacoordinated aluminium. The IR spectroscopic data only qualitatively indicate the changes in the aluminium coordination in these samples, but also evidenced aluminium partially with flour hexacoordinated. The number of aluminium atoms in different coordination sites, estimated from NMR results, point out that the addition of fluorides to the aluminosilicate glass matrix causes the increase of the number of hexacoordinated aluminium atoms. This effect could be of interest for the surface properties of filler materials with respect to their behaviour as biomaterials, showing that the best silanisation takes place for the samples wherein the aluminium is tetracoordinated.

REFERENCES

1. I.D. Xynos, A.I. Edgar, L.D.K. Buttery, L.L. Hench, J.M. Polak, J. Biomed. Mater. Res, **55**, 151 (2001)
2. Q. Zeng, J.F. Stebbins, Am. Mineral., 85, 863 (2000)
3. P. H. Gaskell, D. W. Johnson, J. Non-Cryst. Solids, **20**, 153 (1976)
4. C.T. Kirk, Phys. Rev. B, **38**, 1255 (1988)
5. E.I. Kamitsos, Phys. Rev. B, **53**, 14659 (1996)
6. P. Li, G. Z. Wang, Y.R. Ma, R.C. Fang, Phys. Rev. B, **58**, 4057 (1998)
7. H. Scholze, Glass: Nature, Structure and Properties, Springer, New York, (1991)
8. B.T. Poe, P.F. McMillan, C.A. Angell, R.K. Sato, Chem. Geology, 96, 333 (1992)
9. S. Abiraman, H.K. Varma, T.V. Kumari, P.R. Umashankar, A. John, Bull. Mater. Sci., **25**, 5, 419 (2002)
10. M.E. Smith, Appl. Magn. Reson., 4, 1 (1993)

11. R.K. Sato, P.F. McMillan, P. Dennison, R. Dupree, J. Phys. Chem., 95, 4483 (1991)
12. D. Iuga, S. Simon, A.P.M. Kentgens, E. de Boer , J. Phys. Chem. B, **3**, 103, 7591 (1999)
13. P.E. Stallworth, P.J. Bray, in Glass Science and Technology, Eds. D.R. Uhlmann and N.J. Kreidl, Acad. Press Inc., Boston, 1990, p. 77-100
14. B.C. Bunker, R.J. Kirkpatrick, R.K. Brow, G.L. Turner, C. Nelson, J. Am. Ceram. Soc. **6**, 14, 30 (1991)
15. R.K. Brow, D.R. Tallant, G.L. Turner, J. Am. Ceram. Soc. **79**, 9, 1410 (1996)
16. S. Simon, G.J.M.P. van Moorsel, A.P.M. Kentgens, E. de Boer, Solid St. NMR, 5, 163 (1995)
17. L. Züchner, J.C.C. Chan, W. Müller Warmuth, H. Eckert, J. Phys. Chem. B, 102, 4495 (1998)
18. J.F. Stebbins, S. Kroeker, S.K. Lee, T.J. Kiczensky, J. Non-Cryst. Solids, 275, 1 (2000)

STUDIA UNIVERSITATIS BABEŞ-BOLYAI, PHYSICA, L, 2, 2005

EFFECT OF ANNEALING TIME ON THE $Bi_{1.6}Pb_{0.4}Sr_{1.6}Ca_{2.0}Cu_{2.8}O_X$ SYSTEM

A. SIMON[1*], S. D. ANGHEL[1], I. G. DEAC[1], T. FRENȚIU[2],
G. BORODI[3] AND S. SIMON[1]

ABSTRACT. A superconducting sample with nominal composition $Bi_{1.6}Pb_{0.4}Sr_{1.6}Ca_{2.0}Cu_{2.8}O_x$ was investigated. It was annealed in air, at 845 °C, for 50, 150 and 200 hours. The samples were investigated via AC susceptibility measurements and XRD. The elemental content of the samples (concentrations and stoichiometric coefficients) was studied via plasma source atomic emission spectroscopy. It was established that the Pb content decreases linearly with the annealing time. The results of the investigations indicate that an extensive heat treatment could cause an alteration of the 2223 phase and its transformation in lower T_C phases.

1. Introduction

The Bi-based superconducting family consists of three superconducting phases with quite similar crystal structures and general chemical formula: $Bi_{2-x}Pb_xSr_2Ca_{y-1}Cu_yO_{10+\delta}$, where y = 1, 2, 3 corresponds to the 2201 (T_C ~ 20 K), 2212 (T_C ~ 80 K) and 2223 (T_C ~ 110 K) phases respectively. The discovery of the Pb-free 2223 phase [1] was quickly followed by the synthesis of the Pb substituted 2223 [2]. It was found that the incorporation of Pb might speed up the formation of 2223 phase. The practical applications of high T_C superconductors may require samples under various aspects (bulk, tape, wire, and thin or thick films); therefor extra processing is also needed. Among these techniques, annealing is probably the most important and frequent.

The aim of the present paper is to investigate the influence of the annealing time on properties and structure of the starting system $Bi_{1.6}Pb_{0.4}Sr_{1.6}Ca_2Cu_{2.8}O_x$.

2. Experimental details

The starting sample used for further treatments and investigations was purchased from ALDRICH as fine black powder and has the nominal formula $Bi_{1.6}Pb_{0.4}Sr_{1.6}Ca_2Cu_{2.8}O_{9.2+x}$ with x = 0.45. The powder was pressed at

---

[1] "Babeş-Bolyai" University, Faculty of Physics, 3400 Cluj-Napoca, ROMANIA
∗ coresponding author, E-mail: asimon@phys.ubbcluj.ro
[2] "Babeş-Bolyai" University, Faculty of Chemistry, 3400 Cluj-Napoca, ROMANIA
[3] Institute of Molecular and Isotopic Technologies, 3400 Cluj-Napoca, ROMANIA

200 atm in a cylindrical pellet and annealed in air, at a temperature of 845 ^{o}C, in a CARBOLITE RHF 16/3 owen for 50, 150 and 200 hours. The critical temperature of the superconducting phases was determined by the AC susceptibility method, the measurements being performed with the Oxford Instruments MagLab System 2000 (frequency: 1 kHz, magnetic field: 1 Oe). The superconducting phase formation was investigated via X-ray diffraction (XRD) on a Dron 2 system, using the clasical powder method with Cu K_{α} radiation and Ni filter. The composition of the samples was determined by inductively coupled plasma atomic emission spectrometry technique (ICP-AES).

3. Results and discussion

Fig.1 shows the temperature dependence of the real component of the AC susceptibility for the original and annealed samples.

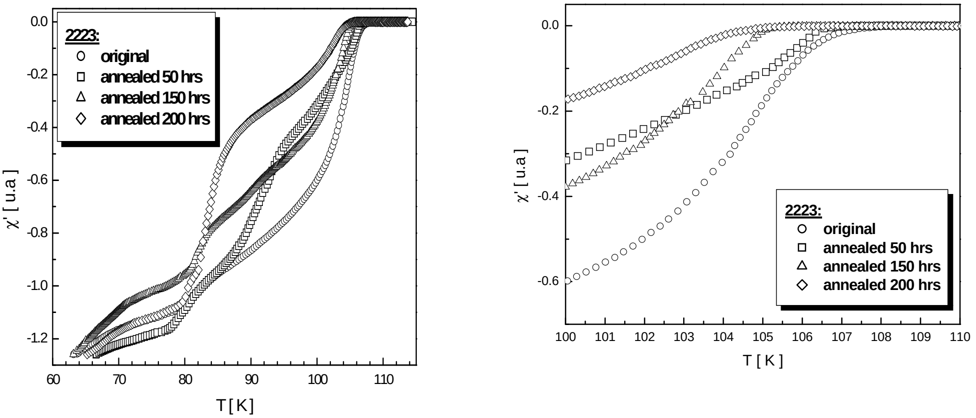

Fig. 1. Temperature dependece of the real component of the AC susceptibility for the original and annealed samples and the magnification of the onset region

Analysing these dependences one can say that next to the usual low (> 80 K) and high T_C (> 100 K) phases, an intermediate phase appeared with T_C ~ 91 K. This phase does not exist in the original sample. It appears after 50 hours of annealing and it is still present after 150 hours, but disappears after a treatment of 200 hours.

A survey of the literature [3] suggests that this value of the critical temperature corresponds to the 2212 phase: with excess of Bi and Sr and deficit of Ca ($Bi_{2.18}Sr_{2.20}Ca_{0.80}Cu_{2.00}O_{x}$) or with deficit of Bi

($\mathrm{Bi_{1.90}Sr_{2.00}Ca_{1.00}Cu_{2.00}O_x}$) or its appearance is due to changes in the oxygen stoichiometry or it is connected somehow to the intercalation of Pb (forming of PbBi2212 phase) [4, 5]. Regarding T_C^{onset}, the magnification of the onset region shows that this temperature changes from 108 K (original) to 107 K (50 hrs) or 105 – 106 K (150 and 200 hrs). The critical temperatures and the onset of the transitions are synthetized in Table 1. One can say that, the annealing time has no significant effect either on the critical temperature or the onset temperature.

Table 1.

Critical temperatures and onset of transitions

Sample	**T_C for superconducting phases**			**T_C^{onset}**
	low	**"intermediate"**	**high**	
original	80 K	absent	105 K	108 K
annealed 50 hrs	80 K	92 K	105 K	107 K
annealed 150 hrs	82 K	91 K	104 K	106 K
annealed 200 hrs	84 K	absent	103 K	105 K

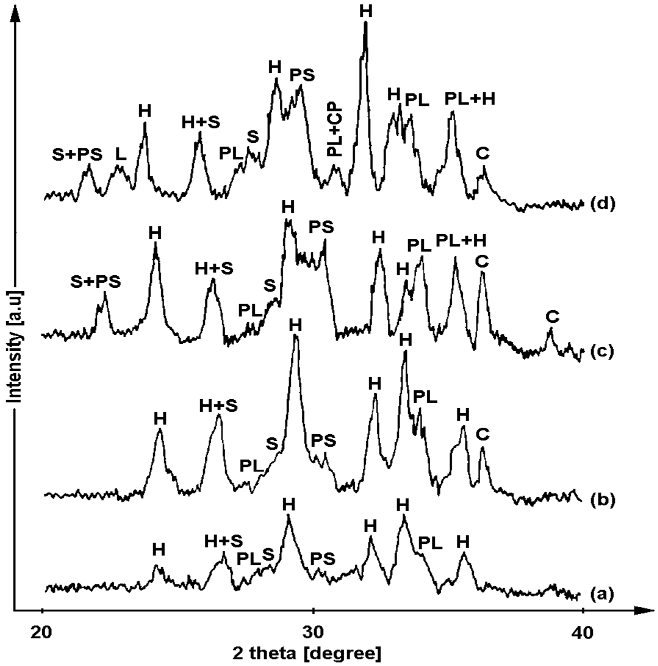

Fig. 2. – XRD patterns for $\mathrm{Bi_{1,6}Pb_{0,4}Sr_{1,6}Ca_2Cu_{2,8}O_x}$ samples:
(a) – original; (b) – annealed 50 hrs; (c) – annealed 150 hrs; (d) – annealed 200 hrs

Fig. 2 shows the results of XRD analysis. As it was suggested by the dependence of the real component of the AC susceptibility on temperature, all samples have all the three characteristic phases for the Bi based superconducting family. Due to the fact that the most proeminent lines of those phases are overlaped, any estimation of the volumic fractions of the phases could lead to erroneous conclusions. Analysing these XRD patterns one can say:

(i) the original sample has the three characteristic phases of the Bi family (2201 – "S", BiPb2201 – "PS", BiPb2212 – "PL" and 2223 – "H"), but phase 2223 in majoritary and there are no non – superconducting type impurities (CuO, Ca_2CuO_3, Ca_2PbO_4).

(ii) after annealing the original sample for 50 hours more diffraction lines could be observed, among them the characteristic lines for CuO ("C") and BiPb2201 phases. The presence of the "intermediate" phase was confirmed, but its distinct identification was not possible due to overlappings. The changes in phase ratios could be easily observed.

(iii) after an annealing time of 150 hours there are more impurities and very low T_C phases in the samples, their presence being proved by the aspect of the XRD pattern. The 2223 phase content of the sample was lowered and at angles of 33^o – 33.5^o a structural change from tetragonal to orthorombic could be observed [3, 6]. The presence of the "intermediate" phase was confirmed, but its distinct identification was not possible due to overlappings.

(iv) after 200 hours of annealing some of the lines are more accurate. A significant degradation of the 2223 could be observed. Meantime the number of BiPb2212, 2212 ("L") and 2201 lines is increasing. Beside CuO, Ca_2PbO_4 ("CP") impurities appeared in the sample.

Fig. 3 and Table 2 presents the change in the Pb atomic ratio as function of annealing time. This graph demonstrate that Pb content (both atomic ration and concentration) reduces in time almost in a linear mode. The influence of the annealing time on the other elements (Bi, Sr, Ca, Cu) and on a Bi2212 type superconductor ($Bi_2Sr_2CaCu_2O_x$) is presented elsewhere [7].

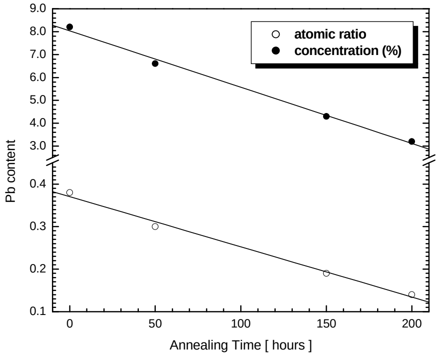

Fig. 3. – Change in Pb content as function of annealing time

Table 2.
Pb content as function of annealing time

Sample	**Pb**		
	concentration [%]		**atomic ratio**
	normal *	**relative** **	
original	8 ***	–	0.4
	8.2 ± 0.2 ****	100.00	0.38 ± 0.02
annealed 50 h	6.6 ± 0.3	80.48	0.30 ± 0.02
annealed 150 h	4.3 ± 0.3	52.44	0.19 ± 0.01
annealed 200 h	3.2 ± 0.2	39.02	0.15 ± 0.02

Legend:

*	as it was
**	normalized to the Pb concentration in the original sample
***	theoretical
****	experimentally determined

4. Conclusions

In this paper results on the influence of annealing time on properties and structure of the starting system $Bi_{1.6}Pb_{0.4}Sr_{1.6}Ca_2Cu_{2.8}O_x$ has been presented. Inductively coupled plasma atomic emission spectroscopy analyses show an almost linear reduction in Pb concentration with the increase of annealing time. Both AC susceptibility measurements and XRD analysis demonstrate the existence of all the three superconducting phases during annealing: 2201, 2212 and 2223. The results of the investigations indicate that an extensive heat treatment could cause an alteration of the 2223 phase and its transformation in lower T_C phases, due to the volatilization of constituent elements other than Pb (Bi and Sr). The results presented in this paper are in good agreement with those presented by other authors [4, 5].

REFERENCES

1. H. Maeda, Y. Tanaka, M. Fukutomi, T. Asano: Jpn. J. Appl. Phys. **27** (1988) L209
2. M. Takano, J. Takada, K. Oda, H. Kitaguchi, Y. Miura, Y. Ikeda, Y. Tomii, H. Mazaki: Jpn. J. Appl. Phys. **27** (1988) L1401
3. P. Majewski: J. Mater. Res. **15** (2000) 854
4. K. Konstantinov, S. Karbanov, A. Souleva, D. Kovacheva: Supercond. Sci. Technol. **3** (1990) 309
5. K. Sarkar, B. Kumar, I. Maartense and T. L. Peterson: J. Appl. Phys. **65**, 2392, 1989
6. Jeremie, K. Alami-Yadri, J. C. Grivel and R. Flukiger: Supercond. Sci. Technol. **6**, 730, 1993
7. Simon, S. D. Anghel, T. Frentiu, G. Borodi, I. G. Deac and S. Simon: Studia Univ.”Babes–Bolyai” Cluj, Physica, XLIX, nr.1, 69 – 74, 2004

STUDIA UNIVERSITATIS BABEŞ-BOLYAI, PHYSICA, L, 2, 2005

INFRARED INVESTIGATION OF BISMUTHATE HEAVY METAL OXIDE GLASSES

S. SIMON[*], M. TODEA

ABSTRACT. Fourier transform infrared (FTIR) spectroscopic results were used to investigate the changes induced in the local structure of samples as the ratio between Bi_2O_3 and SiO_2 content changes from 3:1 to 2:3. The environment of constituent cations was investigated both in vitreous and partially crystallised samples of same composition. Progressive substitution of Bi_2O_3 by SiO_2 contributes to the structural relaxation of vitreous network and enhances glass stability. By crystallisation heat treatment the structural units appear to be more uniform as results from the narrowing of corresponding IR bands. FTIR results show that more affected by composition and heat treatment is the environment of bismuth than that of silicon.

Keywords: Heavy metal glasses, glass-ceramics, FTIR, local order.

Introduction

Despite the fact that Bi_2O_3 is not a classical glass former, due to its high polarisability the coordination number of Bi^{3+} cations may decrease and in the presence of conventional glass formers they may build a glass network of $[BiO_3]$ pyramids [1, 2]. Bismuth-silicate glasses acquired special applications as low loss optical fibres, infrared transmitting materials or as active medium of Raman-active fibre optical amplifiers and oscillators [3-4].

In all optical switching and broadband amplification devices are used glasses based on bismuth oxide [5] characterised by high non-linear optical susceptibility. Bismuth based glasses are also used to produce after appropriate annealing high temperature superconductors with controllable microstructure [6-8].

However, the structural role played by Bi_2O_3 in glasses without or with low content of conventional glass formers is complicated and poorly understood. The problem is complex because crystalline Bi_2O_3 can form several polymorphs with highly distorted corner-, and edge-sharing polyhedra and consequently the structural model for $xSiO_2 \cdot (100-x)Bi_2O_3$ glasses is still under discussion [9, 10].

Several techniques have been employed in the attempt to identify the local environment of the different elements in bismuthate glasses. Infrared spectroscopy can provide important information on the local structure in vitreous and ceramic materials.

---

[*] Corresponding author: simons@phys.ubbcluj.ro, Babes-Bolyai University, Faculty of Physics, Cluj-Napoca, Romania

This paper is focused on the structural changes induced in heavy metal glass samples by progressive substitution of Bi_2O_3 with SiO_2 and by heat treatment such as they are experienced by the vibrations of the constitutive structural units.

Experimental

Glass samples belonging to $0.01Fe_2O_3 \cdot 0.99[xSiO_2 \cdot (100\text{-}x)Bi_2O_3]$ system ($10 \leq x \leq 60$ mol %) were prepared using $BiO(NO_3) \cdot H_2O$, SiO_2 and Fe_2O_3 of analytical grade purity. Corresponding amounts of reagents were mixed and melted in sintercorundum crucibles for 10 minutes at 1200℃. The samples were obtained by fast quenching of the melts cast and pressed between steel plates at room temperature. X-ray powder diffraction analysis did not reveal any crystalline phase. The vitreous samples were partially crystallised by heat treatment applied at 600^oC for 24 hours.

The FTIR spectra were recorded with a resolution of 4 cm^{-1} on a Bruker spectrophotometer at room temperature using the KBr disk technique.

Results and discussion

The bismuth-silicate samples doped with 1 mol % Fe_2O_3 are transparent and coloured from yellow-brown to red-brown as SiO_2 content increases from 10 to 60 mol %. The IR absorption bands recorded in the spectral range 400-2500 cm^{-1} both for glass and vitroceramic samples are given in Fig. 1. Beside the apparent similarity of the FTIR spectra recorded from the investigated samples the IR analysis of $xSiO_2 \cdot (100\text{-}x)Bi_2O_3$ matrix is awkward due to the fact that several absorption bands of silicon structural units occur in the same wavenumber range as that of bismuth units. However the mindful watching of the expanded spectra evidence structural changes both with composition and heat treatment. From the vitreous samples (Fig. 2) are recorded IR bands around 480 and 610 cm^{-1} and very large shoulders around 730 and 860 cm^{-1}. The bands around 480 cm^{-1} can be assigned both to Si–O–Si bend vibrations [11-15].

According to the literature the IR absorption peak around 840 cm^{-1} arises from vibration of Si-O bonds in $[SiO_4]$ structural units of Q^2 type [16]. The absorption bands around 610 cm –1 can be assigned to internal vibration modes of SiO_4 structural units [17] while the shoulder at 860 cm^{-1} is related to vibrations of $[BiO_6]$ octahedral units [18-20].

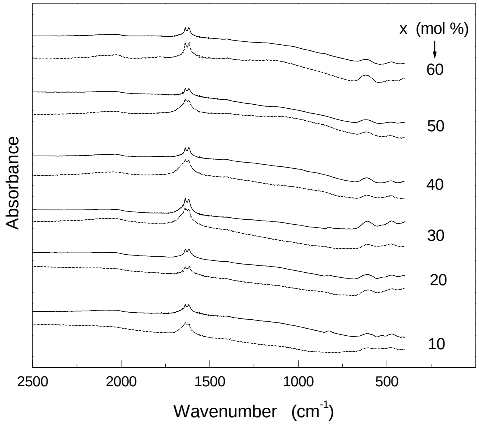

Fig. 1. FTIR spectra of $0.01Fe_2O_3 \cdot 0.99[xSiO_2 \cdot (100-x)Bi_2O_3]$ glass (short dotted lines) and vitroceramic (solid lines) samples.

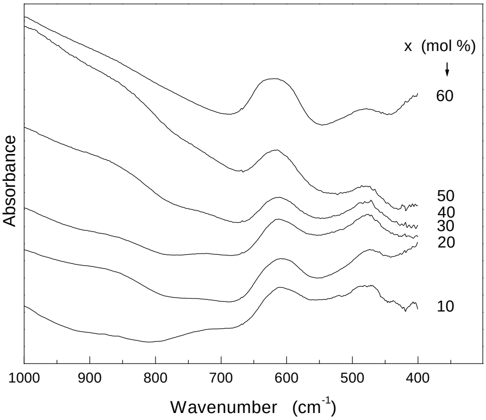

Fig. 2. FTIR spectra of $0.01Fe_2O_3 \cdot 0.99[xSiO_2 \cdot (100-x)Bi_2O_3]$ glass samples in the spectral range 1000-400 cm^{-1}.

For the glass samples one also remarks that the position of the weak shoulder noted around 860 cm^{-1} for x = 10 and assigned to $[BiO_6]$ units shifts to lower wavenumbers as SiO_2 content increases and for x =50 it appears around 830 cm^{-1}, that is related to assigned to $[BiO_3]$ units.

By inspecting the spectra IR spectra obtained from heat treated samples (Fig. 3) one observes the occurrence of new absorption bands around 530 and 830 cm^{-1} for the samples with x = 10, 20 and 30. These bands are assigned to the Bi-O bond vibrations in [BiO_6] octahedral units, respectively in [BiO_3] pyramidal units [19, 20].

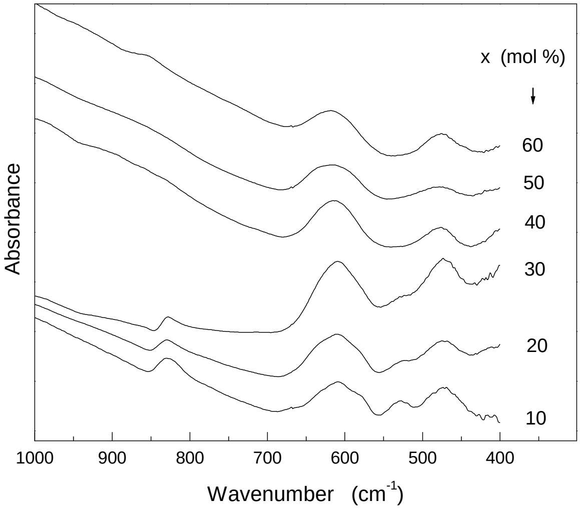

Fig. 3. FTIR spectra of $0.01Fe_2O_3{\cdot}0.99[xSiO_2{\cdot}(100\text{-}x)Bi_2O_3]$ in the spectral range 1000-400 cm^{-1} for partially crystallised samples.

They are not recorded from the partially crystallised samples with x = 40, 50 and 60 but for x = 60 appears a weak band around 850 cm^{-1}. The position of this band is between that of the IR absorption bands assigned to [BiO_3] units (830 cm^{-1}), [SiO_4] units (840 cm^{-1}) and that assignable to [BiO_6] units (860 cm^{-1}).

The investigated samples ($10 \leq x \leq 60$ mol %) are heavy metal glasses [4]. The expected structural units building the glass network are [BiO_3] pyramidal and [BiO_6] octahedral units, without to exclude the occurrence of [SiO_4] tetrahedral units. The increased addition of SiO_2 contributes to the structural relaxation of vitreous network.

The structural role of Bi ions in Bi_2O_3-SiO_2 system impurified with 1 mol % Fe_2O_3 was investigated using several techniques by Nanba et all [10]. They evidenced structural similarities between $50Bi_2O_3{\cdot}50SiO_2$ glass and Bi_2SiO_5 crystal and showed that in $50Bi_2O_3{\cdot}50SiO_2$ glass, Bi ions occupied BiO_6 sites, and the BiO_6 units were surrounded by eight BiO_6 units sharing their edges. They classified the oxygen sites into three groups, Si-O-Si, Si-O-Bi and Bi-O-Bi, whose respective populations were estimated as 20%, 40% and 40% in $50Bi_2O_3{\cdot}50SiO_2$ glass. It was concluded that the Bi-O-Bi bridges formed layers, the Si-O-Si bridges formed chains of Q^2 units, and the bismuthate layers were joined with the silicate chains. It was found that the Bi-O-Bi networks existed over the whole glass forming region. In Bi_2O_3-SiO_2 system, however, Bi-O-Bi networks alone could not form glass, and Si-O-Si networks were indispensable for the glass formation.

Conclusions

The IR results show that the local order in $xSiO_2\cdot(100-x)Bi_2O_3]$ system, for $10 \leq x \leq 60$ mol %, as the ratio between Bi_2O_3 and SiO_2 content changes from 3:1 to 2:3, modifies with the substitution degree of Bi_2O_3 by SiO_2. One remarks that for low SiO_2 contents dominate the bismuth structural units of $[BiO_6]$ type and as SiO_2 content increases is noted the tendency of bismuth to enter in structural units of $[BiO_3]$ type. The partial crystallisation of samples with low SiO_2 content ($x < 40$ mol %) leads to appearance of new IR absorption bands that signalise new structured $[BiO_3]$ and $[BiO_6]$ units.

Acknowledgements

This research was partial financially supported by Romanian National University Research Council.

REFERENCES

1. W.H. Dumbaugh, Phys. Chem. Glasses, **27,** 119 (1986),
2. D. Sreenivasu, V. Chandramouli, Bull. Mater. Sci., **23**, 4, 281 (2000)
3. J. Yang, S. Dai, N. Dai, S. Xu, L. Wen, L.Hu, Z. Jiang**,** Journal of the Optical Society of America B: Optical Physics, 20, 5, 810 (2003)
4. W.H. Dumbaugh, J.C. Lapp, J. Am. Ceram. Soc., 75, 9, 2315 (1992)
5. N. Sugimoto, Am. Ceram. Soc., **85**, 5, 1083 (2002)
6. T. Komatsu, R. Sato, K. Imai, K. Matusita, T. Yamashita, Jap. J. Appl. Phys., 27, L550 (1998);
7. D.G. Hinks, L. Soderholm, D.W. Capone II, B.Dabrowski, A.W. Mitchell, D. Shi, Appl. Phys. Lett., 53, 423 (1988)
8. T. Minami, Y. Akamatsu, M. Tatsumisago, N. Toghe, Y. Kowada, Jap. J. Appl. Phys., 27, L777 (1998)
9. Witkowska, J. Rybicki, A. DiCicco, 6-thInternational Conference on Intermolecular Interactions in Matter, Gdańsk – Poland, 10-13 September 2001
10. T. Nanba, H. Tabuchi, Y. Miura, Proceedings of XX Int. Congress. Glass, Sept. 27- Oct. 1, 2004, Tokyo, Japan, P-10-011

11. S. Abiraman, H.K. Varma, T.V. Kumari, P.R. Umashankar, A. John, Bull. Mater. Sci., **25**, 5, 419 (2002)]
12. V. Dimitrov, Y. Dimitriev, A. Montenero, J. Non-Cryst. Solids, 180, 51 (1994)
13. R.M. Almeida, A.A. Kharlamov, J. Heo, J. Non-Cryst. Solids, 202, 233 (1996)
14. R. Iordanova, V. Dimitrov, Y. Dimitriev, D. Klissurski, J. Non-Cryst. Solids, 180, 58 (1994)
15. R. Iordanova, Y. Dimitriev, V. Dimitrov, S. Kassabov, D. Klissurski, J. Non-Cryst. Solids, 231, 227 (1998)
16. J. P. Borrajo, S. Liste, J. Serra, P. Gonzalez, S. Chiussi, B. Leon, M. Perez-Amor, H. O. Ylanen, M. Hupa,Key Eng. Mat., 254-256, 23 (2004)
17. Gow-Weng Peng, Shou-Kang Chen, Hok-Shing Liu, Appl. Spec., **49**, 11, 1646 (1995)
18. Y. Hu, N.H. Liu, U.L. Lin, J. Mater. Science, 33, 229 (1998)
19. L. Baia, R. Stefan, W. Kiefer, J. Popp, S. Simon, J. Non-Cryst. Solids, 303, 379 (2002)
20. L. Baia, R. Stefan, J. Popp, S. Simon, W. Kiefer, J. Non-Cryst. Solids, 324, 109 (2003).

STUDIA UNIVERSITATIS BABEŞ-BOLYAI, PHYSICA, L, 2, 2005

ATR-FTIR INVESTIGATIONS OF SECONDARY STRUCTURE OF LYOPHILIZED BLOOD PLASMA IN PREGNANCY INDUCED HYPERTENSION

LAVINIA SABĂU[1], G.DAMIAN[2]

ABSTRACT. Pregnancy-induced hypertension (PIH) knowns by many clinical names as toxaemia, gestational proteinuric hypertension and preeclampsia is not a simply high blood pressure, but is a pregnancy condition which must be taken seriously as it can pose a serious risk to health of both mother and baby. This is certainly one of the characteristic signs of the condition, the others being protein in the urine and fluid retention. By biocheemical investigations, we found significantly higher values ($p<0.001$) of serum carbonyl content of proteins in patients with preeclampsia than in healthy pregnant women having the same gestational age. These results illustrate a great production of reactive oxygen species for pregnant women with preeclampsia. Many studies have shown that reactive oxygen species produced in excess modify the structure of proteins, lipids and nucleic acids. The changes in the secondary structure of blood plasma, we have investigated in the lyophilized blood plasma from 30 patients, healty and with different degree of diseases, by ATR-FTIR spectroscopy. In case of patients with preeclampsia the ATR-FTIR spectroscopy reveals a decrease in α-helix and β-sheet content and an increasing of aggregates content. The changes in the secondary structure of blood plasma observed by ATR-FTIR spectroscopy are in perfect correlation with the results obtained from the biochemical method of determination the damage on proteins due to oxidative stress.

Keywords: PIH , preeclampsia, ATR-FTIR, proteins, secondary structure

Introduction

Pregnancy-induced hypertension (PIH) is a frequent disorder that complicates the second trimester of pregnancy, producing increased maternal and fetal morbidity. In spite of this, the mechanisms involved in the pathogenesis of this disorder have not been completely understood. The cause of inadequate trophoblastic invasion in preeclampsia is still unclear, but it is known that this deficient trophoblastic invasion along with the imbalance of vasoconstrictor and vasodilatator factors results in preeclampsia [1].

The aim of our study was to study the effect of on the changes in the secondary structure of blood plasma by ATR-FTIR spectroscopy and to investigate whether these changes are correlated with the plasma levels of protein degradation products of reactive oxygen species in the organism and

---

[1] University of Medicine and Pharmacy “Iuliu Hațieganu”, Faculty of Medicine, Dept. of Physiology, Cluj-Napoca, Romania,

[2] ”Babes-Bolyai” University, Faculty of Physics, Dept. Biomedical Physics, Cluj-Napoca, Romania

with the plasma levels of antioxidants. In order to study the effect of PIH on the changes in the secondary structure of blood plasma, we have investigated the changes in lyophilized blood plasma from pregnant patients, healty and with different degree of diseases, by ATR-FTIR spectroscopy. Attenuated total re£ection Fourier transform infrared spectroscopy (ATR-FTIR) is one of the most powerful methods for recording infrared spectra of biological materials in general, and for proteins in particular. It is fast, yields a strong signal with only a few micrograms of sample, and most importantly, it allows information about the orientation of various parts of the molecule under study to be evaluated in an oriented system [2,3]. The environment of the molecules can be modulated so that their conformational changes in secondary structure, can be studied [4, 5]. Because a biomolecule is determined by its unique structure, each biomolecule will exhibit a unique FT-IR spectrum, representing the vibrations of its structural bonds. Furthermore, every biomolecule present in the sample will exhibit more or less specific FT-IR absorption peaks. Thus, a plasma FT-IR spectrum will exhibit absorption peaks related to its major components (mainly serum albumin). The changes in secondary structure refers to changes in ratio among three common structures, namely alpha helices, beta sheets, and turns. That which cannot be classified as one of the standard three classes is usually grouped into a category called “other”, “random coil” or agregates. Protein aggregates play a large role in human diseases affecting human health. Structural information of lyophilized blood plasma is obtained by analysis of the conformationally-sensitive amide I and amide III bands using Attenuated Total Reflectance FT-IR spectroscopy. The second derivative spectrum was performed in order to overcome the bands overlapping due to the different C=O stretching vibrations of each type of secondary structure (i.e. α-helix, β-sheet, turns and unordered). The results of qualitative and quantitative analysis by curve fitting to the inverted second derivative spectra of amide I features [6,7] of proteins from blood plasma, reveal a decrease in α-helix and β-sheet content and and an increasing of aggregates content for patients affected dy PIH.

Material and Methods

We included in our study 15 pregnant patients (age between 18 and 32 years old) having gestational age from 23 to 38 weeks with moderate and severe forms of preeclampsia and 15 healthy pregnant women (age between 18 and 32 years old) having the same gestational age. The healthy pregnant patients were selected following clinical and usual laboratory examinations that were within normal limits. The pregnant women who had arterial hypertension before the period of pregnancy were excluded from our study. We have investigated the changes in lyophilized blood plasma from all 30 patients by ATR-FTIR spectroscopy and we established for all patients the following blood tests:

- The serum level of carbonyl content of proteins (they result from the reaction between reactive oxygen species and proteins in organism) using the Reznick method [8]
- The hydrogen donating ability of serum (that reflects the serum antioxidant capacity) using the Hatano method [9]

Acquired data were analyzed from statistical point of view using the Student test.

- The levels of nitrate and nitrite (which are the products of nitric oxide degradation in organism) using the Griess reaction [10].

The blood plasma was lyophilized for 30 hours at $–5^0$ C and than used as powder sample for ATR-FTIR investigation. The FT-IR spectra of samples of blood plasma were recorded in the region 4000-800 cm^{-1} by a Bruker EQUINOX 55 spectrometer OPUS software, using an Attenuated Total Reflectance accessory with a scanning speed of 32 cm^{-1} min^{-1} with the spectral width 2.0 cm^{-1}. The internal reflection element was a ZnSe ATR plate (50 x 20 x 2 mm) with an aperture angle of 45°. A total of 1 28 scans were accumulated for each spectrum. Spectra were recorded at a nominal resolution of 2 cm^{-1}. The resultant spectra were smoothed with a 9-point Savitsky–Golay smooth function to remove the white noise. The second derivative spectral analysis was applied to locate positions and assign them to different functional groups [13]. Before starting the fitting procedure, the obtained depths of the minima in the second derivative spectrum and, subsequently, the calculated maximum intensities were corrected for the interference of all neighbouring peaks. All second-derivative spectra, calculated with the derivative function of Opus software, were baseline-corrected, based on the method of Dong and Caughey [2], and area-normalized under the second derivative amide I region, 1700–1600 cm^{-1} and amide III region, 1330-1230 cm^{-1} [14]. The curve fitting is performed by stepwise iterative adjustment towards a minimum root-mean-square error of the different parameters determining the shape and position of the absorption peaks. The inverted second-derivative spectra were obtained by multiplying by –1 the second-derivative spectra. Curve fitting was performed by setting the number of component bands found by second-derivative analysis with fixed bandwidth (12 cm^{-1} for amide I and 14 cm^{-1} for amide III) and Gaussian profile. The best-average fit gave the intensity of each component band for each spectrum. The area under each peak was used to calculate the percentage of each component and finally used to analyze the percentage of secondary structure components.

Results and Discussions

We found significantly higher values ($p<0.001$) of serum carbonyl content of proteins in patients with preeclampsia than in healthy pregnant women having the same gestational age (Fig.1). These results illustrate a great production of reactive oxygen species for pregnant women with preeclampsia.

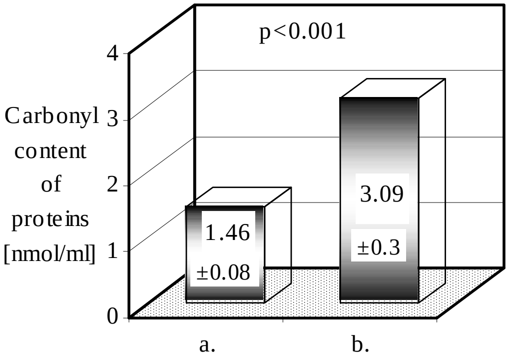

Fig 1. Variation of serum carbonyl content of proteins at patients with PIH: (a) Healthy pregnant women; (b). Patients with PIH

On the other hand, the serum levels of hydrogen donating ability of serum (that reflects the serum antioxidant capacity) were found significantly lower ($p<0.001$) compared with those in healthy pregnant women having the same gestational age (Fig.2). The levels of antioxidants were found to be decreased because they were used for the neutralization of reactive oxygen species produced in excess in pregnant patients with preeclampsia, these antioxidants being consumed in these neutralization reactions. Therefore we can affirm that oxidative stress occurs in preeclampsia. In addition, the levels of nitrates and nitrites as nitric oxide degradation products in the organism were found significantly lower ($p<0.001$)for patients with preeclampsia compared to healthy pregnant women (Fig. 3). Nitric oxide is one of the vasodilatators factors in normal pregnancy. If reactive oxygen species are produced in excess, nitric oxide is consumed in the reaction with superoxide anion [11].

Reactive oxygen species produced in increased amounts in preeclampsia contribute to the accentuation of the imbalance of vasoconstrictor and vasodilatator factors due to their reaction with nitric oxide, known as a vasodilatator factor.

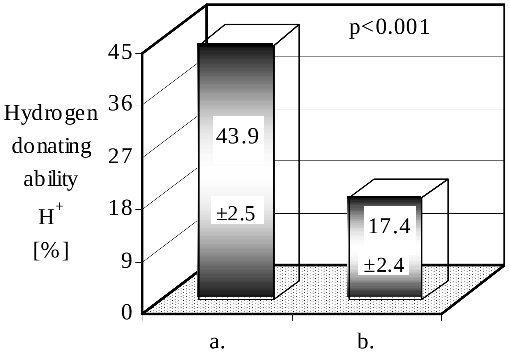

Fig.2. Variation of hydrogen donating ability of serum at patients with PIH: (a). Healthy pregnant women; (b). Patients with PIH

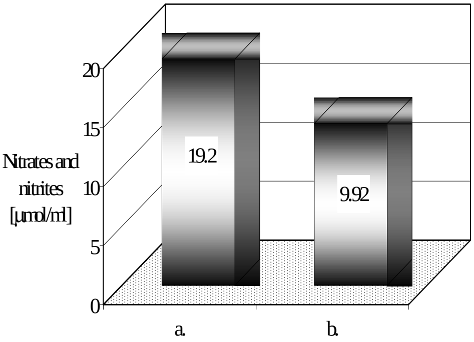

Fig.3. Variation of the serum nitrates and nitrites at patients with PIH: (a). Healthy pregnant women; (b). Patients with PIH

Moreover, in patients with preeclampsia the ATR-FTIR spectroscopy reveals a decrease in α -helix and β-sheet content and an increasing of aggregates content. Structural information were obtained by analysis of the conformationally-sensitive amide I band located between 1600 and 1700 cm^{-1} and amide III located in the spectral region 1215-1335 cm^{-1}. The amide I band (Fig.4) is due to the in-plane C=O stretching vibration, weakly coupled with C–N stretching and in-plane N–H bending. Each type of secondary structure (i.e. α-helix, β-sheet, β-turn and unordered) gives rise to different C=O stretching frequencies, and, hence, results in characteristic band positions. Band positions are used to determine the secondary structural types present in each protein. The relative band areas (determined by curve fitting) can then be used to quantitate the relative amount of each structural component. The α-helix content, is estimated to be approximately in range of 35-40% for healthy pregnant women and in the range of 23-28% for patients with PIH. The amide III (Fig.5) is a more complex vibrational mode. It mainly is the in-phase combination of NH in-plane-bending and CN stretching with contributions from CC stretching and CO in-plane-bending depending on the details of the force field, the nature of side chains and hydrogen bonding. Quantitative analysis of amide III in the studied pH region, revealed that α-helix content decrease from aproximatively 38.4 % for healthy pregnant women to 27.3% for patients with PIH. The results are in agreement with the qualitative and quantitative analysis of amide I region. The changes in the secondary structure, espeacely α-helix content, of blood plasma observed by ATR-FTIR spectroscopy are in perfect correlation with the results obtained from the biochemical method of determination the damage on proteins due to oxidative stress. Previous studies have shown that reactive oxygen species produced in excess modify the structure of proteins, lipids and nucleic acids [12].

The changes in secondary structure of proteins resulted from the damage of proteins produced by excessive amount of reactive oxygen species. Because the changes in the secondary structure of blood plasma observed by ATR-FTIR spectroscopy are in perfect correlation with the serum carbonyl content of proteins in patients with preeclampsia, we can conclude that ATR-FTIR spectroscopy can be a consider as another method of detection the oxidative stress.

Conclusions

We may conclude that oxidative stress is one of the multiple dysfunctions that can be incriminated in the pathogenesis of preeclampsia because contributes to the accentuation of the imbalance of vasoconstrictor and vasodilatator factors. Moreover, the changes in serum carbonyl content of proteins, which are the products result from the reaction between reactive oxygen species and proteins in organism are perfectly correlated with the changes in the secondary structure of blood plasma proteins that is modified as well due to the oxidative stress. Therefore, we can affirm that ATR-FTIR spectroscopy can be a valuable method of detection the oxidative stress.

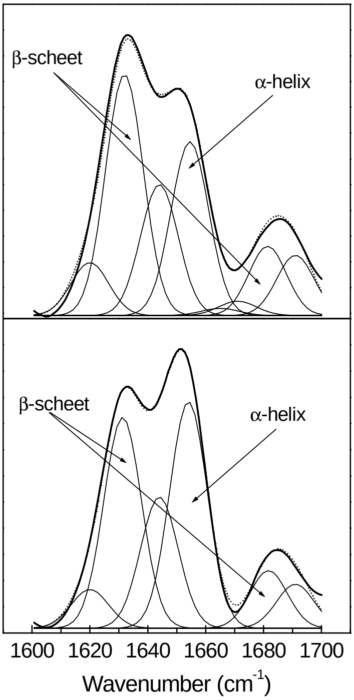

Fig. 4. Curve fitted inverted second derivative spectra amide I of lyophilized blood plasma for: patients with PIH (upper) and healthy pregnant women (lower)

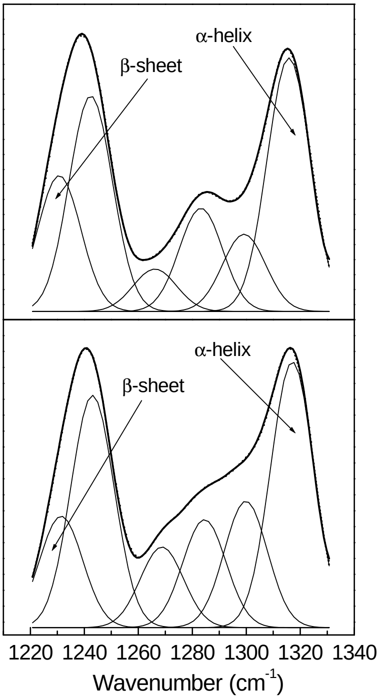

Fig. 5. Curve fitted inverted second derivative spectra amide III of lyophilized blood plasma for: patients with PIH (upper) and healthy pregnant women (lower)

REFERENCES

1. Danford's, *Obstetrics and gynecology*, Sixth edition, J. B. Lippincott Co., 1990, 1067-1121.
2. Dong, W.S. Caughey, *Methods Enzymol*. 232 (1994) 139–175.
3. H.H. Mantsch, D. Chapman, *Infrared Spectroscopy of Biomolecules*, Wiley-Liss, New York, 1996
4. Bandekar, J., *Biochim. Biophys. Acta* ,1120, 123-143 (1992)

5. Fu, F.-D., DeOliveira, D.B., Trumble, W.R., Sarkar, H.K. and Singh, B.R. *Appl. Spectr*. 48, 1432-1441 (1994)
6. Singh, B.R., Fuller, M.P., and Schiavo, G. , *Biophys. Chem*. 46, 155-166 (1990)
7. Singh, B.R., DeOliveira, D.B., Fu, F.-N., and Fuller, M.P. *Biomol. Spectr*. III, 47-55 (1993)
8. Reznick A.Z., Packer L., *Oxidative damage to proteins: method for carbonyl assay,* Methods enzymol, 1994, **233**: 357-363.
9. Amstrong D., *Free radical and antioxidant protocols*, Humana Press Inc., Totowa, New Jersey, 1998, 15-27.
10. Titheradge A. M., *Nitric oxide Protocols*, Humana Press Inc., Totowa, New Jersey, 1998, 83-155.
11. Huie R. E., Padmaja S., *The reaction of nitric oxide with superoxide*, Free Rad. Res. Commun., 1993, **18**: 195-199.
12. Beckman B.K., Ames N.B., *The free radical theory of aging matures*, Physiological Reviews, 1998, **2**: 547-581.
13. Dong, A., Prestrelski, S.J., Allison, S.D., Carpenter, J.F., *J. Pharm. Sci. 84*, 415-424, (1995)
14. Kendrick, B. S., Dong, A., Allison, S. D., Manning, M. C. & Carpenter, J. F. *J. Pharm. Sci.* 85, 155–158.20(1996)

STUDIA UNIVERSITATIS BABEŞ-BOLYAI, PHYSICA, L, 2, 2005

INFRARED ABSORPTION, RAMAN AND SERS INVESTIGATIONS OF 2, 1-BENZISOXAZOLE

M. BAIA[*] AND L. BAIA

ABSTRACT. Surface-enhanced Raman spectrum of 2, 1-benzisoxazole in activated silver colloid was recorded and compared with the normal Raman spectrum. The experimentally observed Raman bands together with their corresponding infrared bands were assigned based on the results of density functional theory (DFT) calculations. The significant changes evidenced between the SER and normal Raman spectra proved that this molecule is adsorbed on the colloidal silver particles through the lone pair electrons of the nitrogen atom. The orientation of the adsorbed species with respect to the metal surface was also predicted.

Keywords: Infrared and Raman spectroscopy, SERS, DFT calculations, 2, 1-benzisoxazole.

Introduction

Surface-enhanced Raman spectroscopy (SERS) has become during the past two decades a convenient technique for analyzing the adsorption of molecules on metallic surfaces [1]. It has been proven to be a very sensitive method able to detect molecules at trace concentration levels (ca 10^{-12} mol dm^{-3}) and to quench the fluorescence background by radiationless energy transfer to the metal surface from adsorbed species [1-3]. Recently semi-quantitative and quantitative analysis based on SERS has been described [4, 5], and therefore SERS has received considerable attention in the chemical, environmental and biomedical fields and also in the biology sciences.

The two main mechanisms proposed to account for the SERS effect are the electromagnetic enhancement [6] and the chemical or charge-transfer effect [7, 8]. In the former, the enhancement of the electromagnetic field near the metal surface is supposed to arise from plasmon resonances [6], while in the chemical mechanism the interaction between a specific group of the molecules and the metal atoms, which leads to a change in the molecular polarizability, is responsible for the appearance of SERS [7, 8].

2, 1-benzisoxazole (anthranil) and its derivatives are well known due to their extensive applications in pharmacology and analytical chemistry [9-13]. While the topical anthranil treatment was suggested for possible use in the bioassay of tumor promoters [9] and some 2, 1-benzisoxazole derivatives

---

[*] Corresponding author. E-mail address: monib@phys.ubbcluj.ro Physics Department, Babes-Bolyai University, M. Kogalniceanu 1, *400084 Cluj-Napoca, Romania*

shown cytotoxic and mutagenic activity [10], other anthranil derivatives proved to posses protective antiulcer effect and sedative activity [11, 12]. It was also shown [14] that 2, 1-benzisoxazole is the key intermediate in the decomposition process of nitroaromatic explosives.

For understanding the action of potential drugs, such as 2,1-benzisoxazole, it is essential to find out if the structure of the adsorbed species is similar to that of the free molecule. In these investigations [15] a silver surface serves as an artificial biologic interface.

In the present study, infrared absorption and Raman spectra of 2, 1-benzisoxazole have been recorded and assigned on the basis of the result of density functional theory calculations. Moreover, SERS has been applied to the 2, 1-benzisoxazole molecule in order to get insights about its adsorption behavior on the colloidal silver particles and to find out, from the enhancement of different Raman bands, the most probable orientation of the adsorbed species relative to the metal surface.

Experimental

2, 1-benzisoxazole of 99% purity was purchased from Lancaster and all other materials involved in substrate and solutions preparation were purchased from Aldrich as analytical pure reagents.

A stable sodium citrate silver colloid was prepared according to the standard procedure of Lee and Meisel [16] and employed as SERS substrate. The resultant colloid was yellowish gray with an absorption maximum at 412 nm. To 3 ml of silver colloid small amounts of 10^{-1} M ethanol solution of 2, 1-benzisoxazole was dropwise added using a micropipette. NaCl solution (10^{-2} M) was also added (10:1) for producing a stabilisation of the colloidal dispersion that yields to a considerable enhancement of the SER signal [17]. The final concentration of the sample in the colloidal suspension was of approximately $2.8 \bullet 10^{-4}$ M.

The FT-Raman spectrum of the sample was recorded using a Bruker IFS 120HR spectrometer with an integrated FRA 106 Raman module and a resolution of 2 cm^{-1}. Radiation of 1064 nm from a Nd-YAG laser was employed for excitation. A Ge detector, cooled with liquid nitrogen, was used. The infrared spectrum was recorded with a Bruker IFS 25 spectrometer and a resolution of 2 cm^{-1}. The SER spectrum of the sample on silver colloid, collected in the back-scattering geometry, was recorded on a Dilor Labram system equipped with an Olympus LMPlan Fl 50 microscope objective, an 1800 lines/mm grating and an external laser with an emission wavelength of 514 nm. In the recording of the SER spectrum a power of 100 mW on the sample has been employed. The focal length of the spectrometer is 300 mm and the slit used for all measurements was 50 µm. Thus, the spectral resolution was of about 2 cm^{-1}.

Theoretical calculations of the structure and vibrational wavenumbers of the investigated compound were performed using the Gaussian 98 program package [18]. Density functional theory (DFT) calculations were carried out with Becke's 1988 exchange functional [19] and the Perdew-Wang 91 gradient corrected correlation functional (BPW91) [20] and Becke's three-parameter hybrid method using the Lee-Yang-Parr correlation functional (B3LYP) [21]. The 6-31+G* Pople split-valence polarisation basis set was used in the geometry optimisation and normal modes calculations at all theoretical levels.

At the optimised structures of the examined species no imaginary frequency modes were obtained proving that a local minimum on the potential energy surface was found.

Results and discussion

The 2, 1-benzisoxazole molecule, which is the result of the junction of two planar cycles, a phenyl and an isoxazole ring, is planar and belongs to the C_s point group symmetry. The optimized geometry of this molecule with the labeling of the atoms is given in Fig. 1.

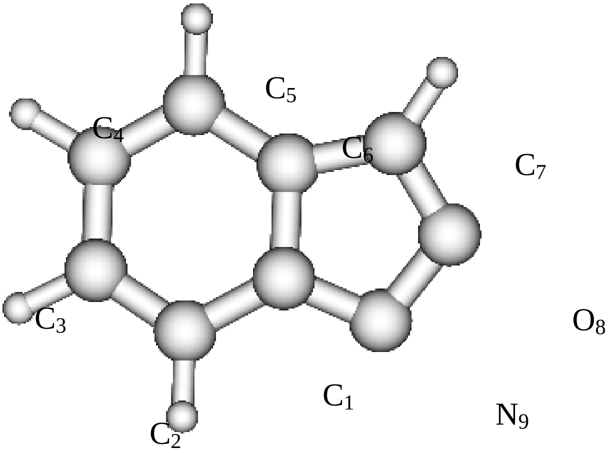

Fig. 1. Optimized geometry of the 2, 1-benzisoxazole molecule with the labeling of the atoms.

G. Mille and his coworkers [22] have already recorded and assigned the infrared and Raman spectra of the 2, 1-benzisoxazole molecule and compared them with those of the 1, 2-benzisoxazole compound. In the present study, a more detailed assignment of the vibrational modes of the title compound based on the results of DFT calculations is provided. The infrared absorption and Raman spectra of the 2, 1-benzisoxazole molecule in the spectral range between 450 and 3250 cm^{-1} are presented in Fig. 2 and the observed bands with their assignment performed with the help of the results of DFT calculations and of the already reported data [22] are summarized in Table 1.

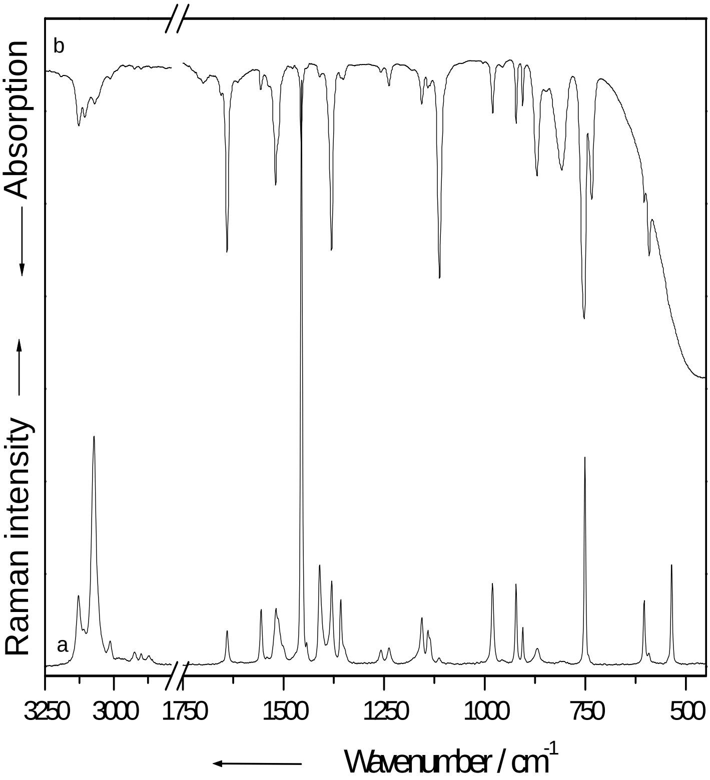

Fig. 2. FT-Raman (a) and infrared (b) spectra of the 2, 1-benzisoxazole molecule.

By comparing the calculated vibrational wavenumbers with the experimental results (see Table 1) one can observe that, similar to the results of previous studies [23, 24], the computed data using the B3LYP method are larger than those calculated with the BPW91 method. The disagreement between the theory and experiment could be a consequence of the anharmonicity and of the general tendency of the quantum chemical methods to overestimate the force constants at the exact equilibrium geometry [25]. One should also mention that the theoretical simulations were performed for the gas phase, while the experimental data were obtained for a liquid sample. However, as can be seen from Table 1 the predictions of the DFT methods for the vibrational frequencies are in consistently good agreement with the experimental values and allow the complete assignment of the vibrational modes.

Table 1.

Assignment of the theoretical wavenumbers values (cm^{-1}) to the experimental bands of the 2, 1-benzisoxazole molecule.

IR	Raman	Calc.[1]	Calc.[2]	Vibrational assignment
	214mw 264w	206 244	212 253	ring 1 + 2 out-of-plane def
	401mw	394	407	$\delta(N_9C_{1,2}) + \delta(C_{5,6,7})$
	435w	427	442	ring 1 out-of-plane def
	536m	529	544	$\delta(C_{1,2,3}) + \delta(C_{4,5,6})$
591ms	592sh	589	604	ring 2 out-of-plane def
604m	603m	596	613	$\delta(N_9C_{1,6}) + \delta(O_8C_{7,6})$
734m	741sh	751	763	$\omega(CH)$
752s	751ms	756	767	$\delta(C_{1,2,3}) + \delta(C_{4,5,6}) + \delta(C_7O_8N_9)$
809m	812vw	826	857	$\tau(CH)$ (ring 1)
868m	869mw	863	902	$\nu(N_9O_8)$
906m	905m	887	918	$\delta(C_{1,2,3}) + \delta(C_{3,4,5}) + \delta(C_{4,5,6})$
921m	922m	906	932	$\delta(C_7O_8N_9)$
956w	957vw	956	968	$\tau(C_7H)$
981m	980m	993	1008	ring 1 breathing
1113s	1114vw	1116	1155	$\tau(C_7H)$
1141m 1157m	1140m 1156m	1133 1157	1166 1190	$\delta(CH)$ (ring 1)
1238m	1237m	1234	1267	$\nu(C_{6,7}O_8)$
1258w	1258m	1249	1292	$\rho(CH)$ (ring 1)
1352m	1357m	1348	1390	$\rho(CH)$ (ring 1) + $\nu(C_1N_9)$
1381s	1380m	1365	1419	$\nu(C_1N_9) + \nu(C_{6,7})$
1410m	1409m	1398	1436	$\nu(C_{1,6}) + \nu(C_{3,4})$
1456m	1454vs	1465	1503	$\nu(C_{2,3}) + \nu(C_{4,5})$
1513sh 1520m	1513sh 1518m	1518	1563	$\nu_{sym}(C_{1,2,3})$
1555m	1555m	1555	1600	$\nu_{sym}(C_{4,5,6})$
1641s	1640m	1637	1689	$\nu_{as}(C_{1,2,3}) + \nu_{as}(C_{4,5,6}) + \nu_{as}(C_{5,6,7})$
3013m 3068m 3106m	3012m 3071s 3108sh	3123 3133 3147	3188 3198 3212	$\nu(CH)$ (ring 1)
3128m	3128m	3219	3285	$\nu(C_7H)$

Abbreviations: ring 1= phenyl ring, ring 2 = isoxazole ring, w = weak, m = medium, s = strong, sh = shoulder, ν = stretching, δ = bending, τ = twisting, ω = wagging, ρ = rocking, sym. = symmetric, as. = asymmetric. Calculated with: [1]BPW91/6-31+G*, [2]B3LYP/6-31+G*.

The SER spectrum of 2, 1-benzisoxazole is illustrated in Fig. 3 together with the normal Raman spectrum. Similar to the case of the adsorbed isoxazole molecules that exhibit Raman signals only in the presence of chloride anions [26], SERS enhancements were obtained only for 2, 1-benzisoxazole species adsorbed on activated silver colloids.

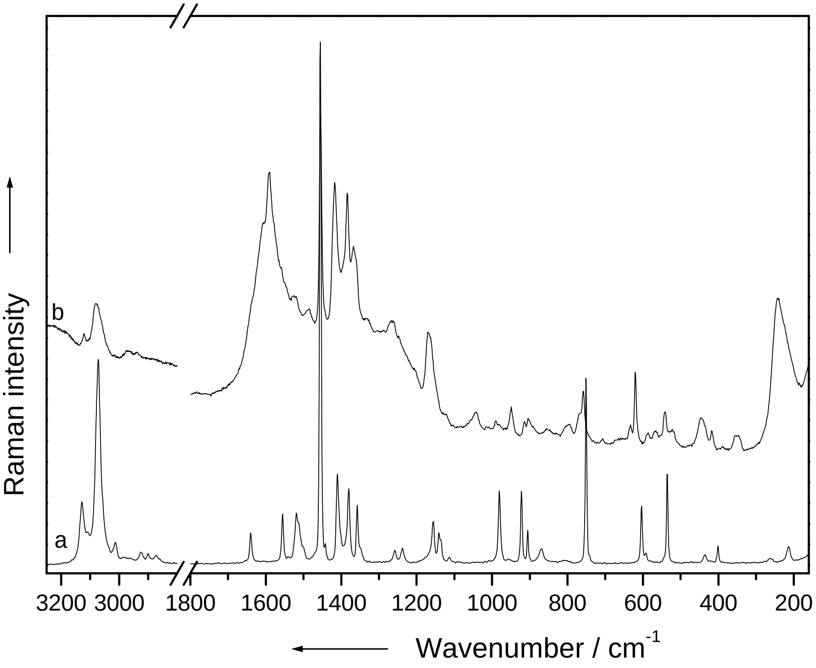

Fig. 3. FT-Raman (a) and SERS (b) spectra of the 2, 1-benzisoxazole molecule.

After a close analysis of the spectra (Fig. 3) and data summarized in Table 2 one can remark that the SERS bands are broader and their peak positions and relative intensities are changed relative to their corresponding Raman bands. These spectral features suggest the existence of a strong interaction between the anthranil molecules and the silver surface, unlike the isoxazole species that shown weak interactions with the metal surface not involving charge-transfer mechanism [26].

Table 2.
Assignment of the normal vibrational modes of the 2, 1-benzisoxazole molecule to the SERS bands.

Raman	SERS	Vibrational assignment
214mw	216sh	ring 1 + 2 out-of-plane def
264w	237s 270sh	ν(Ag-N) + ring 1 + 2 out-of-plane def
401mw	417m	$\delta(N_9C_{1, 2}) + \delta(C_{5, 6, 7})$
435w	446m	ring 1 out-of-plane def
536m	522m	$\delta(C_{1, 2, 3}) + \delta(C_{4, 5, 6})$
592sh	620m	ring 2 out-of-plane def
603m	632w	$\delta(N_9C_{1, 6}) + \delta(O_8C_{7, 6})$
741sh	758m	ω(CH)
751ms	768sh	$\delta(C_{1, 2, 3}) + \delta(C_{4, 5, 6}) + \delta(C_7O_8N_9)$
812vw	794mw	τ(CH) (ring 1)
869mw	856w	$\nu(N_9O_8)$
905m	904w	$\delta(C_{1, 2, 3}) + \delta(C_{3, 4, 5}) + \delta(C_{4, 5, 6})$
922m	913w	$\delta(C_7O_8N_9)$
957vw	949m	$\tau(C_7H)$
980m	990w	ring 1 breathing
1114vw	1120w	$\tau(C_7H)$
1140m 1156m	1162sh 1170m	δ(CH) (ring 1)
1237m	1244sh	$\nu(C_{6, 7}O_8)$
1258m	1265m	ρ(CH) (ring 1)
1348sh 1357m	1335m 1367ms	ρ(CH) (ring 1) + $\nu(C_1N_9)$
1380m	1384s	$\nu(C_1N_9) + \nu(C_{6, 7})$
1409m	1417s	$\nu(C_{1, 6}) + \nu(C_{3, 4})$
1454vs	1454vs	$\nu(C_{2, 3}) + \nu(C_{4, 5})$
1513sh 1518m	1518m 1524m	$\nu_{sym}(C_{1, 2, 3})$
1555m	1589s	$\nu_{sym}(C_{4, 5, 6})$
1640m	1640sh	$\nu_{as}(C_{1, 2, 3}) + \nu_{as}(C_{4, 5, 6}) + \nu_{as}(C_{5, 6, 7})$
3071s	3078ms	ν(CH) (ring 1)
3128m	3120w	$\nu(C_7H)$

Abbreviations: ring 1= phenyl ring, ring 2 = isoxazole ring, w = weak, m = medium, s = strong, sh = shoulder, ν = stretching, δ = bending, τ = twisting, ω = wagging, ρ = rocking, sym. = symmetric, as. = asymmetric.

By looking at the structure of the 2, 1-benzisoxazole species one supposes that it may bind to the silver surface either through the lone pair electrons of the nitrogen or oxygen atoms or through the π electrons system of the aromatic ring. For aromatic molecules it is known that [27] the bands due to ring vibrations are red shifted by more than 10 cm^{-1} and their bandwidths substantially increase, when the molecules adsorb on the metal surface via their π systems. Since our SERS spectrum exhibits shifts to higher wavenumbers in comparison to the normal Raman spectrum and the bandwidths were hardly affected by the adsorption, it is likely that the molecules are adsorbed on the colloidal silver particles through the nonbonding electrons of nitrogen and/or oxygen atoms.

The SER spectrum of 2, 1-benzisoxazole (Fig. 3) presents an intense band at 237 cm^{-1}, which is characteristic for the SER spectra of N-adsorbed species and is ascribed to the Ag-N stretching vibration [28]. The existence of this band can be regarded as an evidence of the anthranil species bonding to the silver surface through the lone pair electrons of the nitrogen atom, even if out-of-plane deformation vibrations of both benzene and isoxazole rings give rise to bands in approximately the same spectral region.

As one can see from Fig. 3 and Table 2 the experimental SERS bands at 417, 632 and 768 cm^{-1} attributed to the in-plane deformation vibration of both rings are shifted to higher wavenumbers up to 20 cm^{-1} relative to their corresponding Raman bands. The band at 990 cm^{-1} due to the breathing vibration of the benzene ring is also blue shifted in the SER spectrum by 10 cm^{-1}. From Fig. 3 and Table 2 one can also remark that most of the SERS bands present in the spectral range between 1400 and 1600 cm^{-1}, which are attributed to CC stretching vibrations, are blue shifted relative to their analogue Raman bands. The behavior of the SERS bands relative to their corresponding Raman bands further supports the assumption made above according to that the 2, 1-benzisoxazole molecules are adsorbed on the colloidal silver particles through the nonbonding electrons of the nitrogen atoms.

By following the enhancement of specific bands in the SER spectrum in agreement to the surface selection rules [29-31] the orientation of the adsorbed species relative to the metal surface can be determined. According to these rules the vibrational modes that involve a large change of the polarizability perpendicular to the metal surface are the most enhanced. By comparing the SER and Raman spectra of the 2, 1-benzisoxazole molecule one can see that the bands attributed to out-of-plane vibrations are mainly enhanced. Thus, the SERS bands at 446 and 620 cm^{-1} assigned to the out-of-plane deformation vibrations of the phenyl and isoxazole rings are enhanced in comparison with their corresponding Raman bands, while the bands given by the in-plane rings deformation vibrations present in the SER spectrum at 632 and 768 cm^{-1} are only weakly enhanced. The bands evidenced at 758, 794, 949 and 1120 cm^{-1} in the SER spectrum and assigned to the out-of-plane deformation vibrations of the CH groups of both rings (see Table 2) are also enhanced compared to their analogue Raman bands. However, in the high wavenumber region of the SER spectrum one can observe the enhancement of the bands at 3078 and 3120 cm^{-1}, which were clearly attributed to the CH stretching vibrations. Moreover, the band at 990 cm^{-1} assigned to the breathing vibration of the phenyl ring together with the bands due to the CC stretching vibrations of both rings situated in the spectral range between 1400 and 1600 cm^{-1} are also enhanced in the SERS spectrum. Having in view all these features of the SER spectrum we assume that the adsorbed 2, 1-benzisoxazole molecules adopt a tilted orientation relative to the silver surface.

Conclusion

The Raman and infrared spectra of the 2, 1-benzisoxazole molecule have been recorded and the assignment of the vibrational modes has been performed on the basis of the results of density functional theory calculations. The SER spectrum of the molecule in colloidal silver suspension has been also recorded and analyzed. By correlating the spectroscopic changes evidenced between the Raman and SER spectra it was concluded that the 2, 1-benzisoxazole molecules are adsorbed on the colloidal silver surface through the lone pair electrons of the nitrogen atoms. By following the enhancement of the SERS bands according to the surface selection rules a titled orientation of the adsorbed 2, 1-benzisoxazole species relative to the metal surface has been predicted.

Acknowledgment

The authors are thankful to Prof. J. Popp (University of Jena) for providing the samples and Prof. W. Kiefer (University of Wuerzburg) for providing access to experimental facilities and generous allotment of computing time.

REFERENCES

1. Chang, R. K.; Furtak, T. E. *Surface Enhanced Raman Scattering*; Plenum Press: New York, 1982.
2. Van Duyne, R. P. *Chemical and Biochemical Application of Lasers*; C. B. Moore, vol. 4, chap. 5, Academic Press: New York, 1978.
3. Campion, A.; Kambhanpati, P. *Chem. Soc. Rev*. **1998,** *27,* 241.
4. Jones, J. C.; McLaughlin, C.; Littlejohn, D.; Sadler, D. A.; Graham, D.; Smith, W. E. *Anal. Chem*. **1999,** *71,* 596.
5. Kneipp, K.; Kneipp, H.; Itzkan, I.; Dasari, R. R.; Feld, M. S. *Chem. Rev*. **1999,** *99(10),* 2957.
6. Moskovits, M. *Rev. Mod. Phys.* **1985,** *57*, 783.
7. Lombardi, J. R.; Birke, R. L.; Lu, T.; Xu, J. *J. Chem. Phys*. **1986,** *84,* 4174.
8. Creighton, J. A. *Surf. Sci*. **1983,** *124,* 208.

9. Armuth, V.; Berenblum, I. *Cancer Lett*. **1982,** *15(30)*, 343.
10. Sokovikov, Ya. V.; Sokovikova, I. N.; Kotov, A. D.; Orlov, V. Yu. *Toksikologicevskii Vestnik* **2002,** *2*, 29.
11. Manolov, P.; Todorov, S. *Eksp. Med. Morfol*. **1974,** *13(1),* 36.
12. Arya, V. P.; Shenoy, S. *J. Indian J. Chem.* **1976,** *14B(10),* 780.
13. Doppler, T.; Schmid, H.; Hansen, H. J. *Helvetica Chimica Acta* **1979,** *62*, 271.
14. He, Y. Z;. Cui, J. P.; Mallard, W. G.; Tsang, W. *J. Am. Chem. Soc.* **1988,** *110*, 3754.
15. Dryhurst, C. G. *Electrochemistry of Biological Molecules*; Academic Press: New York; 1977, p. 473.
16. Lee, P. C.; Meisel, D. *J. Phys. Chem*. **1982,** *86*, 3391.
17. Brandt, S. E.; Cotton, T. M. *Physical Methods of Chem. Series,* 2-nd ed., Wiley; 1993, Vol. IX B, p. 670.
18. Frisch, M. J.; Trucks, G. W.; Schlegel, H. B.; Scuseria, G. E.; Robb, M. A.; Cheeseman, J. R.; Zakrzewski, V. G.; Montgomery, J. A. Jr.; Stratmann, R. E.; Burant, J. C.; Dapprich, S.; Millam, J. M.; Daniels, A. D.; Kudin, K. N.; Strain, M. C.; Farkas, O.; Tomasi, J.; Barone, V.; Cossi, M.; Cammi, R.; Mennucci, B.; Pomelli, C.; Adamo, C.; Clifford, S.; Ochterski, J.; Petersson, G. A.; Ayala, P. Y.; Cui, Q.; Morokuma, K.; Malick, D. K.; Rabuck, A. D.; Raghavachari, K.; Foresman, J. B.; Ciolowski, J.; Ortiz, J. V.; Stefanov, B. B.; Liu, G.; Liashenko, A.; Piskorz, P.; Komaromi, I.; Gomperts, R.; Martin, R. L.; Fox, D. J.; Keith, T.; Al-Laham, M. A.; Peng, C. Y.; Nanayakkara, A.; Gonzales, C.; Challacombe, M.; Gill, P. M. W.; Johnson, B.; Chen, W.; Wong, M. W.; Andres, J. L.; Head-Gordon, M.; Repogle, E. S.; Pople, J. A. *Gaussian 98*, Revision A7, Gaussian Inc.: Pittsburgh, PA 1998.
19. Becke, A. D. *Phys. Rev.* **1988,** *A38,* 3098.
20. Perdew, J. P.; Wang, Y. *Phys. Rev.* **1992,** *B45*, 13244.
21. Becke, A. D. *J. Chem. Phys.* **1993,** *98*, 1372.
22. Mille, G.; Guiliano, M.; Angelelli, J. M.; Chouteau, J. *J. Raman Spectrosc*. **1980,** *9*, 339.
23. Scott, A. P.; Radom, L. *J. Phys. Chem.* **1996,** *100*, 16502.
24. Wong, M. W. *Chem. Phys. Lett.* **1996,** *256*, 391.
25. Rauhut, G.; Pulay, P. *J. Phys. Chem.* **1995**, *99,* 3093.
26. Muniz-Miranda, M. *Vib. Spectrosc.* **1999,** *19*, 227.
27. Gao, P.; Weaver, M. J. *J. Phys. Chem*. **1985,** *89,* 5040.
28. Chowdhury, J.; Ghosh, M.; Misra, T. N. *Spectrochim. Acta* **2000,** *A56,* 2107.
29. Hallmark, V. M.; Champion, A. *J. Chem. Phys.* **1986,** *84,* 2933.
30. Moskovits, M.; DiLella, D. P. *J. Chem. Phys.* **1980,** *73,* 6068.
31. Moskovits, M.; Suh, J. S. *J. Phys. Chem*. **1984,** *88,* 5526.

STUDIA UNIVERSITATIS BABEŞ-BOLYAI, PHYSICA, L, 2, 2005

THE MEASUREMENT OF THE METAL NANOPARTICLE SIZE

N. ALDEA[1], B. BARZ[1], P. MARGINEAN[1], T. D. SILIPAS[1], MIHAELA LAZAR[1], C. DUCU[2], XIE YANING[3], HU TIANDOU[3], LIU TAO[3], ZHONGHUA WU[3] AND FLORICA ALDEA[4]

ABSTRACT. A new theoretical analysis for determining the metal crystallite size and lattice strain from X-ray diffraction line profile broadening is presented. Emphasis is made on the rigorous analysis of the line profiles in terms of Fourier transform. Fermi generalized distribution function for single X-ray line profile approximation is used in order to determine the crystallite size and the lattice strain by the deconvolution technique. The microstructural parameters are obtained by using the Warren and Averbach theory and are included in the general form of the Fourier transform of the true sample. A comparison of microstructural models of the supported gold and nickel catalysts, determined by various analytical approximations, is presented.

KEYWORDS: Metal crystallite size, Microstrain, Deconvolution, Fourier transform technique, X-ray diffraction.

1. Introduction

X-ray diffraction line profile analysis is a versatile nondestructive method that can be used in obtaining nanostructural information (averaged over a moderately large volume about 1 mm^3) about supported metal catalysts used in oxidation, redaction, isotopic exchange and hydrogenation reactions. From the position and broadening of X-ray line profile (XRLP) are obtained the imperfect crystallite structure in terms of effective crystallite size and microstrain as lattice disorder. The purpose of this paper is to point out theoretical aspects of determining the metal nanoparticle size and the lattice distortion using various analytical approximations as well as a general formula based on Warren and Averbach theory. The results are exemplified by analyzing seven samples of supported gold and nickel catalysts: Au/SiO$_2$(1.2), Au/MTA, Au/SiO$_2$(1.1), Au/SiO$_2$IMP3, Au/Al$_2$O$_3$, Ni/SiO$_2$IMP2 and Ni/SiO$_2$MTB. The analytical models are implemented in our XRSIZE computer package program.

---

[1] National Institute of Research and Development for Isotopic and Molecular Technologies, R-400293 Cluj-Napoca, P.O. 5, Box 700, Romania
[2] University of Pitesti, Research Scienter for Advanced Materials, Romania
[3] Beijing Synchrotron RadiationFacilities of Beijing Electron Positron Collider National Laboratory, Beijing, People's Republic of China
[4] Agriculture Sciences and Veterinary Medicine University, Cluj-Napoca, Romania
*Corresponding author: naldea@s3.itim-cj.ro

2. Theoretical Background

X-ray diffraction pattern of a crystal can be described in terms of scattering intensity as function of scattering direction defined by the scattering angle 2θ, or by the scattering parameter $s=2\sin\theta/\lambda$, where λ is the wavelength of the incident radiation. Experimentally one can measure the integrated intensity profile function $h(2\theta)$ or $h(s)$ for the crystals. We shall discuss the X-ray diffraction for the mosaic structure model in which the atoms are arranged in blocks, each block itself being an ideal crystal, but with adjacent blocks not accurately fitted together. The experimental X-ray line profile (XRLP), h, represents the convolution of the true sample function f and the instrumental function g obtained from a well-annealed sample and it is described by the Fredholm integral equation of the first kind [1]

$$h(s)=\int g(s-s^*)f(s^*)\,ds^* \tag{1}$$

From mathematical point of view, the true sample function, $f(s)$, as a solution of eq. (1) can be obtained by three distinct methods: Fourier transform [2], regularization [3, 4] and the third order spline functions [5]. If one chooses the first one, the Fourier Transform of the true sample function will be

$$H(L)=G(L)F(L), \tag{2}$$

where $H(L)$ and $G(L)$ are Fourier transforms (FT) of the experimental XRLP and instrumental function, respectively. The variable L is the distance perpendicular to the (hkl) reflection planes. The crystallite size and lattice disorder can be analyzed as a set of the independent events of likelihood concept. The normalized $F(L)$ can be described as the product of two factors, $F^{(s)}(L)$ and $F^{(\varepsilon)}(L)$. The factor $F^{(s)}(L)$ describes the contribution of the crystallite size and the stacking fault probability while the factor $F^{(\varepsilon)}(L)$ gives information about the microstrain of the lattice. Based on Warren and Averbach theory [6], the general form of the Fourier transform of the true sample for cubic lattices is given by

$$F^{(s)}(L)=e^{-\frac{|L|}{D_{eff}(hkl)}}, \qquad F^{(\varepsilon)}(L)=e^{-\frac{2\pi^2\left\langle \varepsilon_L^2\right\rangle_{hkl} h_0^2L^2}{a^2}}, \tag{3}$$

where $D_{eff}(hkl)$ is the effective crystallite size, $<\varepsilon^2>_{hkl}$ is the microstrain of the lattice, $h_0^2=h^2+k^2+l^2$ and $C^2=2\pi^2h_0^2/a^2$. It is known that whenever two or more X-ray line profiles (XRLP) of the same (hkl) plane family are present the particle size and the lattice disorder effects can be separated. In this way Raitieri, Senin and Fagherazzi [7] investigated the global structure of Cu filings for (111) and (222) XRLP. X-ray line broadening investigations for supported metal catalysts have been done in order to find the average crystallite size from the integral breadth or the full width at half maximum (FWHM) of a diffraction profile. In the case of supported metal catalysts, it is impossible to obtain two orders of the same *(hkl)* profile due to the difficulty of performing satisfactory intensity measurements on the higher-order reflections. Consequently, it is not possible to apply the classical method of Warren [1]. Despite the numerous studies, the global microstructure parameters based on the single XRLP analysis are incompletely elaborated because many authors have used an approximate relations for the Fourier transform of the true sample. Some of them are presented in references [8-20]. The integral width $\delta^{[F]}$ of the Fourier transform for the true sample, present in equation (3) contains the crystallite size and the microstrain of the lattice, is given by the relation

$$\delta^{[F]}(\beta,\gamma)=\sqrt{\frac{\pi}{\beta}}\exp\left(\frac{\gamma^2}{4\beta}\right)\cdot\left[1-erf\left(\frac{\gamma\sqrt{\beta}}{2\beta}\right)\right], \tag{4}$$

where $\beta=\frac{2\pi^2\left\langle\varepsilon_L^2\right\rangle h_0^2}{a^2}$, $\gamma=\frac{L}{D_{eff}}$ and *erf* is the error function [21]. The general form of the true sample function *f(s)* is given by the inverse Fourier transform of *F(L)* [22],

$$f(s)=\int_{-\infty}^{\infty}e^{-\beta L^2-\gamma|L|}e^{2\pi isL}dL=$$

$$=\sqrt{\frac{\pi}{\beta}}\exp\left[\frac{\gamma^2-(2\pi s)^2}{4\beta}\right]\left\{\mathrm{Re}\left[erfc\left(\frac{\gamma-2\pi is}{2\sqrt{\beta}}\right)\right]\cos\frac{\pi\gamma s}{\beta}-\mathrm{Im}\left[erfc\left(\frac{\gamma+2\pi is}{2\sqrt{\beta}}\right)\right]\sin\frac{\pi\gamma s}{\beta}\right\}, \tag{5}$$

where $s=2\left(\frac{\sin\theta}{\lambda}-\frac{\sin\theta_0}{\lambda}\right)$ and *erfc* is the complementary error function [21,23]. The functions $F^{(s)}(L)$ and $F^{(\varepsilon)}(L)$ can be described as Fourier transforms of the following two distributions: Cauchy P_C, and Gaussian P_G

$$e^{-\frac{|L|}{D_{eff}}} = 2D_{eff}FT\left[\frac{\left(\frac{1}{D_{eff}}\right)^{2}}{\left(\frac{1}{D_{eff}}\right)^{2}+4\pi^{2}s*^{2}}\right]$$

and

$$e^{-\frac{2\pi^{2}\left\langle\varepsilon_{L}^{2}\right\rangle h_{0}^{2}\,L^{2}}{a^{2}}} = FT\left[\frac{a}{h_{0}}\sqrt{\frac{1}{2\pi\left\langle\varepsilon_{L}^{2}\right\rangle}} - e^{-\frac{a^{2}s*^{2}}{2\left\langle\varepsilon_{L}^{2}\right\rangle h_{0}^{2}}}\right] \tag{6}$$

The first distribution contains the crystallite size and the stacking fault probability while the second one contains the microstrain of the lattice. Based on Fourier transform proprieties, the true sample function can be described by an equivalent relation

$$f(s)=\int_{-\infty}^{\infty}P_{C}(s-s*)P_{G}(s)\,ds \tag{7}$$

In literature, relation (7), for explicit forms of P_C and P_G, is called Voigt distribution. Unfortunately, the integral from equation (7) can be performed only by numerical methods [24]. Because of this reason, many authors have considered that XRLP can be approximated by Voigt or pseudo Voigt (pV) distributions [25,26]. The integral widths δ_C, δ_G of P_C and P_G distributions, expressed in the reciprocal space units are given by the following relations

$$\delta_{C}=\frac{1}{2D_{eff}}, \qquad \delta_{G}^{2}=\frac{2\pi\left\langle\varepsilon_{hkl}^{2}\right\rangle h_{0}^{2}}{a^{2}} \tag{8}$$

In terms of P_C and P_G distributions, Fourier transform of the true sample, *F(L)*, is given by an equivalent relation

$$\mathrm{F(L)}=\mathrm{e}^{-2\,\delta_{C}\,|L|-\pi\,\delta_{G}^{2}\,L^{2}}, \tag{9}$$

and its integral width can be expressed by another equivalent relation,

$$\delta^{F}(\delta_C,\delta_G)=\frac{1}{\delta_G}\exp\left(\frac{\delta_C^2}{\pi\delta_G^2}\right)\left[1-\mathrm{erf}\left(\frac{\delta_C}{\sqrt{\pi}\delta_G}\right)\right]. \tag{10}$$

3. Results and discussion

The analytical models were applied on catalysts samples prepared by coprecipitation and impregnation. The following samples were investigated: Au/SiO_2(1.2), Au/MTA, Au/SiO_2(1.1), Au/SiO_2IMP3, Au/Al_2O_3**,** Ni/SiO_2IMP2, Ni/MTB. The standard samples were a well annealed gold foil and nickel black powder. The X-ray diffraction (XRD) measurements of supported metal catalysts were collected using a horizontal powder diffractometer in Brag-Brentano (BB) geometry on Dron 2 set up, having the Cu K_α radiation filtered. The wavelength of the incident ray for XRD experiments was 1.5406 Ǻ. A NaI (Ti) detector was used and the signals were amplified, fed to a single channel analyzer and read out by a computer. Practically speaking, it is not easy to obtain accurate values for the crystallite size and microstrain without extreme care in the experimental measurements and analysis of XRD data.

The XRLP Fourier analysis validity depends strongly on the magnitude and nature of the errors propagated in the data analysis. Three systematic errors have been discussed [23,27]: uncorrected constant background, truncation and the effect of sampling the observed profile at a finite number of points that appear in the discrete Fourier analysis. In order to minimize the propagation of these systematic errors a global approximation of the XRLP is adopted instead of the discrete Fourier analysis. Therefore, in this paper, the diffraction line broadenings for (111) (220) and (311) profiles was analytical calculated using the generalized Fermi function (GFF) [16-20, 23]. Based on the GFF approximation and the analytical deconvolution technique between experimental, instrumental XRLP and relation (3) the true sample functions have been obtained. By these techniques the curves of the experimental true sample functions and calculated ones exhibit good similarities. The main results regarding the investigated supported gold and nickel catalysts were obtained by data processing of the experimental XRLP using XRSIZE computer package program and are summarized in Table 1.

Table 1.

Structural parameters of supported gold and nickel catalysts

Sample no.	Sample	Line	D Scherrer [Å]	Polynomial approximation (L→0)		General relation		$\frac{(3)-(5)}{(5)}$ %	$\frac{(2)-(5)}{5}$ %
				D_{eff} [Å]	$<\varepsilon^2>$ x10^{-4}	D_{eff} [Å]	$<\varepsilon^2>$ x10^{-4}		
	0	1	2	3	4	5	6	7	8
1	Au/SiO_2(1.2)	(111)	355	285	0.08	218	0.07	30	62
2	Au/MTA	(111)	333	266	0.22	186	0.11	43	79
3	Au/SiO_2(1.1)	(111)	285	181	0.31	140	0.32	29	103
4	Au/SiO_2IMP3	(220)	129	63	0.33	61	0.31	3	111
5	Au/Al_2O_3	(311)	69	27	1.53	38	1.62	28	89
6	Ni/SiO_2IMP2	(111)	55	21	1.98	32	1.8	34	71
7	Ni/MTB	(111)	219	118	0.42	104	0.42	13	110

The second column indicates the crystallite size of investigated samples calculated by classical Scherrer formula.

The third up to the sixth columns contain the average crystallite size and microstrain of the lattice determined by polynomial approximations and general relation. There are large differences between global structural parameters corresponding to each computation technique.

The nanostructural parameters determined by polynomial approximations are very sensitive to the interval limits chosen for the fitting technique. The literature does not indicate a reliable prescription for choosing them. This situation is caused by the fact that the *F(L)* function is approximated only by a polynomial portion. The global structure parameters can be analyzed by the absolute value of the relative variation (AVRV) of the crystallite size given by the general form of the true sample function. By analyzing the AVRV values from column 7 corresponding for each sample we have obtained the following relation:

AVRV(4) < AVRV(7) < AVRV(5) < AVRV(3) < AVRV(1) < AVRV(6) < AVRV(2),

while the AVRV values from column 8 give the following succession:

AVRV(1) < AVRV(6) < AVRV(2) < AVRV(5) < AVRV(3) < AVRV(7) < AVRV(4)

From the first succession we can consider that, for small crystallite, the polynomial approximations and the general relation exhibit good similarities. The similarities around L → 0 are due to the close values given by the polynomial approximation and the general relation while for large value of L this approach disappears.

The second succession shows a worse correlation for the values in the columns three and five, due to the Scherrer formula that does not take into consideration the microstrain of lattice. It can be used only for large values of the crystallite size.

The most valuable formula for global microstructural information obtainable from XRLP analysis is the general relation (5). This relation is valid for any value of *L* and is not sensitive for the interval chosen because the Fourier Transform of the true sample is defined on the whole real axis. Our results, determined by polynomial distributions are based on approximations when $L \to 0$ from relation (9). The definition interval is changed until the obtained results are similar to the ones obtained with the general formula.

In many cases, in literature, are reported results obtained only with the Scherrer relation for quite large values of the integral width, without taking into account the contribution of the disorder parameter to the line shape. This can be reflected in ambiguous results.

The microstrains of the lattice can also be correlated with the effective crystallite size in the following ways: the value of the effective crystallite size increases when the microstrain value decreases, and vice versa.

5. Conclusions

In the present paper it is presented a theoretical analysis of the X-ray line profile applied to the global structure determination of the supported nickel catalysts used in reactions as: reduction, oxidation, hydrogenation and isotopic exchange between hydrogen and deuterium. Their global structures can be correlated with the intrinsic catalytic activity.

The conclusions that can be draw from this study are:

- For XRLP analysis, a global approximation by GFF distribution is applied rather than a numerical Fourier analysis. This can minimize the systematic errors that appear in the traditional Fourier analysis;

- The approximate forms of the Fourier transform are valid only for small crystallite size, less than 100 Å, and its general form can also be used use for any value of the variable *L*;
- The new analytical true sample function and its approximation is one of the most general formula that contains the Cauchy and Gaussian contributions;
- XRSIZE package program contains all the methods described in the second section and it has a user's friendly interface.

REFERENCES

1. B. E. Warren, X-Ray Diffraction, Addison-Wesley Publishing Company, 1969.
2. E. O. Brigham, The Fast Fourier Transform, Pretice-Hall Inc., Englewood Clifs, New Jersy, 1974.
3. Tihonov and V.Arsenine, Méthodes de Résolution de Problèmes Mal Posés, Ed. Mir, Moscou, 1974.
4. H.J. J. Te Riele, A program for solving first Fredholm integral equations by means of regularization, Report NM-R8416 of Center for Mathematics and Computer Sciences, 1984.
5. Beniaminy, M. Deutsch, Comput. Physics Common. **21**, 1980, 271. H. P. Klug, L. E. Alexander, X-Ray Diffraction Procedures for Polycrystalline and Amorphous Materials, 2nd ed. John Wiley and Sons, New York, 1974.
6. F. Raiteri, A. Senin, G. Fagherazzi, J. Mater. Science **13**, 1978, 1717.R. 7. S. Smith, IBM J. Res. Develop. **4**, 1960, 205.
8. G. B. Mitra, N. K. Misra, Acta Cryst. **22**, 1967, 454.
9. J. Mignot, D. Rondot, Acta Met. **23**, 1975, 1321.
10. J. Mignot, D. Rondot,, Acta Cryst. **33**, 1977, 327.
11. E. J. Charlson, D. H. Hu, M. R. Farukhi, Adv. X-Ray Anal. **14**, 1971, 441.
12. P. Ganesen H. K Kuo, A. Saavedra, J. Catal. **52**, 1978, 310.
13. N. Aldea, E. Indrea , Comput. Phys. Commun **60**, 1990, 155.
14. N. Aldea, R. Zapotinschi, C. Cosma, Fresenius J. Anal. Chem. **355**, 1995, 367.

15. N. Aldea, A. Gluhoi, P. Marginean, C. Cosma, X. Yaning, Spectrochim. Acta Part B **55**, 2000, 997.

16. N. Aldea, A. Gluhoi, P. Marginean, C. Cosma, Xie Yaning,, H. Tiandou, W. Wu, B. Dong, Spectrochim. Acta Part B **57**, 2002, 1453.

17. N. Aldea, C. V. Tiusan, B. Barz, J. Optoelectron. Adv. Mater. **6**(1), 2004, 225.

18. N. Aldea, C. Tiusan, R. Zapotinschi , Proceedings of the 8th Joint EPS-APS International Conference on Physics Computing, Published by Academic Computer CYFRONET-Krakow, 1996, p. 391.

19. N. Aldea, B. Barz, A. C. Gluhoi, P. Marginean X. Yaning H. Tiandou L. Tao, Z. Wu, Z. Wu, J. Optoelectron. Adv. Mater**. 6**(4), 2004, 1287.

20. P. Abramovich and I. A. Stegun, Handbook of Mathematical Function, Dower, New York 1965.

21. N. Aldea, B. Barz, T. D. Silipas, Florica Aldea and Zhonghua Wu, sent for publishing, J. Optoelectron. Adv. Mater, sept. 2005.

22. N. Aldea and F. Aldea, Analysis Techniques of Physical-Chemical Signals, Ed. Risoprint, Cluj-Napoca, 2001 (in Romanian language).

23. J. F. Kielkopf, J. Opt. Soc. Am. **63**(8), 1973, 987.

24. Balzar , H. Ledbetter J. App. Cryst. **26**, 1993, 97.

25. J. Mittemeijer and P. Scardi, Diffraction Analysis of the Microstructure of Materials, Springer Verlag, Berlin, Heidelberg, 2004.

26. R. A. Young, R. J. Gerdes, A. J. C. Wilson, Acta Cryst. **22,** 1967, 155.